BODIPY dyes for application in the photo-oxidation of pollutants, photodynamic antimicrobial chemotherapy, and nonlinear optics

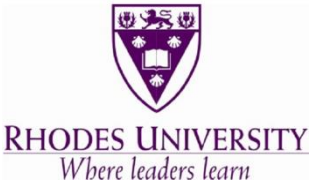

A thesis submitted in fulfillment of the

requirements for the degree of

MASTER OF SCIENCE

of

RHODES UNIVERSITY

by

Lebechi Augustus Kelechi

February 2019

Acknowledgements

I would like to first thank my supervisor, Dr J. Mack for the opportunity and privilege to work with him and for making this project a reality. I would also like to thank Prof. T. Nyokong, my co-supervisor, for all her support and encouragement. It would have been impossible to have any of this without the two of you; words cannot express my gratitude. In this regard, special thanks also go to Ms Gail Cobus for all the work she does that make the period of my studies seamless and free of administrative litter. I want to also thank Dr Britton for all the technical work and other things you do to keep our laboratory running smoothly. To everyone in laboratory S22: Thank you for the support, and for making the laboratory a conducive environment for flourishing research. Above all, I would like to thank God almighty for everything, my family for every support and encouragement, my friends and acquaintances, thank you all for being there for me even during the most challenging moments of my studies. Financial support from the DST MINTEK Nanotechnology Innovation Centre is acknowledged with a grateful heart.

Abstract

The synthesis and structural characterization of a series of BODIPY dyes to analyze both the effects of halogenations at the 2,6-positions and the introduction of styryl groups at the 3,5-positions. The photophysical properties of these dyes were investigated to determine their suitability as singlet oxygen-generating photosensitiser dyes for application in photocatalytic degradation of azo dyes and in photodynamic antimicrobial chemotherapy (PACT). Upon halogenation, the dyes showed high to moderate singlet oxygen quantum yields. The potential utility of electrospun polystyrene (PS) nanofibres embedded with halogenated BODIPY dyes for the photocatalytic degradation of Orange G and Methyl Orange from textile industry effluents were investigated. A comparison of the singlet oxygen quantum yield of the BODIPY dyes in solution and when embedded in the PS nanofibres support demonstrates that its photosensitiser properties are maintained in the nanofibre mats. The photocatalytic degradation properties of the PS nanofibres for Orange G and Methyl Orange were determined by using a 530 nm and 660 nm light-emitting diodes. The rate of photodegradation increases with both the Orange G and Methyl Orange concentrations and follows pseudo-first-order kinetics. The PACT activities of brominated BODIPYs on *Escherichia coli* and *Staphylococcus aureus* were investigated. Log reduction values of over 9 were obtained during the photoinactivation of *Staphylococcus aureus*. To be able to red-shift the main spectral band of the BODIPY dyes into the therapeutic window, styryl groups were introduced at the 3,5-positions through a modified Knoevenagel condensation reaction. Because the red-shifted spectral band lies above 532 nm, the second harmonic of the Nd:YAG laser, there is very minute absorption at this wavelength. One of the novel brominated BODIPY dyes was investigated for its potential utility as optical limiting materials in nonlinear optics (NLO), and the dyes demonstrated typical nonlinear absorption behaviour characterised by reverse saturable absorption (RSA) in

Z-scan measurements. Excellent optical limiting parameters were obtained for third-order susceptibility and hyperpolarisability.

Table of Contents

List of Schemes

List of Figures

List of Tables

List of Symbols

A	Absorbance
Å	Angstrom
α	Linear absorption coefficient
β	Nonlinear absorption coefficient
ε	Molar extinction coefficient
γ	Second-order hyperpolarisability
I_{lim}	Optical limiting threshold
Im[$\chi^{(3)}$]	Third-order nonlinear susceptibility
λ	Wavelength
η	Refractive index
Φ_{Δ}	Singlet oxygen quantum yield
Φ_{F}	Fluorescence quantum yield
S_n	n^{th} electronic excited state
S_0	Singlet ground state
S_1	First singlet excited state
S_2	Second excited state
T_1	First triplet excited state
τ_F	Fluorescence lifetime
t	Time

List of Abbreviations

Abs	Absorption
ADMA	Anthracene-9,10-bis-methylmalonate
APTES	3-aminopropyl triethoxysilane
BODIPY	4,4′-difluoro-4-bora-3a,4a-diaza-*s*-indacene
B3LYP	Becke 3-Parameter, Lee, Yang and Parr
CAM-B3LYP	Coulomb-attenuating method - Becke 3-Parameter, Lee, Yang and Parr
CFU	Colony forming unit
DCM	Dichloromethane
DFT	Density functional theory
DMSO	Dimethyl sulfoxide
DPBF	1,3-Diphenylisobenzofuran
E. coli	*Escherichia coli*
Em	Emission
ESA	Excited state absorption
Exc	Excitation
FT-IR	Fourier-transform infrared spectroscopy
HOMO	Highest occupied molecular orbital
ISC	Intersystem-crossing
LUMO	Lowest unoccupied molecular orbital
MALDI-TOF	Matrix-assisted laser desorption/ionisation-time of flight
MNPs	Magnetic nanoparticles
MRSA	Methicilin-resistant *Staphylococcus aureus*
MS	Mass spectrometry
NBS	*N*-bromosuccinimide

Nd:YAG	Neodymium-doped yttrium aluminium garnet
NLA	Nonlinear absorption
NLO	Nonlinear optics
NLS	Nonlinear light scattering
NMR	Nuclear magnetic resonance spectroscopy
NPs	Nanoparticles
NLR	Nonlinear refraction
OL	Optical limiting
PACT	Photodynamic antimicrobial chemotherapy
PBS	Phosphate-buffer saline
PS	Polystyrene
PDT	Photodynamic therapy
ROS	Reactive oxygen species
RSA	Reverse saturable absorption
RT	Room temperature
SEM	Scanning electron microscopy
S. aureus	*Staphylococcus aureus*
TCSPC	Time-correlated single photon counting
TEA	Triethylamine
TEOS	Tetraethyl orthosilicate
TFA	Trifluoroacetic acid
THF	Tetrahydrofuran
TLC	Thin layer chromatography
2PA	Two-photon absorption
XRD	X-ray powder diffraction

ZnPc	Zinc phthalocyanine

Chapter 1

1. INTRODUCTION

Fluorophores are functional organic molecules [1]. Due to their photophysical properties, they have found applications in many areas of science especially in chemistry, materials, and biology where they are employed as active media for tunable lasers, in the development of photoelectronic devices, and as fluorescence and chemical probes [2]. Notwithstanding, the favourable photophysical properties of fluorescent organic dyes, properties such as their high fluorescence quantum yields and strong absorption in the visible region can limit their application in other areas such as their use as photosensitiser dyes in photocatalysis [2,3], and in photodynamic antimicrobial chemotherapy (PACT) [4] in the absence of further structural modifications being made. In this study, the boron dipyrromethene (BODIPY) fluorophore is structurally modified to become suitable for use in in the photooxidation of pollutants, PACT, and in nonlinear optics.

The principles of photocatalytic degradation involve using cytotoxic singlet oxygen photogenerated upon illuminating a photosensitiser dye with light of appropriate wavelength to photodegrade/phototransform organic pollutants [3]. These photogenerated reactive oxygen species (ROS) such as $^1O_2$ ($^1\Delta_g$) are utilised in mineralising organic pollutants such as azo dyes and xanthenes dyes to less hazardous elements [4]. Advanced oxidation mechanisms have proven their efficacy in degrading recalcitrant organic dye pollutants in wastewater [5]. The photocatalytic oxidation of pollutants has significant advantages over other approaches since it generally does not lead to the release of harmful by-products. Studies have found that the photosensitisers developed for photocatalytic oxidation have also become useful in PACT, an alternative antimicrobial treatment methodology for microbes that have developed resistance to conventional treatment methodology [6]. PACT involves microbial inactivation by singlet

oxygen and other reactive oxygen species, in this regard, militating against the issue of microbial resistance to traditional methods of treatment.

The study of NLO deals with the study of interactions of electromagnetic fields in various media producing new fields that are altered in phase, frequency, amplitude, or other propagation characteristics from the incident field [7]. In essence, NLO materials can be used to manipulate optical signals in telecommunication systems, and other optical signal processing applications [8]. In the context of this study, optical limiting materials limit the output of the emerging beam when exposed to very intense light such as that from high-intensity lasers [7, 8]. There is an urgent need for alternative antimicrobial treatment through PACT, wastewater remediation through photocatalytic degradation, coupled to the protection of sensitive optics from high-intensity lights that could be harmful; therefore, the design of novel photosensitiser dyes for use in these applications is an important research goal. An in-depth understanding of the photophysical properties of these dyes is required along with novel synthetic strategies that provide easy modifications of the molecular structure of the chromophore by adding appropriate functionalities according to the desired need.

1.1. BODIPY Dyes

1.1.1. History and Structure

Functional molecules, such as light-emitting dyes (fluorophores) have wide-ranging applications in diverse fields [9]. Their favourable photophysical properties notwithstanding, unfavourable properties such as high fluorescence quantum yields, structural instability, the limited usable range of solvents and strong absorption in the visible region limits the utility of many fluorophores for use in other applications such as photosensitisers in photocatalytic degradation and PACT. Although a wide range of fluorophores exist, the reactivity of organic molecules when subjected to sustained intense incident light especially in the presence of

molecular oxygen has necessitated the search for more photostable dye molecules [10]. In some contexts low triplet yielding molecules can be used since the pathway of decomposition via singlet oxygen is, at least partially curtailed [10], but in this study heavy atoms are incorporated to enhance the formation of the triplet state and the generation of singlet oxygen.

BODIPY dyes (4,4′-difluoro-4-bora-3a,4a-diaza-*s*-indacenes) as structural analogues of porphyrins have been the focus of considerable research over the last three decades [11]. The synthetic methodology of BODIPY dyes was first described by Treibs and Kreuzer in the 1960s, but the dyes did not garner much attention prior to their application as solid state concentrators in the 1980s [12]. Subsequently, their utility as laser dyes, fluorescent stains, and labels in fluorescent imaging and as indicator dyes in sensor applications has been reported [13]. There has been a vast increase in explorative research based on BODIPY fluorophores in recent years due to their favourable properties compared to fluoresceins and rhodamines (**Figure 1.1**), such as (i) their facile synthesis and ease of structural modifications, (ii) their excellent photophysical properties which includes: narrow Gaussian-shaped absorption and emission bands, high molar extinction coefficients (usually $\varepsilon > 80\ 000\ M^{-1}\ cm^{-1}$) and fluorescence quantum yield values (commonly $\Phi > 0.5$), moderate redox potentials, negligible triplet-state formation in the absence of heavy atoms, negligible sensitivity to solvent polarity, excellent photostability and high solubility in common used organic solvents of varying polarities [11,13,14].

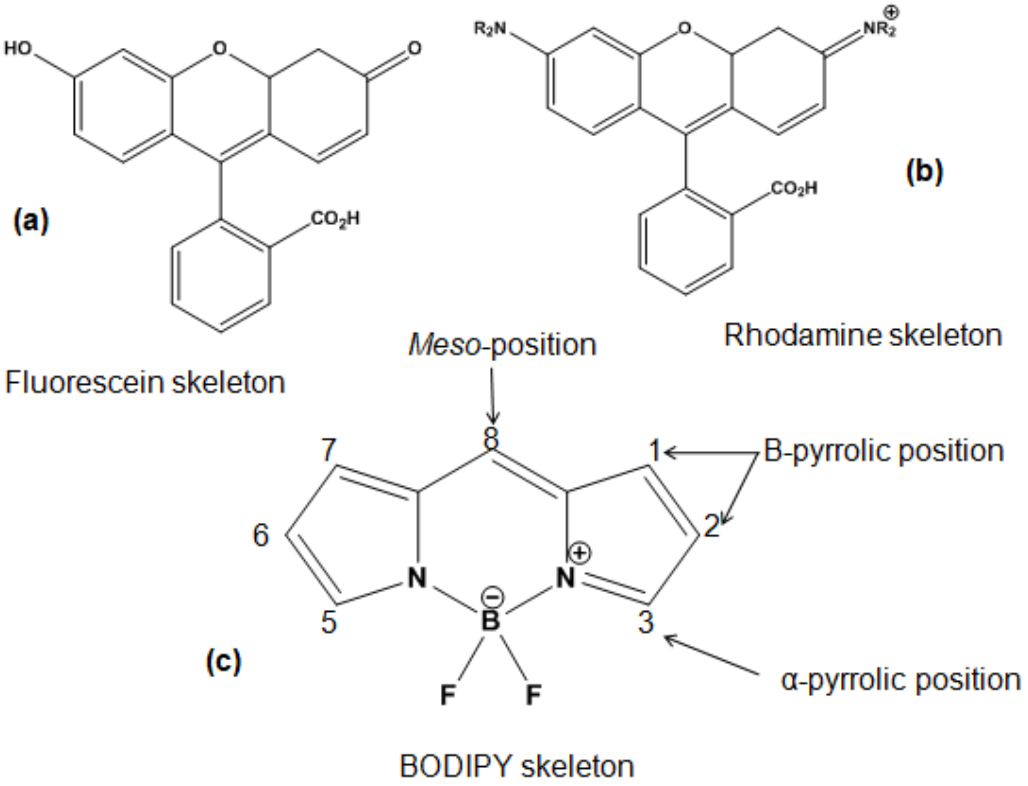

Figure 1.1. Generic structures of (a) fluorescein and (b) rhodamines; and (c) the BODIPY core and its IUPAC numbering system.

BODIPY core dyes are heterocyclic molecules consisting of two pyrrole units connected by a methene bridge at the 2-position and complexed by BF_2 [13]. The two pyrrole rings are bridged at the *meso*-position to form the intermediate dipyrromethene [15]. The BODIPY molecule is planar, and because of the heteroatoms is slightly polarised, providing scope for electrophilic and nucleophilic reactions at different sites on the core [16]. BODIPY dyes can be likened to "constrained" cross-conjugated cyanine type dyes due to the BF_2 complexation, which prevents the *cis-trans* isomerisation and interpyrrolic chain twisting that is commonly associated with other cyanine type dyes [17]. During synthesis, the complexation of dipyrromethene with boron trifluoride leads to the formation of a dipyrromethene boron difluoride structure which can be considered an example of a rigidified monomethine cyanine dye (**Figure 1.2**) [15-17]. The high

fluorescence quantum yields of BODIPY dyes compared to cyanine dyes is associated with this restricted flexibility [17].

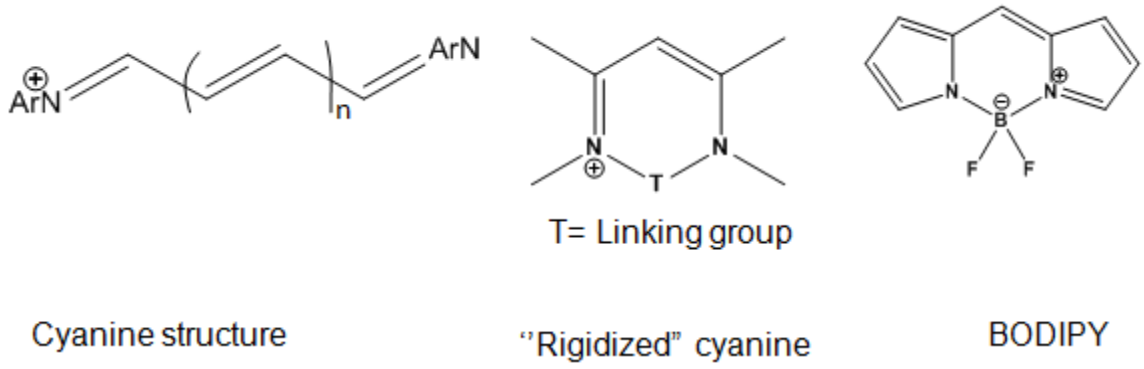

Figure 1.2. A comparison of cyanine structures.

BODIPY dyes have been used as a more photostable replacement for fluoresceins in biological imaging and as tunable laser dyes [18,19]. BODIPY dyes despite displaying properties typical of an aromatic compound are only quasi-aromatic, since they do not obey Huckel's 4N+2 rule for aromaticity [18,19].

1.1.2. The synthetic methodology of BODIPY core dyes

BODIPY dye synthesis is often based on the acid-catalysed condensation of pyrroles to yield the intermediate dipyrromethene, a procedure previously developed for porphyrins and other macrocyclic compounds [2]. Formation of a wide variety of dipyrromethene ligands is easily achieved by using pyrroles and highly electrophilic carbonyl compounds (for example, acid chlorides, acid anhydrides or aldehydes) to form the methene bridge between two pyrrole units [20]. Subsequently, BF_2 complexation in the presence of a base such as tertiary amine affords BODIPY core in high reproducible yields (**Scheme 1**) [2]. Using this approach, many symmetric BODIPY dyes have been prepared from readily available pyrrole units with much of the synthetic effort focused on varying the substituents at the *meso*-position [20]. When 2,4-dimethylpyrrole is used as the precursor as is the case in this study, the incorporation of

different functional groups onto the BODIPY core usually results in only minor changes to the photophysicochemical properties [21], since the geometry of the chromophore and the electron density on the BODIPY core is not perturbed [20, 21]. Several pathways are available for the synthesis of the parent BODIPY core as well as the symmetrical and asymmetrical BODIPY dyes as shown in **Figure 1.3.**

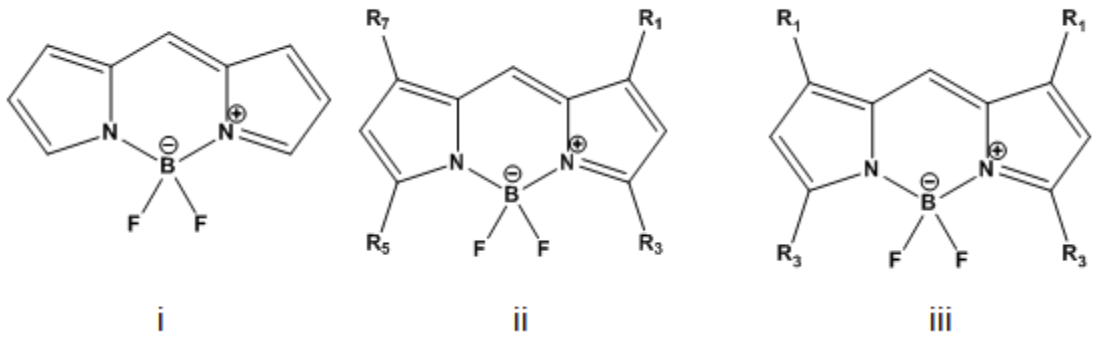

Figure 1.3. Molecular structures of (i) *meso*-unsubstituted BODIPY core, (ii) asymmetrical and (iii) symmetrical BODIPY dyes.

1.1.2.1. Synthesis of the unsubstituted BODIPY core

Studies have shown that unsubstituted dipyrromethene is unstable in solution at temperatures above −40°C due to their susceptibility to nucleophilic attack, so the synthesis of unsubstituted parent BODIPY core becomes very challenging [18]. To overcome this challenge, stabilisation of the dipyrromethene upon oxidation from dipyrromethane is of paramount importance. Bruce and co-workers thus carried out the oxidation reaction of dipyrromethane at −70°C and upon completion; dipyrromethene was allowed to react with boron trifluoride diethyl etherate at the same temperature for an hour prior to heating the reaction under reflux in dichloromethane (Route 1, **Scheme 1**) [18]. Finally, the fully unsubstituted parent BODIPY core was isolated as a stable bright red solid in 5−10% yield. Wild and co-workers (Route 2) utilised the one-pot synthetic pathway which involves the trifluoroacetic acid-catalysed direct condensation of 2-

formylpyrrole and 1H-pyrrole, followed by deprotonation with diethyldiisopropylamine and subsequent complexation of the dipyrromethene intermediate with boron trifluoroetherate [16]. Subsequent purifications steps through fast filtration and column chromatography gave the compound at a low yield (< 10%). Peňa-Cabrera et al. (route 3) reacted 8-thiomethylBODIPY with triethylsilane by using Pd as a catalyst and a stoichiometric amount of copper(1)thienyl-2-carboxylate (CuTC) in THF at 55°C and formed an unsubstituted BODIPY in quantitative yield [19].

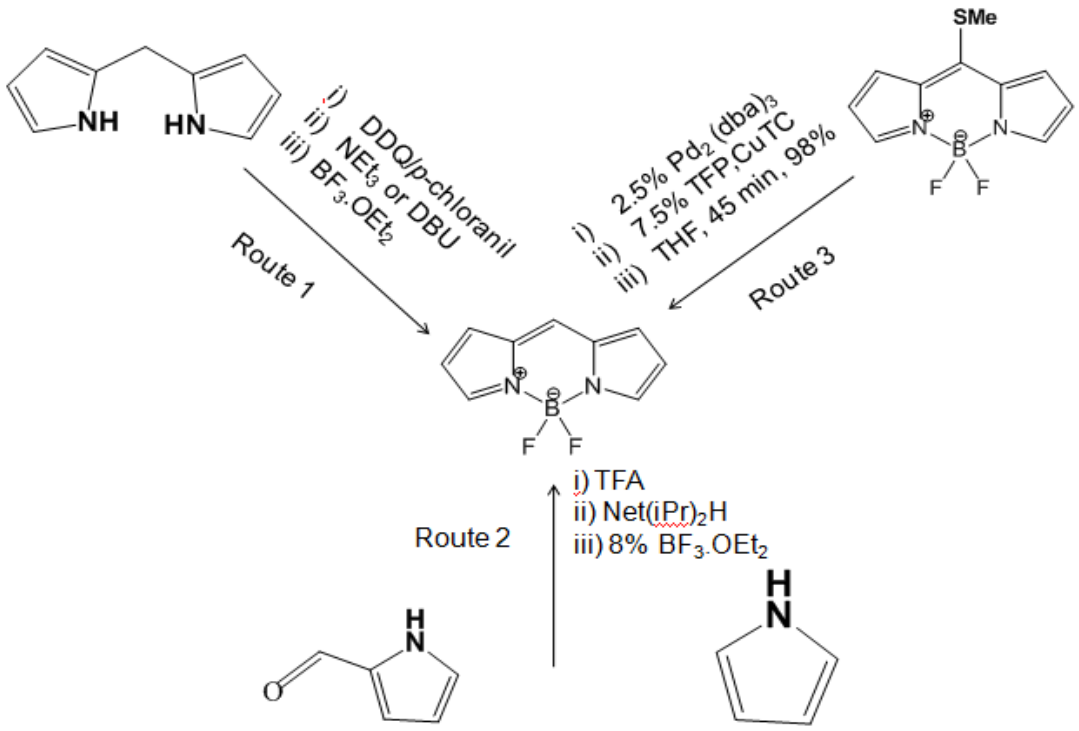

Scheme 1. Different pathways for the synthesis of an unsubstituted BODIPY core.

1.1.2.2. Synthesis of substituted BODIPY core dyes

One of the main synthetic routes for BODIPY core dyes follows the route shown in **Scheme 2**. A McDonald's coupling condensation reaction is used [22]. This involves an acid-catalysed condensation of 2-formyl pyrrole with a pyrrole that has no substituent at the α-position. Generally, high product yields are observed through this synthetic route, sometimes with limitations during product purification from the reaction mixture. Self-condensation of 5-

formyl pyrrole can become competitive resulting in undesirable symmetric dipyrrin salt when pyrroles that lack substituents at the α-position with electron-withdrawing groups are used [22]

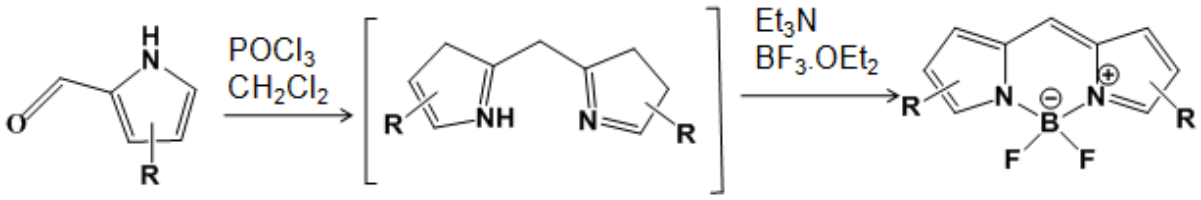

Scheme 2. A generalised synthetic route for BODIPYs.

Symmetric BODIPY dyes with substituents at the *meso*-position are synthesised mainly via a one-pot synthetic method shown in **Scheme 3**. This was the approach followed in this study. A Lewis acid (typically trifluoroacetic acid) catalyses the condensation of pyrroles with aldehydes, acid chlorides or anhydrides, yielding dipyrromethanes which subsequently are oxidised to dipyrromethenes. Further complexation of dipyrromethenes with $BF_3 \cdot OEt_2$ in the presence of a base usually a tertiary amine (triethylamine) gives BODIPY dyes in yields greater than 50%. Pyrroles substituted at the 2, 4-positions are generally used in this reaction to avoid polymerisation. Another advantage is that BODIPY dyes with substituents at the *meso*-position often display enhanced stability in comparison to their *meso*-unsubstituted counterparts [23]. Synthesis of *meso*-unsubstituted asymmetric BODIPY dyes can be achieved by the self-condensation process involving an appropriate pyrrole carbonyl cation precursor under acidic conditions (usually *p*-toluenesulfonic acid, *p*-TSA or Montmorrilonite clay), subsequent $BF_3 \cdot OEt_2$ complexation gives the product [23].

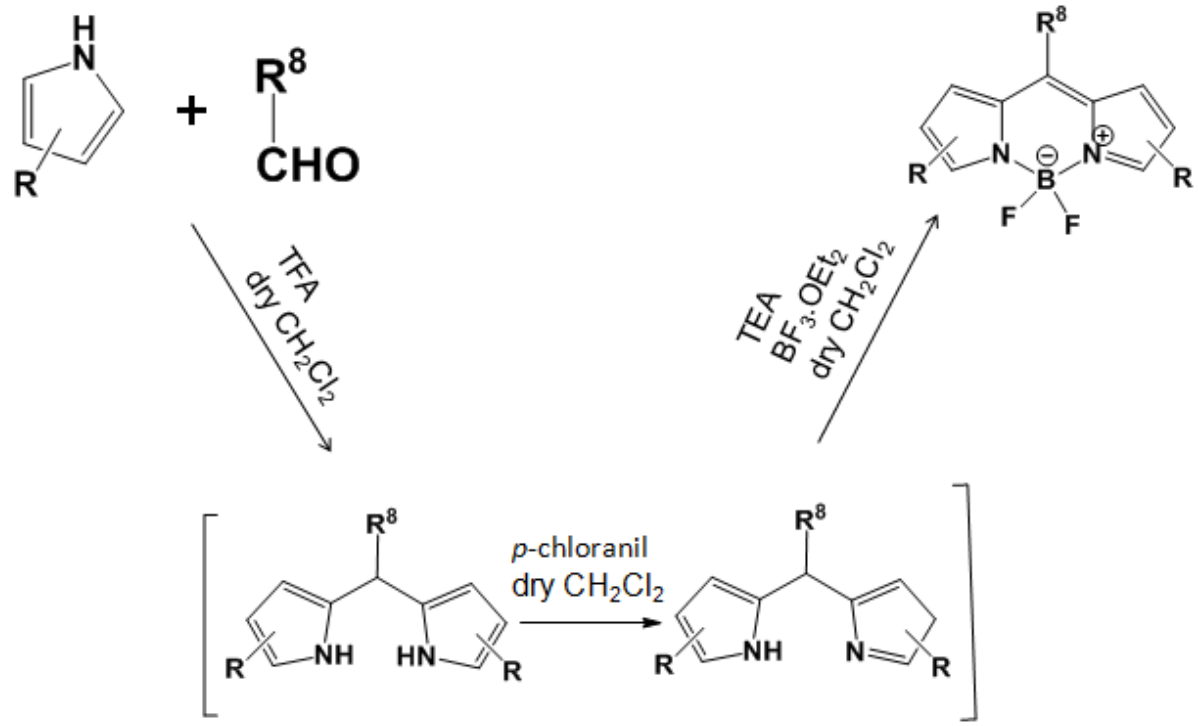

Scheme 3. Symmetric BODIPY synthesis using different aldehydes and pyrrole derivatives.

1.1.3. Functionalisation of the BODIPY core

BODIPY dyes are renowned for their structural flexibility [2]. Different functionalities can be added at virtually every position on the core. In this section, various ways in which substituents are added onto the BODIPY core and their impacts on the photophysical properties of the dye are explored.

1.1.3.1. Functionalisation via the C8 or meso-position

A facile way to add the desired substituents at the *meso*-position of a BODIPY core is to start the synthesis with an aldehyde containing the desired functional group. To prevent rotation of aromatic groups at the *meso*-position, substituted pyrrole units with methyl groups are used for the acid-catalysed condensation reaction, for their dual role of also preventing polymerisation of the pyrrole units and stabilising the BODIPY core [24]. In this regard, the resultant orthogonal geometry serves to minimise electronic coupling between the dye and the *meso*-substituent [24]. Substituents at the C8-position can greatly affect the fluorescence properties

of the dye through photo-induced electron transfer processes, leading to quenching of fluorescence emission as a result of a low lying charge transfer states between the BODIPY core and the *meso*-substituent [25]. Suitable substitution at the *para*-position of the *meso*-aryl substituent can enable the addition of other functional groups, conjugation with macromolecules and can enhance water-solubility [14]. Studies have also explored the replacement of the *meso*-carbon with a nitrogen atom, and the resulting aza-BODIPY dyes have been found to absorb strongly in the NIR region [14].

1.1.3.2. Electrophilic Substitution at the 2,6-positions

The 2,6-positions of BODIPY dyes are susceptible to electrophilic substitution reactions [26]. This is useful because 1,3,5,7-tetramethylBODIPY core dyes have high fluorescence quantum yields since little or no intersystem crossing (ISC) to the triplet excited state occurs on photon absorption, and most of the energy absorbed on excitation is lost through radiative relaxation in the form of fluorescence [27]. In this regard, unsubstituted BODIPY core dyes are usually unsuitable for applications in PACT and photocatalytic degradation, since these applications depend on singlet oxygen generated through ISC to the triplet state. To encourage ISC, heavy atoms such as halogens (Br, I) are incorporated at the 2,6-positions, and this relaxes the spin selection rule, thereby giving rise to BODIPY dyes with reduced fluorescence quantum yield and enhanced ISC to the triplet state [27].

The incorporation of halogens at the 2,6-positions is also known to cause a red shift of the main BODIPY absorption wavelength. Halogen atoms can cause both electron-withdrawing inductive effects and an electron-donating mesomeric effect through the interaction between the lone pairs of electrons and the BODIPY core [26,27]. As a result, there is a relative destabilisation of the highest occupied molecular orbital (HOMO) energy, which has larger MO coefficients at the 2,6-positions than is the case with the lowest unoccupied molecular orbital (LUMO), and a narrowing of the HOMO−LUMO energy gap [27]. It should be noted

that the electrophilic addition of bromines or iodines at the 1,3,5,7-positions would be preferred if the core dyes were unsubstituted [28,29]. Studies have also noted a nonlinear relationship between increasing the number of halogen atoms beyond two and the extent of the heavy atom effects on the photophysical properties of the dyes [29].

1.1.3.3. Modification of the 3,5-methyl substituents

BODIPY dyes bearing methyl-groups on the 3,5-positions are acidic enough to undergo base-catalysed Knoevenagel type condensation reactions [14]. This procedure has been used to introduce styryl moieties at the 3,5-positions with the aim of inducing a bathochromic red-shifting of absorption and emission maxima of the BODIPY chromophore to the NIR region [14]. This involves Knoevenagel condensation reactions [2,14] at the 3,5-position methyl groups with aromatic aldehydes; normally this reaction requires basic conditions and also involves an azeotropic removal of water through a Dean-Stark apparatus to afford styryl extended BODIPY chromophores. Large bathochromic shifts in the absorption maxima of the main spectral band of the BODIPY chromophore occur because there is an uneven distribution of molecular orbital (MO) coefficients at the 3,5-methyl positions, causing a relative destabilisation of the HOMO energy with respect to the LUMO. This results in a narrowing of the HOMO−LUMO energy gap and a shift of the main BODIPY absorption band maximum towards the NIR region [14].

The 3,5-methyl substitutions can also be used to introduce different functional moieties onto the BODIPY chromophore for further conjugation to nanoparticles, a property which is of interest to this study. Studies by Yogo et al. [30], have shown that the presence of good leaving groups (such as iodine or chlorine) at the 3- and/or 5-positions make it possible for electron-deficient BODIPY dyes to undergo nucleophilic aromatic substitutions and transition metal-catalysed cross-coupling reactions (Suzuki, Heck, Sonogashira and Stille) [30]. Modification of 3,5-dichloroBODIPYs by substitution with carbon, nitrogen, oxygen and sulfur nucleotides

has been carried out with the aim of obtaining large bathochromic shifts in the absorption and emission maxima [31]. This procedure has made it possible to introduce various aryl, ethenylaryl, and ethynylaryl substituents by making use of palladium-catalysed Suzuki, Heck, Sonogashira and Stille coupling reactions (**Scheme 4**) [31]. The synthesis of novel BODIPY-based fluorescent materials for biosensing and labelling is made possible. During these cross-coupling reactions, the B-F bonds remain inert.

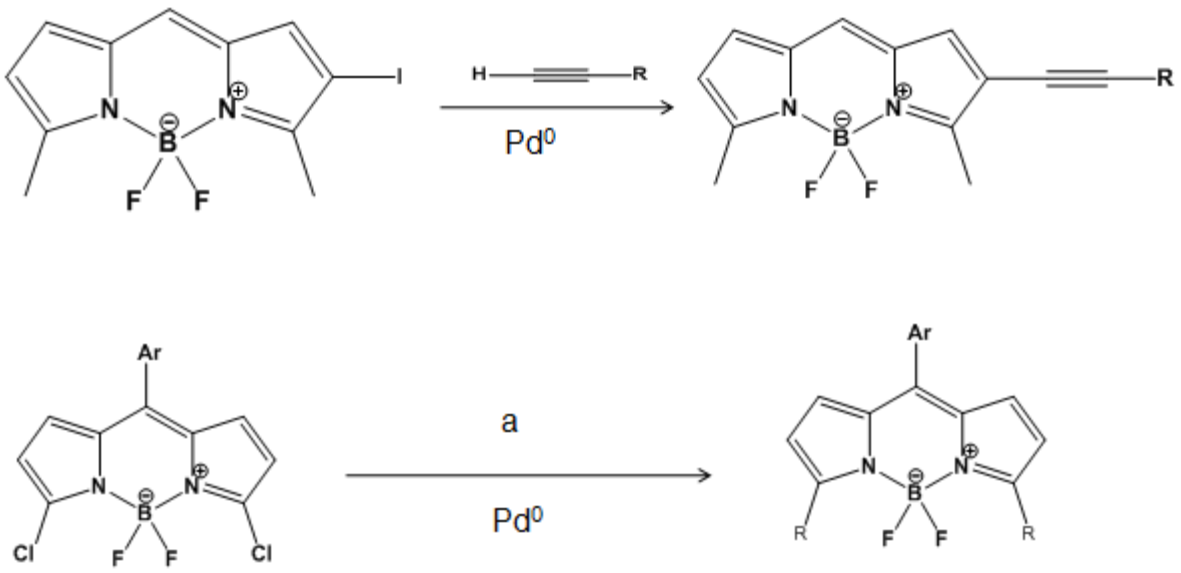

Scheme 4. Examples of palladium-catalysed cross-coupling reactions on a BODIPY core. (a) Reagents: $SNPh_4$ (R=Ph) or $ClC_6H_4B(OH)_2$ (R = p-ClC_6H_4), or styrene R=CHCHPh, or phenylacetylene R=C≡Ph.

1.1.3.4. Modification at the boron centre

The replacement of fluorine atoms at the boron centre was reported recently when it was shown that the fluorine atoms could be substituted with aryl groups [32]. This approach was further developed by Ulrich and Ziessel when they reported the replacement of the fluorine atom with aryl, ethynylaryl and ethynyl subunits [32]. These reactions are usually carried out with an organolithium or a Grignard reagent (**Scheme 5**). The strategy affords scope for the attachment

of one or more aromatic polycycles, and this has led to the fabrication of a new family of highly luminescent, redox-active and photostable dyes called C-BODIPYs, E-BODIPYs, and O-BODIPYs [32]. The attached polycycles are energy-donors, and this creates an energy-donor and energy-acceptor relationship with the parent BODIPY fluorophore. Upon photon absorption, the polycycle rapidly transfers its energy to the acceptor (i.e., the parent BODIPY), due to the significant overlap of the donor emission and acceptor absorption spectra [33]. In this regard, the attached donor acts as a photon harvester and in so doing, addresses key problems associated with BODIPY dyes, such as their small Stokes shifts [34]. Attachment of aromatic polycycles has proven to be a favourable way to extend the π-conjugation system of the BODIPY chromophore. This method is currently being explored by Ziessel, Ulrich, and Harriman whose work has led to many BODIPY scaffold-based dyads, photovoltaics, electroluminescent devices, energy transfer cassettes and supramolecular assemblies [32,34].

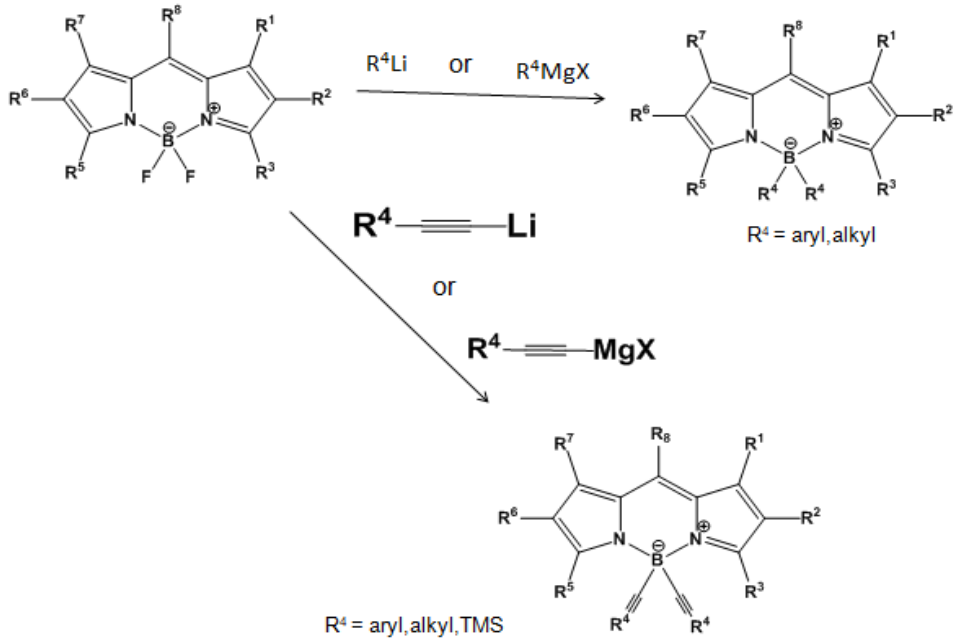

Scheme 5. Selected methods for modification at the boron centre. TMS = Trimethylsilyl.

1.1.3.5. Structurally rigidified BODIPYs

The preparation of structurally-rigidified BODIPYs can be achieved by aromatic fusion onto the BODIPY core. This strategy has led to the generation of long emission BODIPYs as a result of the steric hindrance that is introduced [35]. Structurally rigidified BODIPY dyes can also be prepared through direct annulations of aromatic rings at the β,β'-positions of the parent BODIPY core. For example, fused benzene, substituted benzene, and spiro-fluorene moieties have been generated, starting from either aryl-fused pyrroles or 2-acetyl-phenols **Figure 1.4** [36].

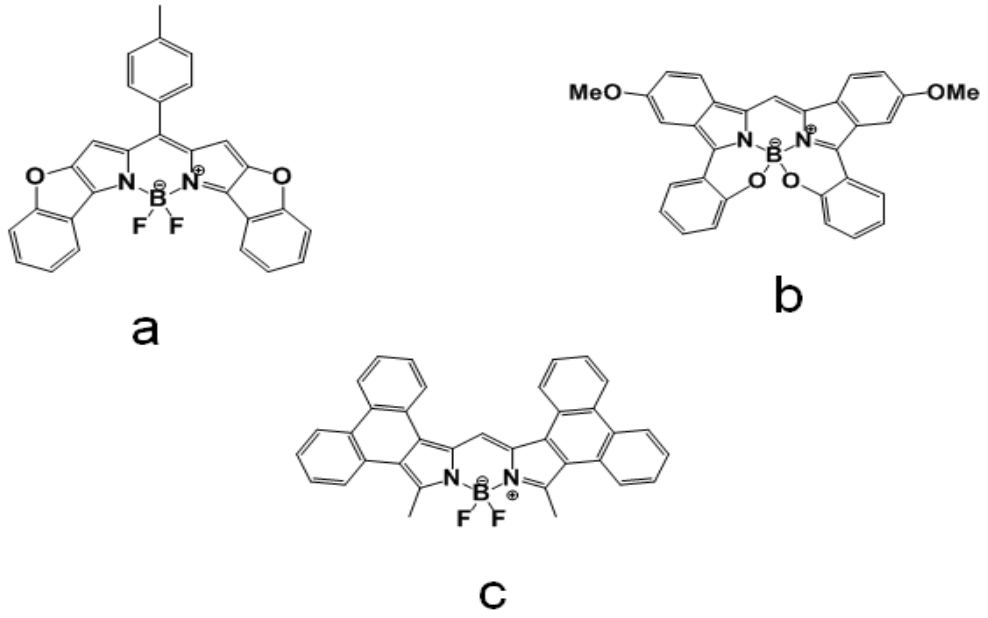

Figure 1.4. Structurally rigidified BODIPY dyes.

1.1.3.6. Replacement of meso-carbon (C8) with a nitrogen atom

When the *meso*-carbon of the parent BODIPY core is replaced by a nitrogen, aza-BODIPYs dyes are formed. The incorporation of a nitrogen atom at the 8-position narrows the HOMO−LUMO energy gap, thereby red-shifting the absorption and emission maxima to the NIR region of the spectrum [37]. Several studies have reported on the synthetic strategies for the fabrication of these dyes [37-40]. Recently the synthesis of both symmetric and asymmetric

aza-BODIPY dyes have been reported, motivated by their potential utility as biological labels, singlet oxygen-generating sensitizers in photodynamic therapy (PDT) and PACT and as luminescent proton sensors.

1.1.4. Physicochemical properties of BODIPY dyes

A Jablonski diagram can be used to provide an illustration of processes that take place upon photon absorption by the ground state (S_0) of the BODIPY dye (**Figure. 1.5**) [41].

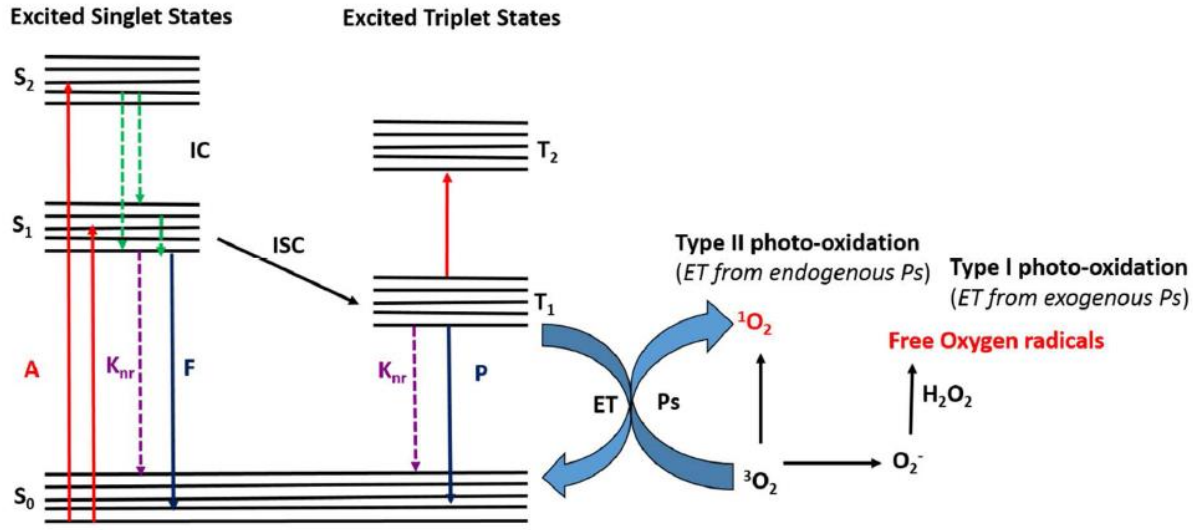

Figure 1.5. A Jablonski diagram highlighting the various electronic transitions that occur upon photoexcitation. These include a transition from the ground state (S_0) to the first singlet excited state (S_1), an internal conversion (IC) process, fluorescence relaxation from the first excited state to the ground state, intersystem crossing (ISC) from the S_1 state to the first triplet excited state (T_1), and relaxation through phosphorescence from the T_1 state to the ground state. The scope also exists for excitation of the molecule to higher S_n electronic states [41].

Upon photoexcitation, an electron on the BODIPY dye gets excited to an unoccupied MO to form short-lived S_n excited states. Through a process of internal conversion that generally occurs within 10^{-12} s, the S_n excited states rapidly relax to the lowest vibrational level of the S_1

state. From the S_1 state, relaxation to the ground state occurs either via fluorescence or by non-radiative emission. This series of processes is consistent with Kasha's rule which states that the fluorescence emission spectra and quantum yields are independent of the excitation wavelength, because the fluorescence process occurs only from the lowest vibrational level of the S_1 excited state. From the S_1 state, a spin-forbidden transition to the first triplet excited states (T_1) is possible through a process of ISC that is encouraged by the presence of heavy atoms on the BODIPY fluorophore [41]. BODIPY dyes in the T_1 state can either transfer their energy to molecular oxygen to generate singlet oxygen and other reactive oxygen species or return to the S_0 state through phosphorescence or non-radiative decay.

1.1.4.1. UV-visible Absorption Spectra.

In the UV-visible absorption spectra of BODIPY dyes, the transition from the ground state to the first excited state ($S_0 \rightarrow S_1$), corresponds to the lowest energy absorption band and it is characterised by a high transition probability, possessing high molar absorption extinction coefficients and oscillator strengths in the orders of $\varepsilon \sim 10^5$ M^{-1} cm^{-1} [14]. The shoulder appearing at higher energies (around 1100 cm^{-1} from the absorption maximum) is due to an out-of-plane vibration of the aromatic C-H skeleton of the BODIPY chromophore [14]. Other absorption bands to higher singlet excited states (S_2, S_3…) are less intense than the $S_0 \rightarrow S_1$ transitions.

The absorption and fluorescence characteristics do not depend significantly on the nature of substituents on the chromophore or on the solvents used to prepare solutions [14], if the substituents do not have strong electron donor or acceptor capabilities. Quantum mechanical calculations predict that the main absorption band for a BODIPY dye with no substituents and C_{2v} symmetry results from an allowed $A_1 \rightarrow B_2$ transition [14]. From the calculations, it can be inferred that the main BODIPY UV-visible absorption band can be assigned to an electron being promoted from the HOMO to the LUMO (**Figure 1.6**), which is polarised along the

molecular axis of the chromophore [42]. It is known that this absorption is independent of dye concentration (at least up to 2×10^3 M), and this provides an indication of a lack of any form of intermolecular dye interactions, such as dye aggregation [42]. This confers an advantage to BODIPY dyes with respect to other dyes, such as rhodamines, because the formation of non- or poorly fluorescent aggregates reduces the fluorescence intensity in concentrated solutions and can also drastically lower the singlet oxygen generating properties of the structurally modified dyes [43].

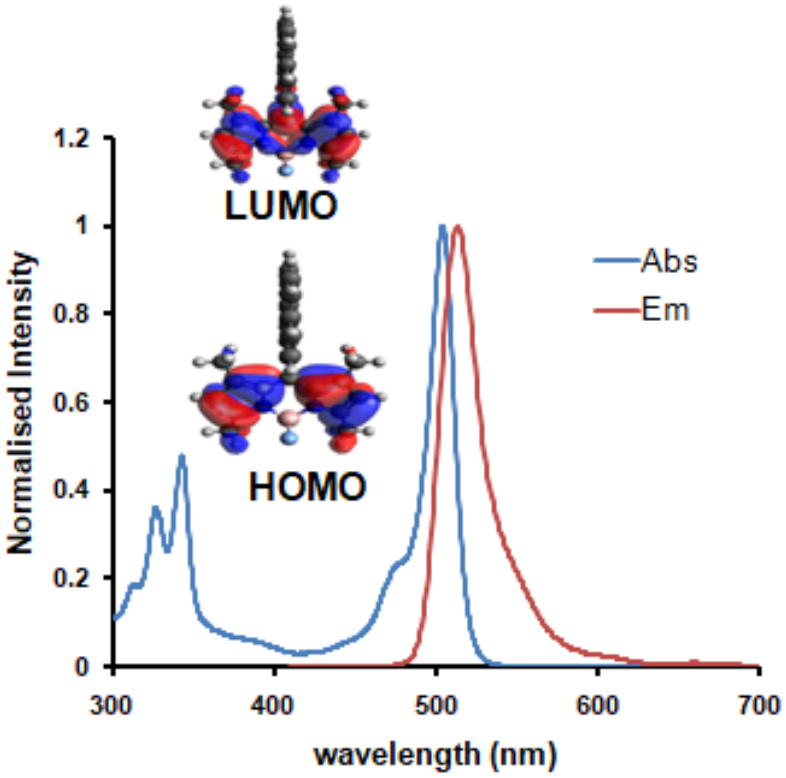

Figure 1.6. Frontier molecular orbitals, highlighting the angular nodal plane patterns of the HOMO and LUMO orbitals (A), and the absorption (blue line) and emission (red line) spectra of a typical BODIPY core dye.

1.1.4.2. Fluorescence and fluorescent quantum yields

The fluorescence spectra of BODIPYs are usually a mirror image of the $S_0 \rightarrow S_1$ absorption band, due to similarities in the vibrational energies in both electronic states [42], since the geometry of the S_1 excited state is typically very similar to that of the ground state [43]. Hence,

the fluorescence band is characterised by a small Stokes shift in the range of 500 cm^{-1}. The morphology of the fluorescence emission band is known to be independent of both the wavelength of excitation and electronic-vibrational levels directly populated in the excitation process, which shows that emission is from the lowest vibrational level of the S_1 excited state, which is populated by a fast internal conversion process from the upper S_n excited states [43]. A mono-exponential decay describes the fluorescence decay curve of BODIPY dyes with lifetimes typically in the 4−6 ns range (**Figure 1.7**) [42]. This value is usually independent of both the emission and excitation wavelengths. The fluorescence lifetime as defined by **Equation 1**, and denotes the time that 1/e of the BODIPY dyes remain in the S_1 excited state before decay to the ground state [44].

$$\tau_0 = \tau_F/\Phi_F \quad (1)$$

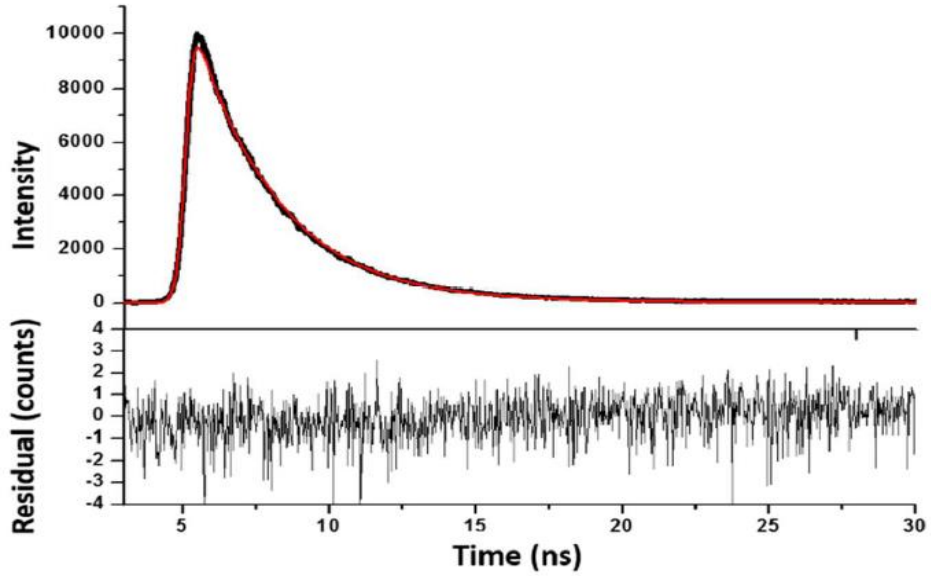

Figure 1.7. A typical monoexponential fluorescence decay curve of a BODIPY dye.

Fluorescence quantum yields can be determined by comparing the integrated intensity of the BODIPY dye and that of a known standard according to **Equation 2**:

$$\Phi_F = \Phi_{F(std)} \frac{F.A_{std}.n^2}{F_{std}.A.n_{std}^2} \quad (2)$$

where F and F_{std} represent the integrated area under the fluorescence decay curves for sample and standard, A and A_{std} are the absorbance values of the sample and reference at the excitation wavelength; while n and n_{std} are the refractive indices of the sample and standard solutions, respectively. The high fluorescence quantum yields of most BODIPY core dyes arise from the rigid delocalised π-system, which is devoid of any cyclic electron flow around the chromophoric ring [45]. Hence, the dye is characterised by low intersystem crossing, according to Drexhage's Loop rule [46]. The low non-radiative deactivation is controlled mainly by the internal conversion processes, which are less likely to occur when a dye has a rigid planar geometry.

1.1.4.3. Singlet oxygen quantum yield of BODIPY dyes

Singlet oxygen generation by BODIPY dyes is of great importance as it enables the application of the dye in PDT, PACT and the photocatalytic degradation of organic pollutants in industrial wastewater. The first triplet excited state T_1 is known to be the key intermediate that leads to the formation of singlet oxygen, but studies have shown that BODIPY dyes usually exhibit negligible ISC to the triplet manifold [2,14]. This is attributed to the disruption of the cyclic π conjugated system by the BF_2 linking group that stops cyclic electron flow, thereby forming a rigid delocalised π-system with high fluorescence quantum yields [1,2]. To encourage ISC, the incorporation of heavy atoms, such as Br or I, onto the BODIPY core, encourages spin-orbit coupling. The triplet state BODIPY dye then transfers its energy to molecular dioxygen in a Type II process to generate singlet oxygen, or in a Type I process where an electron is transferred to form other ROS such as superoxides.

The facile incorporation of heavy atoms onto the BOIDPY chromophore has proved to be a useful approach to enhance ISC as well as causing a bathochromic shift in the main BODIPY absorption band [47]. The mesomeric structure of BODIPY dyes causes the 2,6-positions in BODIPY dyes to be more susceptible to electrophilic substitution as these positions are less positively charged [13]. In this study, a similar approach was used to incorporate bromines and iodines at the 2,6-positions of a series of BODIPY dyes to encourage singlet oxygen generation for the intended applications. There are two methods to quantify singlet oxygen generation. Firstly, the use of a germanium detector to monitor singlet oxygen phosphorescence, and secondly a comparative method that was used in this study. The comparative method involves the use of a singlet oxygen scavenger, such as 1,3-diphenylisobenzofuran (DPBF) to monitor singlet oxygen production in an oxygenated environment [15]. The rate of photooxidation of DPBF is then monitored using UV-visible absorption spectroscopy. **Equation 3** is used for the quantification of singlet oxygen quantum yield (Φ_Δ) in this context [15]:

$$\Phi_\Delta = \Phi_\Delta^{std} \cdot \frac{R^{sample} \cdot I^{std}}{R^{std} \cdot I^{sample}} \quad (3)$$

where Φ_Δ^{std} is the singlet oxygen quantum yield for the standard (Rose Bengal, Φ_Δ^{std} = 0.76 in ethanol) [48], R^{sample} and R^{std} are the DPBF photo-bleaching rates in the presence of the sample and standard, and I^{sample} and I^{std} represents the rates of light absorption, which cancel if the optical densities of the solutions are the same.

Studies to determine the Φ_Δ value of the BODIPY dye embedded in nanofibres were carried out using the direct chemical method due to a lack of suitable standards. The studies were performed in unbuffered aqueous solution using anthracene-9,10-bis-methylmalonate (ADMA)

as a singlet oxygen scavenger. The modified fibres were suspended in the aqueous solution of ADMA and irradiated using a photolysis set up with a light-emitting diode. Φ_{ADMA} was first calculated using **Equation 4** [15]:

$$\Phi_{ADMA} = (C_0 - C_t).V_R / I_{Abs}.t \quad (4)$$

where C_0 and C_t are ADMA concentrations before and after irradiations, V_R is the solution volume; t represents irradiation time per cycle and I_{Abs} is defined by **Equation 5**:

$$I_{Abs} = (\alpha.A.I) / N_A \quad (5)$$

where $\alpha = 1-10^{-A(\lambda)}$ and $A(\lambda)$ is the absorbance value of the sensitizer at the irradiation wavelength, A is the irradiated area, I is light intensity, and N_A is Avogadro's constant. Singlet oxygen calculations were carried out with **Equation 6**:

$$1/\Phi_{ADMA} = (1 / \Phi_\Delta) + (1 / \Phi_\Delta). (K_d / K_a). (1 / [ADMA]) \quad (6)$$

where K_a denotes the rate constant for the reaction of ADMA with $^1O_2$, and K_d represents the decay constant of singlet oxygen. The Φ_Δ value is obtained from the intercept of the plot of $1 / \Phi_{ADMA}$ against 1 / [ADMA]. In **Equation 5**, the absorbance value used is that of the BODIPY modified nanofibres, and this was measured by placing the fibres on a glass slide. Since some of the incident light is expected to be scattered, the Φ_Δ value of BODIPY dyes in the fibre should be viewed only as an estimate.

1.2. Nanoparticles

In nanotechnology, nanosized materials can be defined as particles with sizes ranging between 1 and 100 nanometres. Nanoparticles are composed of carbon, metal, metal oxides and organic matter. Due to their nanoscale range sizes, these particles possess unique physicochemical properties compared to their bulk material. These unique properties include their relatively larger surface area to volume, increased reactivity or stability in chemical processes, and

enhanced mechanical strength. This has enabled the exploitation of nanoparticles in diverse fields, such as medicine, cosmetics, renewable energy, environmental remediation, and biomedical devices, [49,50]. In this study, attempts were made to conjugate BODIPY dyes to magnetic nanoparticles to enhance their photocatalytic and photosensitising properties.

1.2.1. Magnetic Nanoparticles (MNPs)

Metal oxide nanoparticles (NPs) have found applications in diverse fields because of their unique optical, electronic and magnetic properties in comparison to the bulk materials [51]. The drawbacks in the application of metal oxide nanoparticles are that bare Fe_2O_4 magnetic nanoparticles (MNPs) agglomerates in solution. To overcome these problems, magnetic nanocomposites are used instead [51]. Spinel ferrites of the form MFe_2O_4 (M = Pd, Si, Co) have been the subject of considerable attention because of their stronger magnetic properties, higher chemical resistance to oxidation and larger surface areas when compared to iron oxide NPs [52]. MFe_2O_4 is also very stable in acidic media (pH 2.0−6.0), making it suitable for applications through a broad pH range [53]. Amongst various spinel ferrites, cobalt ferrite ($CoFe_2O_4$) have received special attraction due to their unique physical properties such as high Curie temperatures, large magnetocrystalline anisotropy, high coercivity, moderate saturation magnetisation, large magnetostrictive coefficient, and excellent chemical and mechanical stabilities [49]. These unique characteristics enabled their applications as anode materials in the commercial manufacture of lithium-ion batteries, as adsorbents [52], in sensors [54], magnetic devices [51], biomedicine [53], in catalysis, and in PACT [55].

Studies have shown that in photocatalysis, semiconductors with narrow band gaps are more suitable than those possessing wide band gaps, due to their ability to use visible light [56]. Ferrites due to their chemical and thermal stability possess important photocatalytic properties for many industrial applications. Some of these industrial processes include the oxidative dehydrogenation of hydrocarbons, the decomposition of alcohols and hydrogen peroxides, and

the treatment of exhaust gases [50,51]. Properties of ferrites are strongly dependent on the size, nature, and number of metals incorporated into the structure [57]. The presence of the different metals in the lattice structure is known to modify the redox properties of ferrites and influence their stability while maintaining the spinel structure. The spinel structure of ferrites enhances photocatalysis providing an extra catalytic site by virtue of the crystal lattice [57]. Photocatalytic degradation is known to be enhanced by the presence of ferrites, because upon visible light absorption, an electron is excited from the valence band (VB) to the conduction band (CB), so that a photogenerated positive hole is created [56]. The e^-/h^+ pair facilitates redox reactions that give rise to ROS that facilitate the photodegradation of contaminants [57]. Composites of ferrites and dyes such as BODIPYs and phthalocyanines that have been structurally modified to enable the heavy atom effect, improve ROS generation, thereby enhancing the photocatalytic and PACT processes. Hence the use of ferrites as visible light photocatalysts has proven promising not only for environmental purification but in wastewater remediation through degradation of organic pollutants.

Depending on the synthetic procedure, parameters such as particle size, size distributions and magnetic properties of cobalt ferrites can be modified which also impacts on the applications of the nanoparticles especially in photocatalysis and PACT [53,58]. Conventionally, NPs are prepared by the following methods; sol-gel processing, hot spraying, evaporation-condensation, matrix isolation, laser-induced vapour phase reactions and aerosols [53]. The major drawbacks of these synthetic methods are that control of particle size and size distribution, which affects the magnetic properties of the MNPs, is very difficult [59]. In contrast, cobalt ferrite synthesis by the wet chemical method (coprecipitation) ensures control of both the size and size distributions by controlling the nucleation and growth rate [57]. During synthesis, the rate of nucleation should be adjusted to be higher than the growth rate in order to obtain smaller sized particles that are uniformly distributed [56-58]. Other advantages

include removal of the need for extra mechanical or microwave heat treatment as well as production control when large amounts of particles synthesis are required.

The issue of agglomeration is an unavoidable problem associated with nanoparticles as they tend to reduce the energy associated with the high surface area to volume ratio. Also, bare MNPs are highly reactive and are easily oxidised in air resulting in loss of magnetism and dispersibility [50]. Hence, it is crucial to develop protection modalities to chemically stabilise bare magnetic nanoparticles during or after synthesis [51]. Some of these strategies include coating with organic species such as surfactants or polymers or with an inorganic layer such as silica or carbon [51]. These protections not only serve to stabilise the nanoparticles to provide a longer shelf life but can also be used for further functionalisation with various ligands or other NPs, depending on the desired application. In this work, spherical, silica capped cobalt ferrite magnetic nanoparticles were synthesised according to a previously reported chemical procedure [50,51].

1.3. Electrospinning

In this work, BODIPY dyes were embedded in electrospun nanofibres to enable the photocatalytic degradation of azo dyes. Hence the methodology of electrospinning needs to be addressed. The electrospinning technique is a simple method of nanofibre fabrication using electrostatic forces with working principles akin to that of electrospraying [60]. The popularity of this technique is due to its simplicity, cost-effectiveness, and versatile utility to seemingly any synthetic and many natural polymers to produce uniform, continuous nanofibres with diameters ranging from several micrometres to tens of nanometres [61]. The scope also exists for industrial-scale applications of the electrospinning process. In order to obtain continuous fibres of uniform diameter and morphology, the optimisation of several parameters is required. The electrospinning parameters can be divided into (i) solution parameters (polymer concentration, viscosity, and nature of the solvent), and (ii) working parameters (flow rate,

voltage, and tip to collector distance). Both sets of parameters determine the spinnability of the solution or the overall occurrence of the electrospinning process [60,61]. Hence, for successful electrospinning, the dissolution of the polymer of adequate molecular weight in a solvent/solvent mix with suitable conductivity, surface tension, and vapour pressure is a prerequisite [62], coupled to having a solution concentration that is moderately high. These factors determine the viscosity of the polymer solution, and hence determine the ease of flow during the electrospinning process.

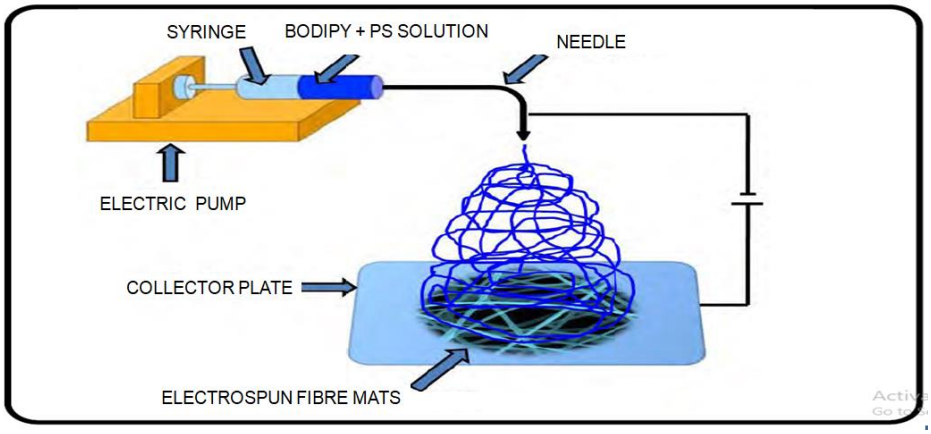

Figure 1.8. Typical diagrammatic set-up of an electrospinning apparatus.

The basic laboratory set-up of an electrospinning apparatus includes; a syringe fitted with a metal needle at the tip (spinneret) mounted on a syringe pump, a high voltage supply source with connections to the needle and a metal collector where the fibre mats are deposited [63]. The syringe pumps are responsible for the flow of the polymer solution towards the tip of the needle where a spherical droplet forms [63]; an applied high voltage at the cathode increases gradually until the applied potential overcomes surface tension. The spherical droplets are distorted to form so-called “Taylor cones” [62]. Consequently, a jet of polymer solution flies towards the collector plate (anode), where on cooling and solvent evaporation nanofibrous membranes form. The facile and versatile modifications of nanofibre surfaces, tailor-made to suit desired applications have led to increased attention in their potential utility in many

applications including; filtration, composites, scaffolds, and in medical applications [63]. Electrospun nanofibres, their nanoscale size ranges notwithstanding, have the advantages of being highly porous, due to the high-surface-to volume ratio and small pore sizes [61-63]. In this thesis, the main interest in using nanofibres relative to other supports lies in their ability to be easily modified with embedded BODIPY dyes for specific applications.

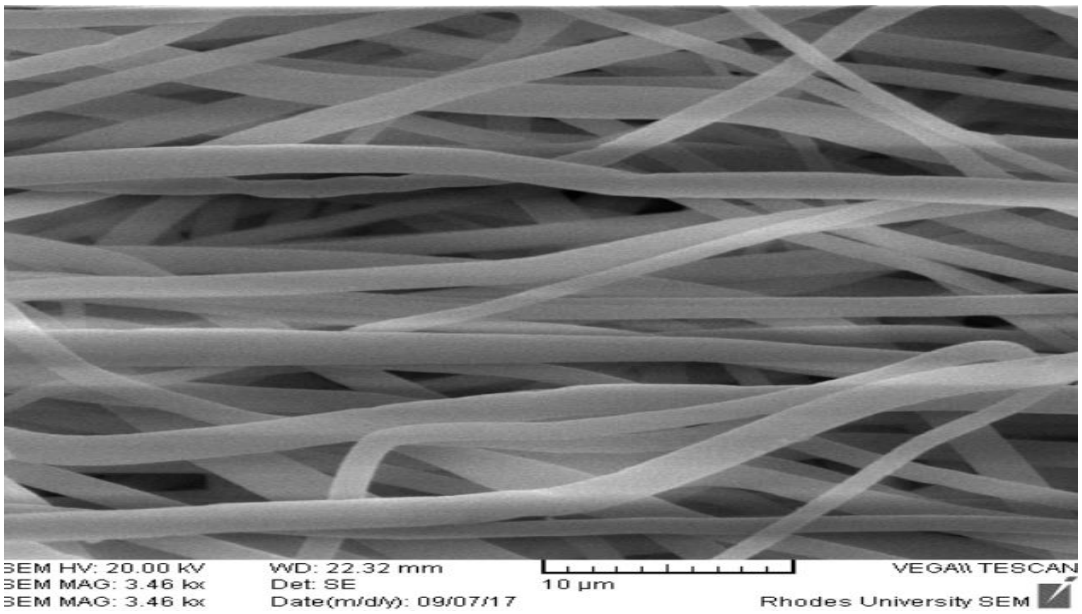

Figure 1.9. Typical scanning electrode microscope (SEM) image of a polystyrene electrospun nanofibre [62].

Integration of functional molecules into the fibre core has led to applications in diverse fields such as in biosensor technology, tissue engineering, drug delivery, heterogeneous catalysis and nanoelectronics [62]. In this thesis, the aim is to functionalise fibres with BODIPY dyes for potential applications in PACT and the photocatalytic degradation of azo dyes in industrial wastewaters. It has been reported that BODIPY dye modified nanofibre mats did not change the physicochemical properties of the dye in the fibre mats [64]. Although the use of BODIPY dyes as photocatalysts in organic transformations has been reported previously [64], up to the time of the research reported in this thesis, there had been no previous studies of the potential

utility of BODIPY dyes modified nanofibres for the photocatalytic degradation of organic dye pollutants.

1.4. Applications of BODIPY dyes

The application of BODIPY dyes in various fields such as molecular biological labelling, cell imaging, chemical sensing, solar cells, and two-photon absorption, has been inspired by their unique properties [1,2,14]. In this study, one of the major aims was to investigate their applications in PACT, the phototransformation/degradation of organic pollutants, and as optical limiting materials.

1.4.1. Photodynamic antimicrobial chemotherapy

In the 20th century, antibiotics were a breakthrough discovery that made treatment of many microbe related diseases that hitherto eluded treatment possible [65]. This led to a decrease in bacteria-related infections that can be observed at the beginning of the 21st century. However, the widespread use of antibiotics led to the emergence of antibiotic resistance and multi-drug resistance microbial strains [66]. The clinical isolation of methicillin-resistant *Staphylococcus aureus* (MRSA), with reduced susceptibility to vancomycin, was reported in 1996 [67]. In 2002, a vancomycin-resistant *Staphylococcus aureus* was also documented. MRSA caused infections have been difficult to treat, and infected patients are often infected for many months and can require long hospitalisation [65]. Furthermore, the emergence of mupirocin (Bactroban) resistance in MRSA, underscores the urgent need for the development of novel, localised, treatment alternatives to the standard antibiotic treatment. In this regard, PACT has shown potential to be an alternative antimicrobial remedy and already has proven its effectiveness *in vitro* against bacteria, viruses, and protozoa [65-68].

1.4.1.1. Background and working principle

In 1890, Oscar Raab published the first paper on the photodynamic effects of dyes on the activities of microorganisms when he investigated the light-dependent phototoxicity of acridine hydrochloride against *Paramecium caudatum* [69]. However, further studies and practical applications of this phenomenon did not appear until the second half of the 20th century with its proposed utility as an anti-tumour agent preceding the subsequent antimicrobial studies [68]. In both PDT and PACT, the basic principles involve photoinactivation of tumour cells or microbes using photoactive dyes called photosensitisers that are non-toxic or of low toxicity in the dark in an oxygen-containing medium [65,68]. A non-toxic photosensitizer localised in specified target cells can be activated by a low dosage of visible light of appropriate wavelength (**Figure 1.8**), to generate cytotoxic singlet oxygen species via the Type II mechanism [67].

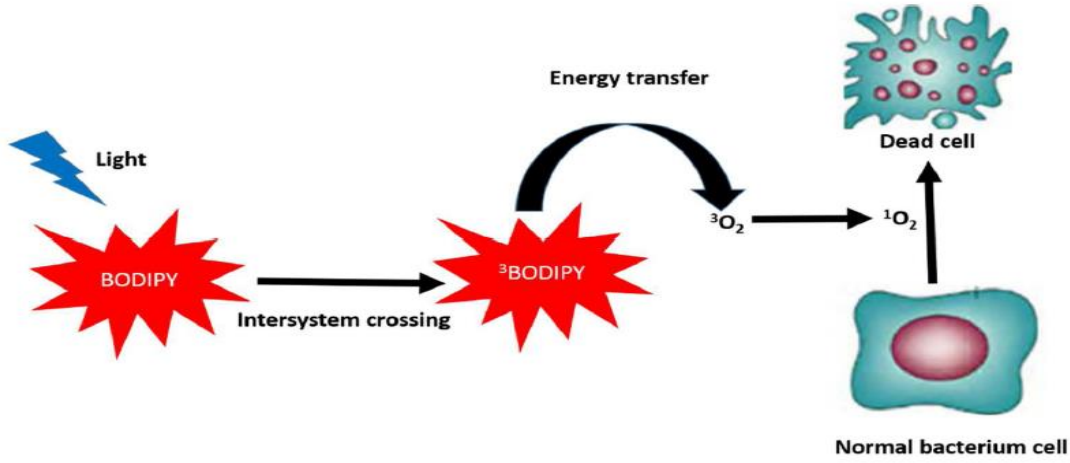

Figure 1.10. Schematic diagram showing processes culminating in cell death during PACT.

The ability of a molecule to instigate singlet oxygen formation depends on there being sufficiently populated triplet state molecules, which in turn depends on the rate of decay of both the triplet state and the initially formed singlet states. To ensure production of sufficiently populated triplet states, heavy atoms are incorporated into the photosensitising agent which encourages ISC through spin-orbit coupling, preventing radiative deactivation through

fluorescence or non-radiative deactivation through internal conversion by heat production. Also, since radiative deactivation through phosphorescence is a spin forbidden process, sufficient production of triplet state excited photosensitiser molecules is ensured [13]. The molecules then transfer its energy through the Type II process to generate singlet oxygen, the cytotoxic agent that is primarily responsible for antimicrobial inactivation.

Studies have shown that bacterial inactivation occurs mainly through outer membrane damage. Typically, neutral anionic or cationic photosensitiser molecules can destroy gram-positive bacteria [70]. In the case of gram-negative bacteria, cationic photosensitisers or strategies that can disorganise the gram-negative permeability barrier are required [70]. The difference arises from the cell wall make-up of both kinds of bacteria. Gram-positive bacteria have a cytoplasmic membrane that is surrounded by a relatively porous peptidoglycan layer and lipoteichoic acid that allows the photosensitiser molecules to easily access the inner membranes [70]. In gram-negative bacteria, however, the cell wall consists of an inner and an outer membrane which envelops the peptidoglycan layer, creating an effective permeability barrier between the microorganism and its environment which tends to restrict the penetration of many photosensitiser molecules [67, 70].

PACT has been demonstrated to be effective against gram-negative and gram-positive bacteria, yeasts, fungi, protozoa, and viruses, and is advantageous over antibiotics as it does not lead to the formation of antibiotic-resistant bacterial strains [71]. In this instance, PACT is considered as an alternative to antibiotics. The development of novel photosensitisers with improved photo-bacterial activities remains an important research goal.

1.4.2. Photo-oxidation of pollutants

Photocatalytic degradation of environmental pollutants recalcitrant to both light and normal aerobic degradations using photo-generated singlet oxygen has garnered a lot of interest, since it does not lead to the release of harmful by-products [4]. Hence, in this study, it is used for the degradation or mineralisation of azo (Orange G and Methyl Orange) dyes, which are often present in industrial wastewater [5]. Azo dyes typically contain a coupling between a diazotised amine and an amine or a phenol and possess one or more azo linkages [60]. Due to their chemical stability and versatility, azo dyes represent more than 50% of all dyes in common use [60]. They are extensively used in the textile, pharmaceutical and food industries where they are used as colourants [61]. Studies have shown that about 10% of these dyes ultimately end up in industrial wastewater and are released into the environment. The indiscriminate disposal of azo dyes poses a serious threat to human and animal health as they are both carcinogenic and mutagenic [60,61]. Current treatment modalities such as coagulation, activated carbon adsorption, and membrane filtration are known to be non-destructive, so complete degradation, or mineralisation of dye pollutants has been elusive [72,73]. Therefore, the development of destructive processes that enable the complete degradation or mineralisation of azo dyes is an important research goal.

Photocatalysts are a class of materials that provide a relatively simple means for the conversion of solar energy for use in photo-oxidation and reduction processes [72-74]. Photo-oxidative degradation is viewed as a "green" chemistry process, considering the use of abundant natural resources: (a) oxygen (from the atmosphere as the oxidant), (b) water as a solvent, (c) and visible region light (often from solar radiation) [75]. During photocatalysis, reactive oxygen species, such as $^1O_2(^1\Delta_g)$, are used in mineralising pollutants to less hazardous elements. Photosensitiser dyes generate $^1O_2$ upon irradiation with light of appropriate wavelength [76]. In recent years, there has been considerable interest in the use of phthalocyanines, which absorb

strongly at the red and blue ends of the visible region, as photocatalysts for the degradation of organic dye pollutants in wastewaters [77,78]. The absence of significant absorbance in the green portion of the visible region means that not all of the incident light can be absorbed when white light sources are used, so introducing a second chromophore that absorbs in this region, such as a halogenated BODIPY core dye, could further enhance the utility of photosensitiser dyes embedded polymer nanofibres for the photodegradation of organic pollutants. Immobilisation of the photocatalysts in organic or inorganic supports is essential because heterogeneous systems allow for easy separation from the reaction product and re-use of the catalysts [78]. This study reports the first use of BODIPY dyes embedded in electrospun nanofibres for the photocatalytic degradation of azo dyes (Orange G and Methyl Orange).

1.4.3. BODIPY dyes in NLO

Non-linear optics is a branch of physics that describes how changes in light propagation characteristics such as frequency, amplitude, and phase, occur when intense electromagnetic fields interact with various media [79]. The nonlinear effects that occur as a result of changes in the optical response of a material as a function of high light intensity are applied in various optical devices which include: optical rectifiers, optical switches, dynamic holography, optical data recording and optical limiters [80]. Research in optical limiting aims at developing novel techniques to protect sensitive optical materials, such as the human eye and optical sensors from high-intensity laser irradiation [81]. Optical limiting materials are able to attenuate the output fluence of emerging high-intensity beam such as that from a laser while allowing only a beam of safe intensity to be transmitted (**Figure 1.11**) [82]. Hence, an inverse relationship exists between transmittance and the high-intensity light when an optical limiting material is used, since increasingly high-intensity light leads to decreasing transmittance while exhibiting high transmittance to low-intensity light [82]. In this regard, a good optical limiting material

must be able to show the dual property of allowing high transmittance of low-intensity light while reducing the intensity of an optical beam by limiting the output fluence at high intensity [80]. These materials differ from filter goggles worn for safety purposes against laser irradiation in laboratories as these completely filter out all of the incident light. In contrast, optical limiters allow the transmission of safe intensity light while blocking high-intensity light that has the potential to cause harm [82]. Applying various nonlinear optical mechanisms, a good optical limiting material ensures the linear transmittance of low-intensity light up to a limiting intensity, I_{lim}, after which it functions to attenuate the high-intensity light (**Figure 1.12**) [79,80-82].

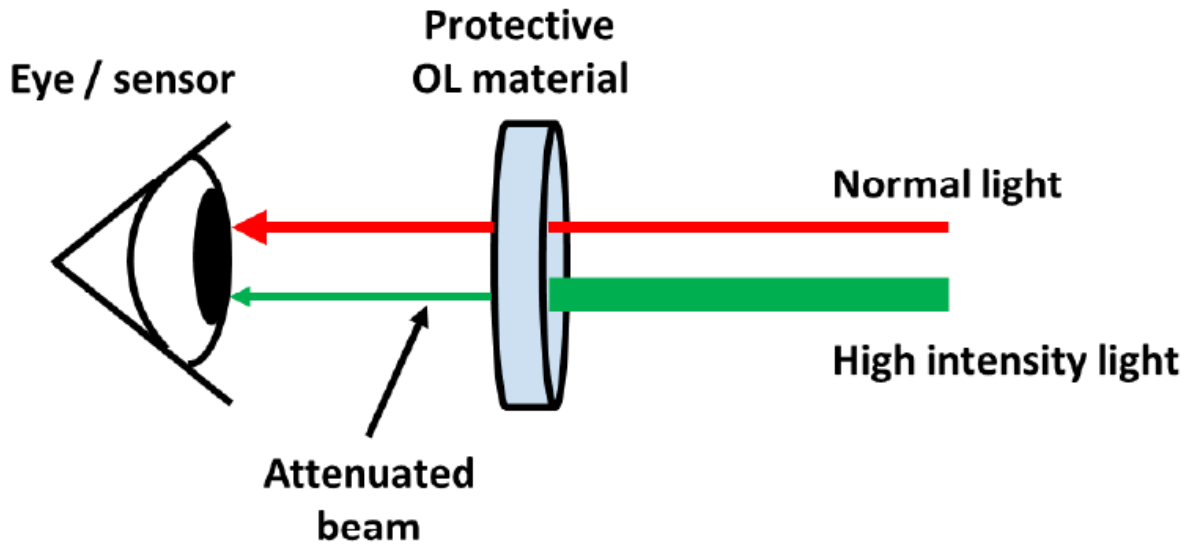

Figure 1.11. Schematic representation of the ideal behaviour of an optical limiting material, under ambient and high-intensity light.

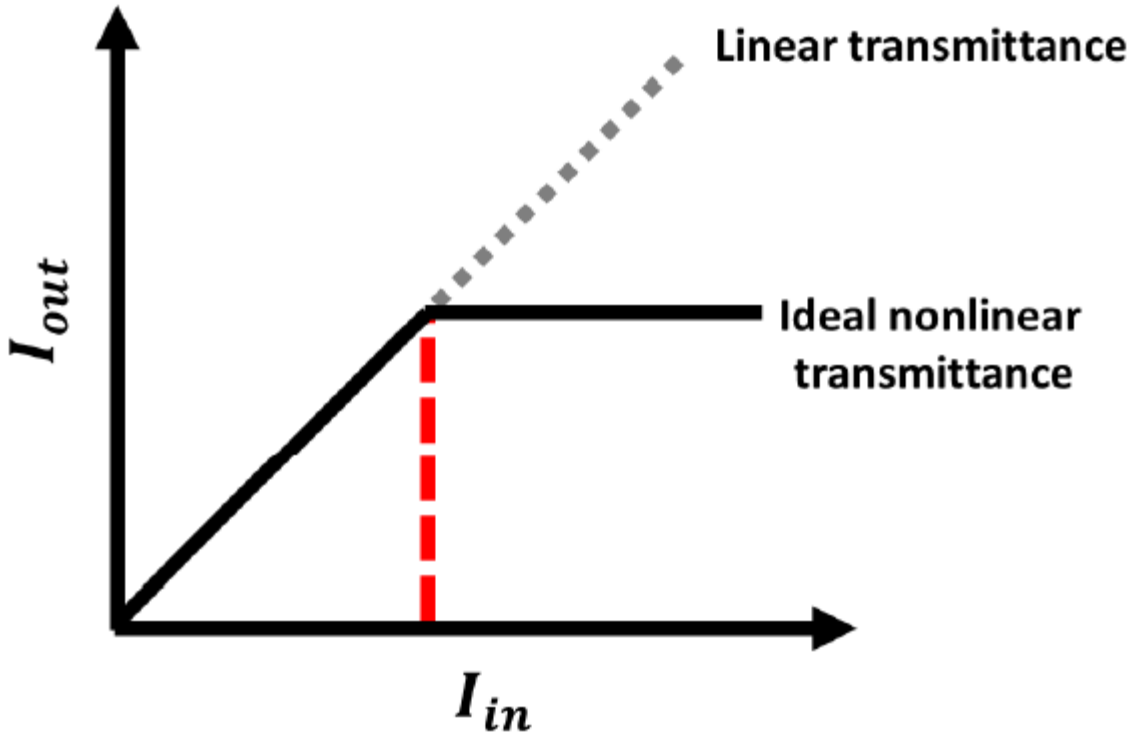

Figure 1.12. The response of an ideal optical limiting material, with the red, dashed line denoting the point at which the transmittance deviates from linearity, which is referred to as the limiting intensity. I_{in} and I_{out} are the incident and transmitted intensities, respectively.

The devices used for optical limiting fall into two classes: active or passive. The functioning of active OL devices depends mainly on internal feedback mechanisms of moving parts, which elicits responses that eventually lead to the regulation of light intensity [83]. The response to an increase in intensity culminates in physical changes that regulate the high-intensity light [84]. In an active OL device, a thermally-induced change in optical properties such as refractive index is required in order to elicit the response. This dependence on heat-induced changes is a major drawback because it has the potential to cause permanent damage prior to noticeable optical changes [83,84]. In passive optical limiting, changes in a nonlinear absorption property of a given material as a function of high-intensity light are used to generate an optical limiter

[85]. Hence, mitigating against reliance on feedback mechanisms, since it depends on the intrinsic ability of materials to exhibit nonlinear absorption responses with decreasing transmissivity in relation to increasing input laser intensity [86]. In this regard, there is a faster response since the OL properties are dependent on the physical properties and not on the response time of moving parts. Passive OL is now the preferred approach for use in protecting sensitive detectors and eyes from high-intensity light.

The quest for ideal OL materials is a research area that is not yet exhausted since the OL materials that have been developed elicit either low NLO responses (e.g., semiconductors) or there are major difficulties in processing them into thin films and or in there being miniaturised into micro-optoelectronics devices (e.g., ferroelectric crystals) [84]. The emergence of organic materials in the mid-1980s revolutionised the field of nonlinear optics due to the ability of these materials to elicit large and rapid nonlinearities [87]. Additionally, organic materials are easily tailored by rational modifications of their chemical structure to fine tune the NLO properties. Finally, the goal of device miniaturisation is made possible by working at the molecular level. The strong nonlinearities in certain organic materials stem from their highly delocalised π-electrons [87]. The delocalised conjugated π-electron system affords high polarisability with a concomitant rapid redistribution of electronic charge upon interaction with intense incident laser radiation [88]. Studies have investigated several organic dyes. For example, phthalocyanines are known to be effective optical limiters due to their highly extended and delocalised macrocyclic π-electron systems [89]. Facile modifications of phthalocyanines reduce the symmetry and enhance polarisability while introducing significant dipole moments [88,89]. Mack and coworkers have recently demonstrated that the lower C_{2v} symmetry of BODIPY dyes and their facile modification to achieve extended π-conjugation through the addition of styryl groups at the 3,5-positions makes these dyes potentially suitable for use as optical limiters [90-92]. Addition of styryl groups shifts the main absorption band to longer

wavelengths, so there is minimal absorbance at 532 nm. Since the second harmonic of Nd:YAG lasers lie at 532 nm, these modifications make these dyes suitable candidates for use in optical limiting.

1.4.3.1. Mechanisms in optical limiting

Three mechanisms have been explored in the study of passive optical limiting; nonlinear absorption (NLA), nonlinear refraction (NLR), and nonlinear scattering (NLS) [93]. To elicit NLR, a wide range of physical factors which includes thermal lensing play a significant role while in optical phenomenon involving nanomaterials, nonlinear scattering principles apply. This study focuses on optical limiting processes associated with nonlinear absorption. NLA arises from reverse saturable absorption (RSA) exhibited by materials that show positive NLA absorption coefficients by inducing a reduction in transmittance as a function of high-intensity light. Amongst the combination of processes that can occur, two-photon absorption (2PA) and excited state absorption (ESA) predominate (**Figure 1.13**).

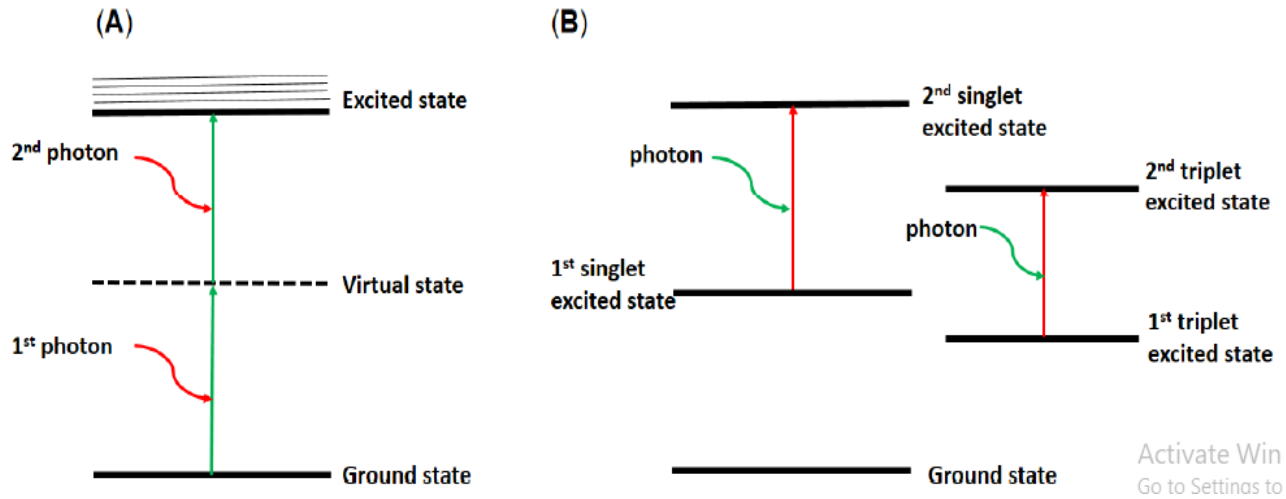

Figure 1.13. Jablonski diagram showing processes in two-photon absorption (A) and excited state absorption (B).

There is a higher probability of optical limiting materials to undergo 2PA before reverting to the ground state as the light intensity increases sufficiently, causing population redistribution [80]. This phenomenon manifests optically in a reduced (saturable) or increased (reverse saturable) absorption. Studies have shown that optical limiters exhibit RSA at wavelengths, where their excited state absorption cross-section becomes greater than ground state absorption cross-section [80]. 2PA is a resonant third-order nonlinear optical process that involves concurrent photon absorption by an excited state molecule when intensely focused light beam such as that generated by a laser pulse is used [81]. This phenomenon can be explained by the imaginary part of the third-order susceptibility (Im[$\chi^{(3)}$]), (**Figure 1.13**) [81]. It is possible for more than two photons to be involved, and this is referred to as multiphoton absorption [80,81]. Due to longer laser pulses used in this study (τ = 10 ns), quantification of 2PA which occurs on a femtosecond time scale is not possible, since ESA can also occur on the nanosecond timescale.

1.4.3.2. Optical Limiting parameters (z-scan technique)

Optical limiting parameters can be determined for NLA and NLR using the single-beam Z-scan experiment, which is a simple to operate and very sensitive technique (**Figure 1.14**) [79,82,83]. This is made possible by moving the sample along the z-direction of a focused Gaussian beam with a fixed set of laser pulses (**Figure 1.14**) [79,82,83]. Both closed and open aperture measurements can be made. During a closed aperture Z-scan experiment, the determination of both nonlinear absorptive and nonlinear refractive characteristics of an optical limiting material can be achieved.

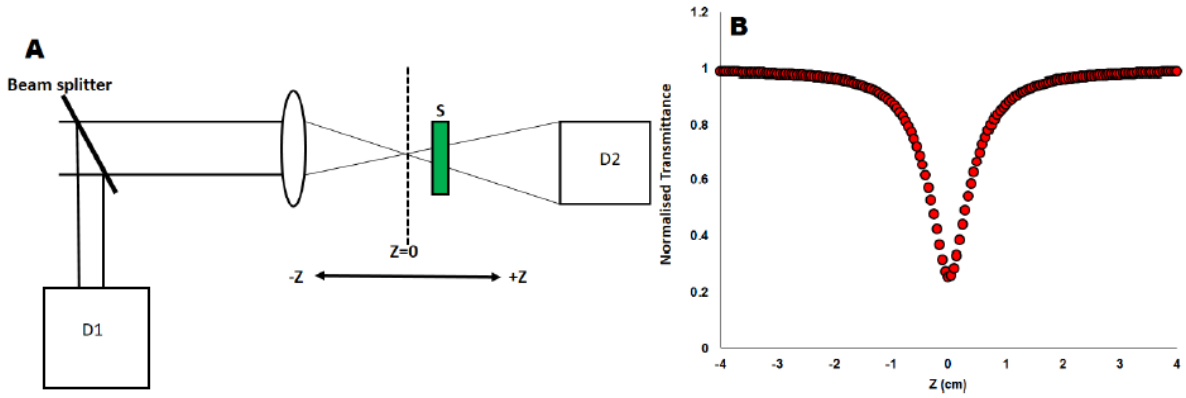

Figure 1.14. An open-aperture Z-scan experimental apparatus (A), showing the transmittance ratio D_2/D_1 as a function of the sample position. Typical reverse saturable absorption behaviour of an optical limiter obtained from the Z-scan setup (B).

In open aperture measurements, the energy transmitted is detected, and this gives rise to only NLA [83]. In this study, only the NLA properties of non-aggregated BODIPY dyes were considered, so an open aperture setup (**Figure 1.14**) was used in order to ascertain the main NLO parameters relevant to OL. In an open aperture Z-scan experiment, the normalised transmittance is the measured quantity, and can be analysed using a series of equations reported by Sheik-Bahae, **Equation 7** [94,95]:

$$T(z) = \frac{1}{\sqrt{\pi} q_0(z)} \int_{-\infty}^{\infty} \ln[1 + q_0(z)\, e^{-\tau^2}] d\tau \quad \textbf{(7)}$$

The parameter $q_0(z)$ provides the strength of the nonlinearity when a Gaussian shaped beam is used, and is described by **Equation 8** [94,95]:

$$q_0(z) = \frac{2\beta P_0 L_{eff}}{\pi w^2(z)} \quad \textbf{(8)}$$

where β denotes the nonlinear absorption coefficient, P_0 denotes the peak power of the laser pulses and the effective pathlength in the sample of length L is denoted by L_{eff}, given by **Equation 9**:

$$L_{eff} = \frac{1-e^{-\alpha L}}{\alpha} \quad (9)$$

where α represents the linear absorption coefficient (cm^{-1}). In practical applications of OL materials, measurement of α is at the intended wavelength, in this instance, 532 nm. The parameter (z) in **Equation 8** denotes the beam width as a function of the sample position as shown in **Equation 10** [94,95].

$$w(z) = w_0 \cdot \sqrt{1 + \left(\frac{z}{z_0}\right)^2} \quad (10)$$

At the focus (z = 0), w_0, describes the beam waist which is defined as the distance from the centre of the beam to the point where the intensity reduces to $1/e^2$ of its on-axis value; while z and z_0 shows the translational distance of the sample from the focus, and the Rayleigh length which is defined as $\pi w_0^2/\lambda$ where λ denotes the laser wavelength. The determination of the nonlinear absorption coefficient (β) from measured experimental normalised transmittance is accomplished with **Equations 7–10**. The measurement of the β value resulting solely from 2PA is not possible, since in this study a nanosecond pulsed laser is used, which elicits an RSA response associated with ESA (**Figure 1.14**). **Equation 7** is not appropriate to fit directly to the data. An analytical version of this formula [96] can be used to derive $q_0(z)$ directly from the normalised transmittance, and this is provided as **Equation 11**:

$$T(z) = 0.363e^{\left(\frac{-q_0(z)}{5.60}\right)} + 0.286e^{\left(\frac{-q_0(z)}{1.21}\right)} + 0.213e^{\left(\frac{-q_0(z)}{24.62}\right)} + 0.096e^{\left(\frac{-q_0(z)}{115.95}\right)} + 0.038e^{\left(\frac{-q_0(z)}{965.08}\right)} \quad \textbf{(11)}$$

To obtain $q_0(z)$, **Equation 10** is substituted into **Equation 8** as indicated below:

$$q_0(z) = \frac{Q_0}{1+\left(\frac{z}{z_0}\right)^2} \quad \textbf{(12)}$$

where,

$$Q_0 = \frac{2\beta P_0 L_{eff}}{\pi w^2(z)} = \frac{2\beta P_0 L_{eff}}{\lambda z_0} \quad \textbf{(13)}$$

From **Equation 11**, a Gaussian plot can be derived that shows Q_0 as the maximum value at the beam waist (z = 0). Using the plots peak value and FWHM, values for Q_0 and z_0 are obtained. Calculation of the nonlinear coefficient (β) can be carried out using **Equation 13** [94,95].

$$\beta = \frac{\lambda z_0 Q_0}{2P_0 L_{eff}} \quad \textbf{(14)}$$

The direct proportionality relationship between β and the imaginary component of the third order susceptibility, $Im[\chi^{(3)}]$ is shown in **Equation 15**:

$$Im\left[\chi^{(3)}\right] = \frac{\eta^2 \varepsilon_0 c \lambda \beta}{2\pi} \quad \textbf{(15)}$$

where, η represents the linear refractive index and c the speed of light in a medium, with ε_0 denoting permittivity of free space. The values obtained from third-order nonlinear optical susceptibility is useful for the description of ultrafast responses. The imaginary component provides a description of nonlinear absorption, while nonlinear refraction of the optical limiting material is represented by the real component [97]. Values of Im[$\chi^{(3)}$] in the 10^{-11}–10^{-13} esu range have been reported to be suitable for use in optical limiting [79,97]. The values for Im[$\chi^{(3)}$] give a description of the material response, while the material behaviour at the molecular level is described by its hyperpolarisability (γ), a parameter showing nonlinear absorption per mole of the optical limiting material (OL). This provides a useful parameter when comparing optical limiting efficiencies of various optical limiters, since concentration is taken into account. **Equation 16** shows the known correlation between Im[$\chi^{(3)}$] and γ:

$$\gamma = \frac{Im[\chi^{(3)}]}{f^4 C_{mol} N_A} \quad (\mathbf{16})$$

where N_A represents Avogadro's constant, the concentration of the active species per mole is denoted by C_{mol} and f is the Lorentz local field factor, $f = (\eta^2+2)/3$. Values of γ from 10^{-29} – 10^{-34} on the esu scale have been reported to be suitable for optical limiting [79,97].

The limiting intensity (I_{lim}) is derived from the definition of the threshold intensity as the fluence value where the linear transmittance is at 50% transmittance [90]. It is possible to experimentally determine approximate I_{lim} values by using a plot of output fluence (I_{out}) vs. input fluence (I_{in}). There are at the moment no known optimal values for I_{lim}, but ideally, lower I_{lim} values are an indication of the efficacy of a good optical limiter as this correlates with its limiting action which occurs at lower intensities and allows for greater protection of sensors. The International Commission On Non-Ionising Radiation Protection published guidelines

highlighting recommended limits of exposure for a variety of lasers [98]. In this work the second harmonic of an neodymium-doped yttrium aluminium garnet (Nd:YAG) laser at 532 nm with 10 ns laser pulses was employed, hence the limit of exposure can be determined from **Equation 17**:

$$2.7\ C_A t^{0.75}\ \mathrm{J/cm^2} \tag{17}$$

where C_A is a correction factor, which adds up to unity for lasers with wavelengths in the 400−700 nm range. For this work, the exposure limit was determined to be 0.95 J/cm^2 assuming a 0.25 s time of exposure, which was selected because it represents the average human response time (blink reflex) to a sudden flux of light into the eye [98].

Fluence, which is photons per unit area has units of W/cm^2, since 1 J/s = 1 W and the laser energy remains constant in any given z-scan experiment, so the overall power of the laser (J/s = W) remains unchanged. The maximum fluence found at the focus (z = 0). Maximum fluence can be determined by **Equation 18**.

$$I_{00} = \frac{E}{\tau \cdot \pi \cdot {w_0}^2} \tag{18}$$

In **Equation 18**, E is the maximum energy of the laser (J), τ denotes the duration of the laser pulse (s), and w_0 is the beam waist (cm). Due to the dependence of the beam width on the distance from the point of focus, fluence (W/cm^2) varies with z, and the circular cross-sectional area of the beam equals $(z)^2$. Hence multiplication of the laser fluence by the corresponding beam area derives the laser power, P, at the focus where z = 0, as represented by **Equation 19**.

$$P = I_{00} \cdot \pi w_0^2 \quad \textbf{(19)}$$

While at other *z* positions, *P* is denoted by **Equation 20**.

$$P = I_{in}(z) \cdot \pi w(z)^2 \quad \textbf{(20)}$$

Since the value of *P* does not change in any given z-scan run, scope exists for the combination of **Equations 19** and **20** as shown in **Equation 21**:

$$I_{in}(z) = I_{00} \cdot \left(\frac{w_0}{w(z)}\right)^2 \quad \textbf{(21)}$$

As the transmittance is directly proportional to the percentage of light that passes through a material, calculation of the output fluence ($I_{out}(z)$) can be achieved by finding first the product of $I_{in}(z)$ and the transmittance that corresponds to each *z* position ($T(z)$) as given by **Equation 22**.

$$I_{out}(z) = I_{in}(z) \cdot T(z) \quad \textbf{(22)}$$

In this study, a novel BODIPY dye was investigated for its efficacy as an OL material. The dye has an extended π-conjugation system due to substitution at the 3,5-positions with styryl groups and at the 2,6-positions with bromines. Bromines are heavy atoms that promote ISC to the triplet state from the singlet manifold through enhanced spin-orbit coupling. The structure of

the dye contains both electron-donating and -withdrawing functional groups separated by a π-system which encourages enhanced optical limiting response because of the dipole moment that is generated. Through the heavy atom effect of bromines, an increased population of the triplet state occurs, which can also lead to enhanced optical limiting behaviour through ESA, as has been reported for phthalocyanines [93]. It is expected that an interaction between the polarisable electrons of the BODIPY π-system with an oscillating electric field of light will cause a selective movement of the electrons from the donor to the acceptor moieties so that a single charge transfer direction is created [86], hence giving rise to a large second-order optical nonlinearity.

1.5 Aims

The aim of this work is to synthesise series of structurally modified BODIPY dyes with an overall goal of achieving red-shifted absorption in the 600−700 nm region and enhanced photophysical properties. The aims can thus be summarised as follows:

1. Synthesis and characterisation of halogenated BODIPY dyes.
2. Synthesis and characterisation of amine functionalised $CoFe_3O_4$ MNPs
3. Conjugation and characterisation of nanoparticles via amide bond linkage to BODIPY dyes.
4. Investigation of the photophysical behaviour of BODIPY dyes alone and when conjugated to MNPs.
5. Investigate applications in the photocatalytic degradation of organic dye pollutants and in PACT.
6. Study the non-linear optical behaviour of a selected 3,5-distyrylBODIPY dye.
7. Molecular modelling studies to ascertain structure-property relationships.

1.6 Publications to date

The following papers have already been published related to the work described in this thesis:

1) Lebechi, A. K.; Gai, L.; Shen, Z.; Nyokong, T.; Mack, J. Electrospun 3,5-dithienylvinyleneBODIPY embedded polystyrene nanofibers for the photocatalytic degradation of azo dyes in industrial wastewaters. *Journal of Porphyrins and Phthalocyanines* **2018**, 1-8.
2) Lebechi, A. K.; Nyokong, T.; Mack, J. BODIPY Dye Embedded Electrospun Polystyrene Nanofibers for the Photocatalytic Degradation of Orange G in Industrial Wastewaters. *Macroheterocycles* **2017**, *10*, 460-466

Chapter 2

2. EXPERIMENTAL

2.1. Materials

2.1.1. Reagents for BODIPY synthesis

Unless otherwise stated, there was no further purification of all reagents prior to use. Trifluoroacetic acid (TFA), 2,4-*dimethylpyrrole*, 1-pyrenecarboxaldehyde reagent plus (99%), 3-thiophenecarboxaldehyde, 9-anthracenecarboxaldehyde (97%), methyl-4-formyl benzoate, 4-bromobenzaldehyde, 4-nitrobenzaldehyde, 4-formyl benzoic acid, benzene, tetrachloro-1,4-benzoquinone (*p*-chloranil), triethylamine (TEA), boron *trifluoride* diethyl etherate ($BF_3.OEt_2$), sodium sulphide nonahydrate (98%), N-bromosuccinimide (NBS), anhydrous magnesium sulfate, glacial acetic acid, piperidine, polystyrene (PS), and sodium hydroxide pellets were purchased from Sigma-Aldrich. Hydrochloric acid 32% was purchased from Merck, and ammonium hydroxide was purchased from Saarchem.

2.1.2. Reagents for determining photophysical parameters

Diphenylisobenzofuran (DPBF), Rhodamine 6G, anthracene-9,10-bis-methylmalonate piperidine (ADMA) and ZnPc were purchased from Sigma Aldrich. Bengal Rose was purchased from Fluka.

2.1.3. Reagents for magnetic nanoparticle synthesis and linking to BODIPY dyes

Cobalt(II) chloride, Iron(III) chloride hexahydrate were purchased from Fluka. Tetraethyl orthosilicate (TEOS), (3-aminopropyl)triethoxysilane (APTES, 99%), (3-aminopropyl)trimethoxysilane (APTMS), succinic anhydride, N,N-dicyclohexylcarbodiimide (DCC) and oleic acid were purchased from Sigma-Aldrich.

2.1.4. Solvents

Ethanol, dimethylformamide (DMF), toluene, dimethylsulfoxide (DMSO), *n*-pentanol, *n*-hexanol, methanol, acetone, tetrahydrofuran (THF) and dichloromethane (DCM) were purchased from Saarchem. Ultra-pure water was prepared by using the Milli-Q Water system from Millipore Corp, Bedford, MA, USA. Dimethylformamide (DMF) was obtained from Associated Chemical Enterprises. Prior to use, all solvents were dried with molecular sieves.

2.1.5. Reagents for photocatalysis and PACT

Phosphate-buffered saline (PBS) solution (pH 6.8) was prepared with appropriate amounts of Na_2HPO_4 and NaOH in ultra-pure water from a Milli-Q Water system (Millipore Corp, Bedford, MA, USA). Nutrient agar and agar bacteriological BBL Muller Hinton broth were purchased from Merck. *Escherichia coli* (ATCC 25922) was obtained from Microbiologic, and *Staphylococcus aureus* (ATCC 25923) was purchased from Davies Diagnostics. Polystyrene (PS, MW = 192 000 g/mol), Methyl Orange (MO), and Orange G (OG) were purchased from Sigma-Aldrich

2.2. Instrumentation

1. Ground state UV-visible absorption spectra were measured on a Shimadzu UV-2550 spectrophotometer using a 1 cm pathlength quartz cuvette for studies in solution. A Perkin Elmer Lambda 950 Ultraviolet-visible spectrophotometer was used for solid state measurements.

2. ^{1}H-NMR spectra were recorded in deuterated solvents ($CDCl_3$ or THF-d_8) at room temperature on Bruker AMX 600 and 300 instruments operating at 600 and 300 MHz, respectively.

3. Fluorescence emission and excitation spectra were obtained using a Varian Cary Eclipse spectrofluorimeter. Optical densities of the solutions were consistently adjusted to ca. 0.05.

4. Monochromatic laser light (420–709 nm) from an Ekspla NT 342B-20-AW pulsed laser (2.0 mJ/5 ns, 20 Hz) was used to determine the singlet oxygen quantum yields.

5. Z-scan analyses were carried out with a frequency-doubled Nd:YAG laser (Quanta-Ray, 1.5 J/ 10 ns FWHM pulse duration). The laser was kept in a near Gaussian transverse mode, with 10 ns pulses at 532 nm and a repetition rate of 10 Hz and an energy range of 0.1 μJ–0.1 mJ, limited by the energy detectors (Coherent J5-09). The beam was filtered spatially to remove higher order modes and tightly focused with a 15 cm focal length lens.

6. No damage was detected between runs after the samples were moved or replaced. The Z-scan data in solution were obtained using a 2 mm quartz cuvette.

7. Elemental analyses for CHNS were carried out using a Vario-ElementarMicrocube ELIII Series.

8. Mass spectral data were collected with a Bruker AutoFLEX III Smartbeam TOF/TOF Mass spectrometer. The instrument was operated in positive ion mode using an m/z range of 400–3000 amu. The voltages of the ion sources were set at 19 and 16.7 kV for ion sources 1 and 2, respectively, while the lens was set at 8.50 kV and the reflector 1 and 2 voltages were set at 21 and 9.7 kV, respectively. α-Cyano-4-hydroxycinnamic

acid was used as the MALDI matrix with a 337 nm nitrogen laser selected as the ionising source.

9. Fourier transform-infrared spectra (FT-IR) were recorded on a Perkin Elmer Spectrum 100 FT-IR spectrometer.

10. Fluorescence lifetime values were measured using a time-correlated single photon counting (TCSPC) setup (FluoTime 200, Picoquant GmbH) (**Figure 2.1**). The excitation source was a diode laser (LDH-P-670 driven by PDL 800-B, 670 nm, 20 MHz repetition rate, 44 ps pulse width, Picoquant GmbH). Fluorescence was detected under the magic angle with a Peltier cooled photomultiplier tube (PMT) (PMA-C 192-N-M, Picoquant) and integrated electronics (PicoHarp 300E, Picoquant GmbH). A monochromator with a spectral width of 8 nm was used to select the required emission wavelength band. The response function of the system, which was measured with a scattering Ludox solution (DuPont), had a full width at half-maximum (FWHM) of about 300 ps. The ratio of stop to start pulses was kept low (below 0.05) to ensure good statistics. All luminescence decay curves were measured at the maximum of the emission peak. The data were analysed using the FluoFit program (Picoquant, GmbH).

11. X-ray photoelectron spectroscopy (XPS) analysis was measured using an AXIS UltraDLD (supplied by Kratos Analytical) with an Al (monochromatic) anode equipped with a charge neutralizer. The following parameters were used: the emission was 10 mA, the anode (HT) was set at 15 kV, and the operating pressure was kept below 5×10^{-9} torr. A hybrid lens was used, and the resolution to acquire scans was set at 160 eV pass energy in slot mode. The centre used for the scans was set at 520 eV (width of

1205 eV) with steps of 1 eV and a dwell time of 100 ms. the high-resolution scans were acquired using 80 eV pass energy in slot mode. The chemically distinct species were resolved using a nonlinear least-squares curve fitting procedure. The core level binding energies (BEs) were aligned with respect to the C_{1s} binding energy (BE) of 285 eV.

12. Transmission electron microscopy (TEM) images were obtained using a JEOL TEM 1210 transmission electron microscope at 100 kV accelerating voltage.

13. Scanning electron microscopy (SEM) images of the electrospun polymer nanofibres were obtained using a JOEL JSM 840 scanning electron microscope.

14. X-ray powder diffraction (XRD) patterns were recorded on a Bruker D8, Discover instrument equipped with a Lynx Eye Detector, using Cu Kα radiation (λ = 1.5405 A, Ni filter). Data were collected over the 2θ = 5−100° range, scanning at 1° min^{-1} with a filter time-constant of 2.5 s per step and a slit width of 6.0 mm. Samples were placed on a zero background silicon wafer slide. The X-ray diffraction data were retreated using Eva (evaluation curve fitting) software. A baseline correction was performed on each diffraction pattern by subtracting a spine fitted to the curved background and the full width at half maximum values reported in this study were obtained from the fitted curves.

15. The optical densities of the bacteria culture were determined using the Ledetect 96 from Labxim Products.

16. A Metrohm Swiss 827 pH meter was used for pH measurements

17. An RAU-530D autoclave was used for the sterilisation and autoclaving of nutrient broth, nutrient agar, and phosphate buffer as well as various apparatus for PACT studies.

18. A vortex mixer and Hermle Z233M-2 centrifuge from Lasiec were used to mix the bacteria suspension and for the harvesting of the bacteria cells, respectively.

19. A Scan® 500 automatic colour colony counter was used for the determination of the colony-forming units (CFU)/mL of bacteria.

20. Electrospun polymer nanofibres were obtained from a set-up consisting of a high voltage source (Glassman High Voltage. Inc., EL series, 0-40 kV), a pump (Kd Scientific, KDS-100-CE), and a plastic syringe connected to a steel needle with a 0.1 mm diameter and aluminium foil as a collector.

21. Photodegradation experiments for Methyl Orange and Orange G solutions and PACT experiments were conducted by using Thorlabs M660L4, M625L3 and M530L3 light-emitting diodes (LEDs) mounted into the housing of a Modulight 7710-680 medical laser system. Irradiance values were measured where necessary with a Coherent FieldmaxII TOP energy/power meter fitted with a Coherent Powermax PM10 sensor.

22. Theoretical calculations were carried out using the lengau cluster of the Centre for High Performance Computing in Cape Town.

2.3. Photophysical Methods

2.3.1. Fluorescence quantum yields (Φ_F)

Extensive studies have been undertaken on the fluorescence properties of BODIPY dyes and their associated applications [2,9,14]. As anticipated based on Kasha's rule, the fluorescence emission spectrum is a mirror image of the S_0−S_1 absorption band [42]. BODIPY core dyes have narrow absorption bands in the 500−550 nm range, and typically small Stokes shift values are observed due to the rigid geometries. The Stokes shift is the difference between the band maxima of the emitted and absorbed light associated with the $S_0 \rightarrow S_1$ and $S_1 \rightarrow S_0$ transitions [42]. Markedly red-shifted emission bands can be obtained upon structural modification of the BODIPY core. The fluorescence quantum yield (Φ_F) is the ratio of the number of photons emitted with respect to the number of absorbed photons. The comparative method (**Equation 2**) was used to determine the fluorescence quantum yield for BODIPY dyes and their nanoparticle conjugates [100-102]. Rhodamine 6G (Φ_F = 0.95 in EtOH [44,103]), and ZnPc (Φ_F = 0.20 in DMSO [104]) were used as standards. Excitation of both sample and standard was carried out at their cross-over wavelength, with maximum absorbance kept at ca. 0.05 to avoid inner filter effects.

2.3.2. Fluorescence lifetime (τ_F)

The fluorescence lifetime value is measured using the TCSPC method [105]. The time-dependent fluorescence intensity profile of emitted light is recorded upon excitation of the molecule by a pulsed laser [105]. The light intensity is kept very low; hence, the probability of detecting one photon in a single period is also very low. The time elapsed upon subsequent excitation by the pulsed laser and the detection of a fluorescence photon is determined and is known as the 'start-stop' time or the time delay (τ). With several repetitions, distribution of time differences can be acquired, with events being binned based on their respective time

differences [106,107]. Exponential curve fitting is used to obtain the τ_F value, which is the time it takes for the intensity to fall to 1/e of its initial value [107].

The use of very dilute solutions not only mitigates against fluorescence reabsorption by neighbouring molecules but is also necessary since the technique is based on single photon detection [107]. From a detection standpoint, there is a need to keep a low probability of registering more than one photon per cycle since the detectors and associated electronics possess a "dead" time [105-108], lasting a number of nanoseconds. Within this period, it is not possible to process another event, leading to an over-representation of early photons in the histogram, a phenomenon known as "pile-up" [108].

2.3.3. Singlet Oxygen Quantum Yield (Φ_Δ)

Singlet oxygen is a cytotoxic species that photodegrades/phototransforms organic pollutants as well as initiating apoptosis or cell death during PACT. In this regard, quantification of the singlet oxygen quantum yield (Φ_Δ) of a compound helps to determine its efficacy for use as a photosensitiser dye. The Φ_Δ value is defined as the number of singlet oxygen molecules produced for every absorbed photon (**Equation 23**). Typically, absorption of a single photon should generate a molecule of singlet oxygen. Therefore, the Φ_Δ value of a photosensitiser can be quantified through a relative method by comparison with a standard with a known Φ_Δ value [109,110].

$$\phi_\Delta = \frac{number\ of\ molecules\ of\ singlet\ oxygen\ formed}{number\ of\ photons\ absorbed} \quad \textbf{(23)}$$

A 1 cm path-length spectrophotometric cell was used for the singlet oxygen quantum yield studies of BODIPY dyes. The rate of singlet oxygen photogeneration was measured in solution

in an oxygenated environment with ZnPc, or Rose Bengal used as a reference compound and DPBF acting as the singlet oxygen scavenger [111]. Solutions of the sample and standards containing identical aliquots of DPBF solution were irradiated in the dark. Irradiations were carried out at a wavelength at which absorbances of the sample and standard solutions are equal, referred to as the cross-over wavelength. The changes in the concentration of DPBF were monitored spectroscopically with each subsequent irradiation [111]. The values of Φ_Δ were calculated using **Equation 3** [110,111]. During the study, the initial concentration of DPBF was kept constant in the sample and reference solutions. ZnPc (Φ_Δ = 0.67 in DMSO [112]; Φ_Δ = 0.53 in EtOH [112]; Φ_Δ = 0.56 in DMF [112]) and Rose Bengal (Φ_Δ = 0.76 in DMSO [112]; Φ_Δ = 0.86 in EtOH [112,113]) were used as standards.

2.4. Synthesis

The synthesis of BODIPY core dyes was based on a previously reported [2] one-pot procedure, following a Lewis acid-catalysed condensation of aldehydes and 2, 4-dimethylpyrrole. Although the reaction follows a step-wise process, only the final product is isolated, purified and characterised.

2.4.1. BODIPY core dyes

Benzaldehyde (1 eq) and 2, 4-dimethylpyrrole were dissolved in dry DCM (50 ml) under inert conditions (example argon or nitrogen gas). TFA (3 ml) was added, and the mixture left to stir continuously at room temperature. Thin-layer chromatography (TLC) was used to monitor the complete consumption of the aldehyde and the formation of the appropriate dipyrromethane. A solution of *p*-chloranil (1.2 eq) dissolved in DCM (10 ml) was added to the stirring reaction mixture at 0^oC. The solution was then allowed to warm up to room temperature, and the reaction was left to continue stirring for 30 min under Ar/N_2. A deep purple colour was observed. The synthesis of dipyrromethene was confirmed by using TLC, after which the

reaction mixture was cooled again to 0ºC. TEA (7 eq) and $BF_3 \cdot Et_2O$ (11 eq) were added dropwise, and subsequently, the reaction was left to stir at room temperature for 12 h. The resulting mixture was washed with water, dried over anhydrous sodium sulfate, and the organic residue was purified by column chromatography by eluting with ethyl acetate: petroleum ether (1:4).

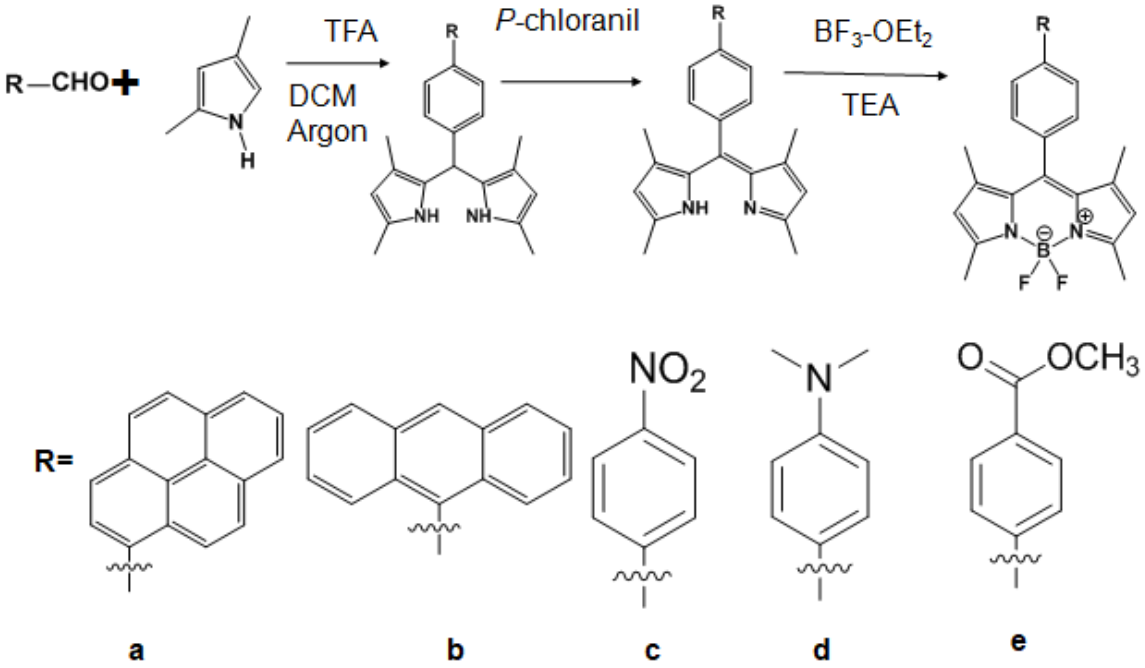

Scheme 6. Synthesis of BODIPYs **1a-e**.

BODIPY **1a**, 4,4′-difluoro(8-pyrenyl)-1,3,5,7-tetramethyl-4-bora-3a,4a-diaza-*s*-indacene, was obtained in 65% yield (0.63 g); IR (ν_{max}/cm^{-1}): 2951−2816 (Aliph CH), 1360−1060 (Ar C-N), 416 (C-H); ^{1}H NMR (600 MHz; THF-d_8): δ 8.40−8.37 (1H, m, Ar-H), 8.30−8.25 (2H, m, Ar-H), 8.22-8.20 (2H, m, Ar-H), 8.07−8.06 (1H, m, Ar-H), 8.00−7.97 (1H, m, Ar-H), 5.99 (2H, s, C-H), 2.56 (6H, s, CH_3), 0.90 (6H, s, CH_3) ppm.

BODIPY **1b**, 4,4′-difluoro(8-anthracyl)-1,3,5,7-tetramethyl-4-bora-3a,4a-diaza-*s*-indacene, was obtained in 62% yield (0.61 g); IR (ν_{max}/cm^{-1}): 2917−2853 (Aliph CH), 1499−1070 (Ar C-N), 467 (C-H); ^{1}H NMR (600 MHz, $CDCl_3$) δ 8.60 (s, 1H, Ar-H), 8.06 (d, *J* = 8.4 Hz, 2H, Ar-H), 7.94 (d, *J* = 8.7 Hz, 2H, Ar-H), 7.53−7.50 (m, 2H, Ar-H), 7.48−7.43 (m, 2H, Ar-H), 5.92 (s, 2H, C-H), 2.65 (s, 6H, CH_3), 0.67 (s, 6H, CH_3) ppm.

BODIPY **1c**, 4,4′-difluoro(8-nitrophenyl)-1,3,5,7-tetramethyl-4-bora-3a,4a-diaza-*s*-indacene, was obtained in 42% yield (0.65 g); IR (ν_{max}/cm^{-1}): 2917−2852 (Aliph CH), 1408−1075 (Ar C-N), 468 (C-H); ^{1}H NMR (600 MHz; $CDCl_3$): δ 8.34 (d, *J* = 12 Hz, 2H, Ar-H), 7.51 (d, *J* = 12 Hz, 2H, Ar-H), 6.01 (s, 2H, C-H), 2.53 (s, 6H, CH_3), 1.33 (s, 6H, CH_3) ppm.

BODIPY **1d**, 4,4′-difluoro-8-(4-dimethylaminophenyl)-1,3,5,7-tetramethyl-4-bora-3a,4a-diaza-*s*-indacene, was obtained in 57% yield (0.43 g); IR (ν_{max}/cm^{-1}): 2911−2853 (Aliph CH), 1456−1049 (Ar C-N), 468 (C-H); ^{1}H NMR (600 MHz; $CDCl_3$): δ 7.01 (s, 2H, Ar-H), 6.73 (s, 2H, Ar-H), 5.91 (s, 2H, C-H), 2.96 (s, 6H, CH_3), 2.49 (s, 6H, CH_3), 1.43 (s, 6H, CH_3) ppm.

BODIPY **1e,** 4,4′-difluoro-8-(4-carboxymethylphenyl)-1,3,5,7-tetramethyl-4-bora-3a,4a-diaza-*s*-indacene was obtained in 51% yield (0.38 g); IR (ν_{max}/cm^{-1}): 2920−2851 (Aliph CH), 1401−1190 (Ar C-N), 509 (C-H); ^{1}H NMR (600 MHz, $CDCl_3$): δ 8.20 (s, 2H, Ar-H), 7.42 (s, 2H, Ar-H), 6.01 (s, 2H, C-H), 4.00 (s, 3H, CH_3), 2.58 (s, 6H, CH_3), 1.38 (s, 6H, CH_3) ppm.

2.4.2. Brominated BODIPYs.

Brominated BODIPYs **2a-d** (**Scheme 7**) were prepared following a modified version of a previously reported procedure [11]. To a solution of BODIPYs **1a-d** (1 eq) dissolved in DCM

(20 mL), were added NBS (3 eq) dissolved in DCM. The mixture was left to stir under Ar/N_2 at room temperature; the reaction was monitored by thin-layer chromatography to completion. The product was washed with water, and the organic phase dried over sodium sulfate. Purification was achieved via column chromatography with ethyl acetate:petroleum ether (1:4) as eluent.

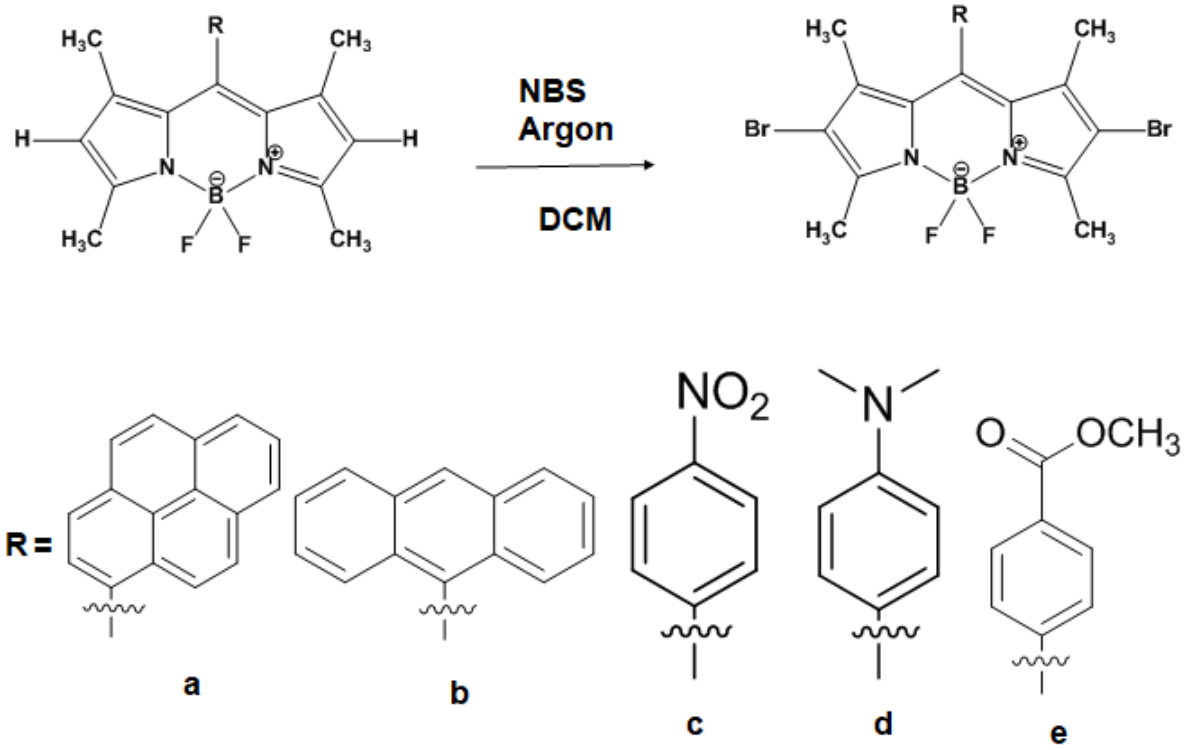

Scheme 7. Bromination procedure to obtain BODIPYs **2a-e**.

BODIPY **2a**, 4,4′-difluoro(8-pyrenyl)-1,3,5,7-tetramethyl-2,6-dibromo-4-bora-3a,4a-diaza-*s*-indacene, was obtained in 89% yield (0.69 g); FT-IR (ν_{max}/cm^{-1}): 524 (C-Br); ^{1}H NMR (600 MHz, $CDCl_3$): δ ^{1}H NMR (600 MHz, $CDCl_3$) δ 8.33 (s, 2H, Ar-H), 8.25 (s, 2H, Ar-H), 8.19 (s, 1H, Ar-H), 8.11 (s, 2H, Ar-H), 7.97 (s, 1H, Ar-H), 7.88 (s, 1H, Ar-H), 2.70 (s, 6H, CH_3), 1.59 (s, 6H, CH_3). ppm; MALDI-TOF Anal. Calc. m/z 606.01; Found: $[M]^+$ 605.5.

BODIPY **2b**, 4,4′-difluoro(8-anthracyl)-1,3,5,7-tetramethyl-2,6-dibromo-4-bora-3a,4a-diaza-*s*-indacene, was obtained in 85.4% yield (0.68 g); FT-IR (ν_{max}/cm^{-1}): 521 (C-Br); ^{1}H NMR

(600 MHz, THF-d_8) δ 8.68–8.64 (m, 3H, Ar-H), 7.89 (d, J = 8.7 Hz, 2H, Ar-H), 7.73–7.69 (m, 2H, Ar-H), 7.56 (d, J = 5.5 Hz, 1H, Ar-H), 7.43 (s, 1H, Ar-H), 2.64 (s, 6H, CH_3), 0.64 (s, 6H, CH_3) ppm. MALDI-TOF Anal. Calc. m/z 582.01; Found: $[M^+H]^+$ 583.01.

BODIPY **2c**, 4,4′-difluoro-8-(4-nitrophenyl)-1,3,5,7-tetramethyl-2,6-dibromo-4-bora-3a,4a-diaza-*s*-indacene, was obtained in 86.6% yield (0.68 g); FT-IR (ν_{max}/cm^{-1}): 523 (C-Br); ^{1}H NMR (300 MHz, $CDCl_3$) δ 8.57 (d, J = 8.7 Hz, 2H, Ar-H), 7.67 (d, J = 8.7 Hz, 2H, Ar-H), 2.76 (s, 6H, CH_3), 1.50 (s, 6H, CH_3) ppm. MALDI-TOF Anal. Calc. m/z 526.97; Found: $[M^+]$ 526.20

BODIPY **2d**, 4,4′-difluoro-8-(4-dimethylaminophenyl)-1,3,5,7-tetramethyl-2,6-dibromo-4-bora-3a,4a-diaza-*s*-indacene, was obtained in 72% yield (0.82 g); FT-IR (ν_{max}/cm^{-1}): 522 (C-Br); ^{1}H NMR (600 MHz, $CDCl_3$) δ 8.47 (s, 2H, Ar-H), 7.82 (s, 2H, Ar-H), 3.39 (s, 6H, CH_3), 1.37 (s, 6H, CH_3), 1.24 (s, 6H, CH_3) ppm. MALDI-TOF Anal. Calc. m/z 525.02; Found: $[M^+H]^+$ 526.08.

BODIPY **2e**, 4,4′-difluoro-8-(4-carboxymethylphenyl)-1,3,5,7-tetramethyl-2,6-dibromo-4-bora-3a,4a-diaza-*s*-indacene, was obtained in 74.3% yield (0.58 g); FT-IR (ν_{max}/cm^{-1}): 521 (C-Br); ^{1}H NMR (600 MHz, $CDCl_3$) δ 8.26 (s, 2H, Ar-H), 7.42 (d, J = 7.2 Hz, 2H, Ar-H), 4.02 (s, 3H, CH_3), 1.27 (s, 6H, CH_3), 0.89 (m, 6H, CH_3) ppm. MALDI-TOF Anal. Calc. m/z 539.54; Found: $[M]^+$ 540.0.

2.4.3. Synthesis of styryl and vinylene extended BODIPYs

BODIPY 3: 4,4′-Difluoro(8-pyrenyl)-1,7-dimethyl-2,6-dibromo-3,5-(di-4-carboxystyryl)-4-bora-3a,4a-diaza-*s*-indacene

BODIPY **2a** (1 eq), 4-formylbenzoic acid (1.4 eq) and glacial acetic acid (0.4 mL) were dissolved in dry benzene (20 mL) under argon with stirring (**Scheme 8**). Piperidine (0.4 mL) was added slowly, and the solution was heated to reflux for 2 h under argon. A Dean-Stark trap was employed for the azeotropic removal of water formed during the condensation reaction. The reaction was quenched with a 1 molar solution of water, and the organic phase was dried over sodium sulfate. The mixture was separated by flash column chromatography with methanol: chloroform (2:3). BODIPY **3** was obtained in 21.1% yield (0.05 g); IR (ν_{max}/cm^{-1}): 3154 (OH), 2850 (Aliph CH), 1683 (C=O), 1604−1520 (C=C), 1435−1060 (Ar C-N), 516 (C-Br); ^{1}H NMR (600 MHz, DMSO-d_6) δ 13.02 (s, 2H, COOH), 8.67 (s, 4H, Ar-H), 8.38 (s, 2H, Ar-H), 8.13 (d, J = 8.2 Hz, 2H, Ar-H), 8.05-7.99 (m, 4H, Ar−H), 7.97−7.90 (m, 4H, Ar-H), 7.81 (d, J = 8.0 Hz, 2H, Ar-H), 7.48−7.52 (m, 3H), 3.25 (s, 6H, CH_3) ppm. MALDI-TOF Anal. Calc. m/z 870.34; Found: $[M]^+$ 870.66.

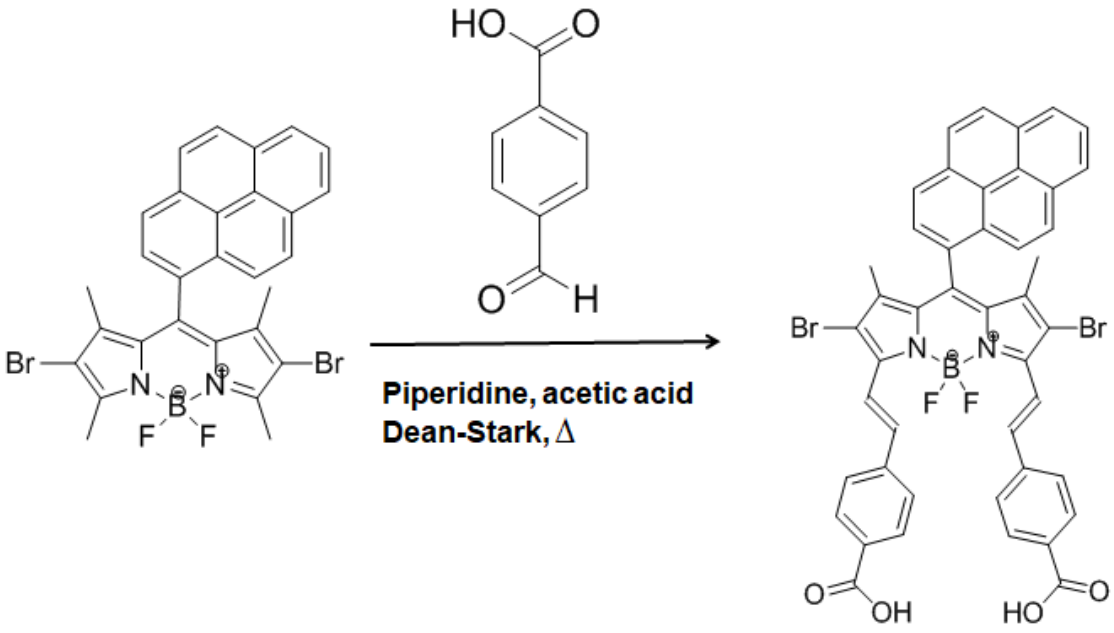

Scheme 8. Synthesis of BODIPY **3**.

BODIPY 4, 4,4′-difluoro-8-phenyl-1,7-dimethyl-2,6-diiodo-3,5-di(thiophen-2-yl)vinyl-4-bora-3a,4a-diaza-*s*-indacene (**Figure 2.1**), was synthesised and purified by Dr Lizhi Gai of Nanjing University and its characterization has been reported previously [90].

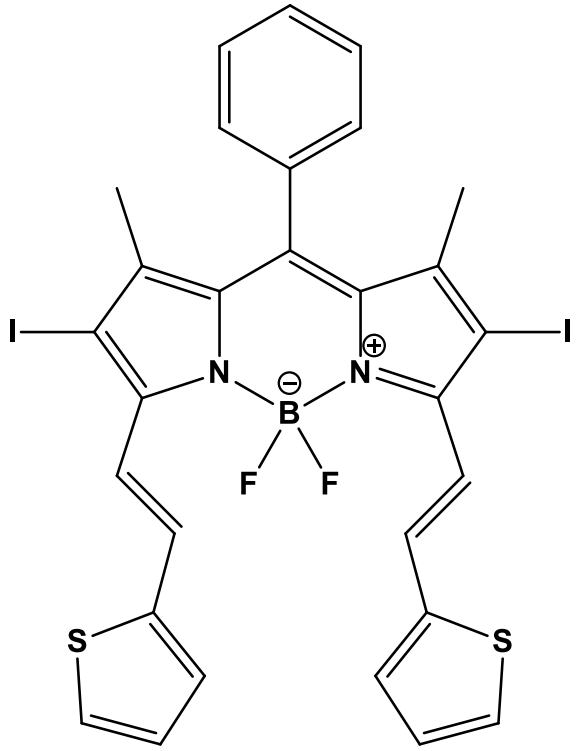

Figure 2.1. Structure of BODIPY **4**.

BODIPY 5: 4,4′-Difluoro(8-anthracyl)-1,7-dimethyl-2,6-dibromo-3,5-(di-4-phenylcarboxystyryl)-4-bora-3a,4a-diaza-*s*-indacene

BODIPY **2b** (1 eq), 4-formylbenzoic acid (1.4 eq) and glacial acetic acid (0.4 mL) were dissolved in dry benzene (20 mL) under argon with stirring (**Scheme 9**). Piperidine (0.4 mL) was added slowly and the solution heated to reflux for 2 h under argon (inert gas). The azeotropic removal of water formed during the condensation reaction was achieved using the Dean-Stack trap apparatus. The reaction was quenched with 1 molar solution of water and hydrochloric acid, and the organic phase was dried over sodium sulfate. The mixture was separated by flash column chromatography with ethyl methanol: chloroform (2:3). BODIPY **5** was obtained in 19.5% yield (0.03 g); FT-IR (cm^{-1}): 3132 (OH), 2845 (C-H stretch), 1666

(C=O), 1257 (C-O), 1401, 1359 (C-N stretch), 1095 (C-N stretch), 1163, 982 (=C-H bend), 564,520 (C-Br stretch); ^{1}H NMR (600 MHz, THF-d_8) δ 8.21 (s, 2H), 6.32 (d, J = 8.1 Hz, 4H), 6.28–6.21 (m, 4H), 6.12 (s, 4H), 6.06 (d, J = 9.1 Hz, 3H), 5.96 (s, 2H), 4.73 (s, 2H), 4.64 (s, 2H), 0.65–0.64 (m, 6H) ppm. MALDI-TOF Anal. Calc. m/z 846.36; Found: $[M]^+$ 846.88.

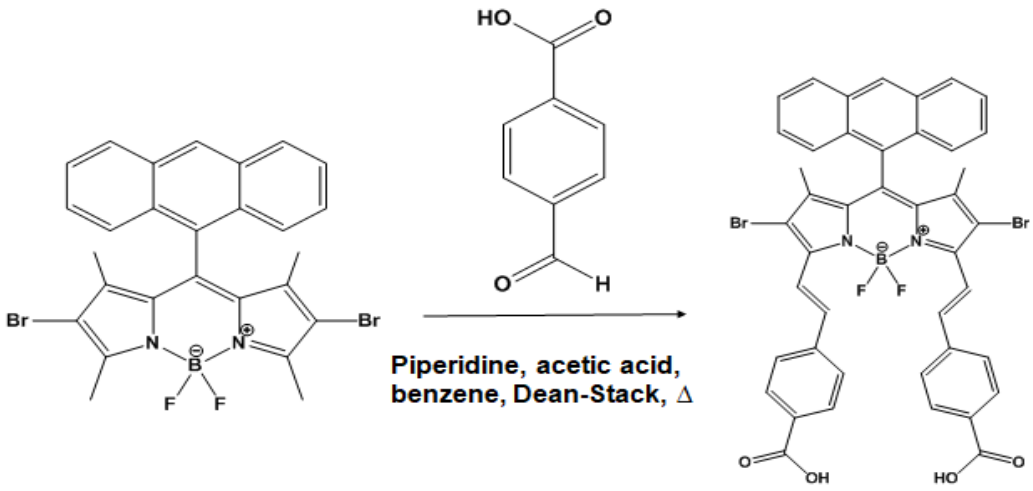

Scheme 9. Synthesis of BODIPY **5**.

2.4.4. Synthesis of magnetic nanoparticles and conjugates

2.4.4.1. Oleic acid coated $CoFe_2O_4$ MNPs

Synthesis of cobalt-ferrite magnetic nanoparticles followed a previously reported conventional coprecipitation method [49] with slight modifications. Iron (III) chloride hexahydrate (25 mL, 0.4 M) and cobalt (II) chloride (25 mL, 0.2 M) solutions were stirred, and this was followed by dropwise addition of sodium hydroxide (25 mL, 3 M) to the salt solution until a pH of 11–12 was attained. Oleic acid (2 mL) as a surfactant was slowly added dropwise, and the solution was then heated to a temperature of 80°C with stirring for 1 h. The resultant precipitate was washed twice with deionised water and then with ethanol to remove excess oleic acid. The

precipitate was dried overnight under vacuum to remove ethanol, and the oleic acid capped $CoFe_2O_4$MNPs were then stored by redispersing in deionised water.

2.4.4.2. Silica-coated magnetic nanoparticles ($CoFe_2O_4$–SiO_2 MNPs)

The bare $CoFe_2O_4$ MNPs were encapsulated with silica for easy functionalisation, as previously reported [50]. Ethanol (80 mL), TEOS (169 µL) and APTMS (14.4 µL) were mixed in a beaker, and 20 mL of the oleic acid capped $CoFe_2O_4$ MNPs were subsequently added dropwise to the mixture followed by stirring for 3 h at room temperature. The silica-coated cobalt ferrite nanoparticles ($CoFe_2O_4$-SiO_2) were collected with a magnet, washed three times with deionised water and then dried overnight under vacuum.

2.4.4.3. Amine functionalised $CoFe_2O_4$ magnetic nanoparticles ($CoFe_2O_4$-NH_2 MNPs).

The silica-coated $CoFe_2O_4$ nanoparticles were modified with amine groups using APTES [50] as follows: the silica-coated MNPs (600 mg), DMF (12 mL) and toluene (8 mL) were vortexed in a 50 mL tube, and while stirring 200 µL APTES was added dropwise into the mixture. The mixture was finally left stirring for 24 h after which the functionalised particles ($CoFe_2O_4$-NH_2 MNPs) were collected with a magnet and washed with toluene, and dried overnight under vacuum.

2.4.4.4. Functionalisation of the magnetic nanoparticles with carboxylic acid ($CoFe_2O_4$−COOH MNPs)

Addition of carboxyl groups to the amine-functionalised $CoFe_2O_4$ nanoparticles was achieved by a ring-opening linker elongation reaction [50]. The ring structure of succinic anhydride was opened up and reacted with the amine groups as follows: 10 mL of a homogenous colloid suspension of the amine-functionalised $CoFe_2O_4$ was added dropwise to a 10 mL DMF solution containing 0.1 g (1.0 mmol) succinic anhydride, and the mixture was stirred for 24 h at room

temperature. The modified nanoparticles were washed with DMF and ethanol, dried under vacuum overnight.

2.4.4.5. Conjugation of BODIPYs to $CoFe_2O_4$ MNPs

Prior to conjugation, activation of the carboxylic acid functional groups on the BODIPY dye was achieved by adding the appropriate BODIPY (0.1 g) and DCC (1.3 g, 6.25mmol) in 5 mL DMSO and stirring for 12 h. $CoFe_2O_4NH_2$-MNPs (0.15 g) was then added to the mixture followed by stirring for 48 h. The final product was washed three times with ethanol and finally with toluene and dried under vacuum.

A mixture of $CoFe_2O_4$-COOH (0.10 g) and DCC (0.02 g, 0.097mmol) was stirred in DMF (4 mL) at room temperature for 48 h to activate the carboxylic acid terminal groups of $CoFe_2O_4COOH$. The appropriate BODIPY (0.1 g) was then dissolved in DMF (2 mL) and added slowly to the above mixture, followed by stirring for a further 48 h. The product was collected and washed several times by centrifugation in acetone, methanol, and absolute ethanol in succession to remove excess DCC.

2.5 Electrospinning methods

Polystyrene (PS) crystals were dissolved in a THF:DMF (2:8) mixture and stirred for 12 h at room temperature. The electrospun unfunctionalised PS fibres were prepared by placing the solution in a 20 mL syringe fitted with a hypodermic needle (inner diameter of 0.1 mm). Electrospinning was then conducted under the following parameters: flow rate 0.05 mL/h, voltage 20 kV, tip to collector distance (TCD) 12 cm, room temperature and 48% relative humidity. The same parameters were maintained for the BODIPY/PS solutions.

2.6. Antimicrobial studies

Staphylococcus aureus and *Escherichia coli* were grown on agar plates by following the manufacturer's specifications to obtain an individual colony. The colony was inoculated into

the nutrient broth and agitated on a rotary shaker (ca. 200 rpm) overnight at 37°C (*Escherichia coli* and *Staphylococcus aureus*). Aliquots of the culture were transferred to 6 ml of fresh broth and incubated at 37°C to obtain a mid-logarithmic phase (OD 620 nm ≈ 0.6). Through centrifuging for 15 min at 3000 rpm to remove the broth, the bacterial culture in the logarithmic phase of growth was harvested and washed three times in PBS. The bacteria culture was diluted to 1/1000 in PBS to provide a working stock solution.

Photodynamic antimicrobial activities of the bacteria were performed following previously reported methods [66]. In all the experiments, suspensions of the bacteria were incubated in an oven equipped with a shaker for 30 min in the dark at 37°C. Then, half (3 mL) of the incubated bacterial suspensions were irradiated at the absorption band maxima of the photosensitiser dye in a 24 well plate, using the set-up described above and the other half was kept in the dark. After irradiation, 100 μL samples were inoculated, and the plates incubated at 37°C. All the experiments were carried out in triplicates.

2.7. Photo-degradation studies

Prior to photocatalytic experiments, the fibres were immersed in both Orange G and Methyl Orange solutions for 30 min to eliminate adsorption effects. The photodegradation of Methyl Orange and Orange G were monitored by viewing the spectral changes at 5 min intervals by UV-visible absorption spectroscopy.

Chapter 3

3. SYNTHESIS AND SPECTROSCOPIC CHARACTERISATION OF BODIPY DYES AND CONJUGATES

In this chapter, the synthesis and characterisation of a series of 1,3,5,7-tetramethylBODIPY core dyes and their 2,6-dibrominated analogues are described, along with that of π-extended 3,5-distyryl analogues of some of the dibrominated cores. The synthesis of the BODIPY core dyes **1a-e** (**Scheme 1**) was carried out to prepare precursors for further reaction. The synthesis of BODIPYs **2a-e** (**Scheme 2**) involves the addition of bromines at the 2,6-positions of BODIPYs **1a-e**. BODIPYs **2a-b** were used as starting reagents for π-extended BODIPYs **3-5**, which are used as optical limiting materials, for the photocatalytic degradation of organic pollutants and in PACT. The photophysical and photochemical properties of **2a-e** and **3-5** were determined to identify trends in their singlet oxygen generating proficiencies.

3.1. 8-Pyrenyl-1,3,5,7-tetramethylBODIPY 1a

BODIPY **1a** has had previously been reported [114] and was synthesised as a precursor for BODIPY dyes suitable for use in optical limiting, photocatalytic degradation of organic pollutants and in PACT. The synthetic route follows the conventional TFA-catalysed ‘’one-pot three-step’’ condensation of 2, 4-dimethylpyrrole and 1-pyrenecaroxaldehyde in DCM (**Scheme 10**).

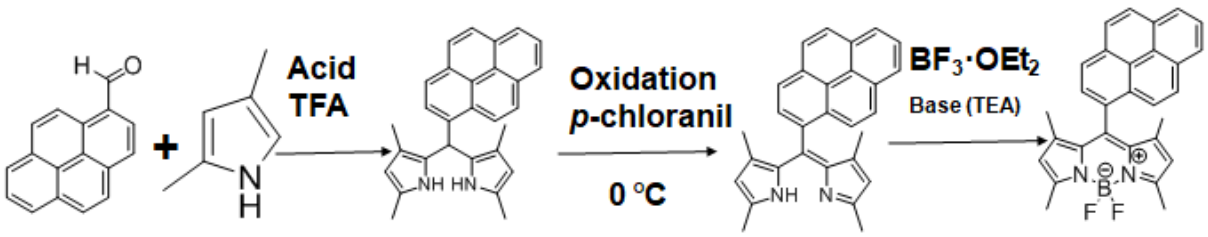

Scheme 10. The acid-catalysed synthesis of BODIPY **1a** following the classical one-pot procedure.

3.1.2 Characterisation of BODIPY 1a

The signals from the twenty-three protons of BODIPY **1a** can readily be identified from the ^{1}H NMR spectrum (**Figure 3.1**). The multiplets that lie at 7.97−8.40 ppm integrate to 9 protons and can be attributed to the pyrene ring, while the singlet at 5.99 ppm integrates to two protons and can be assigned to the 2,6-position protons of **1a.** The signals at 0.90 and 2.56 ppm can be attributed to the twelve methyl protons on the pyrrole core. The signals at 1.73 and 3.58 ppm respectively belong to the deuterated THF solvent. In the FT-IR spectrum (**Figure 3.2**), the peaks normally expected for a BODIPY core dye are observed [115,116]. Bands that lie between 2851−2916 cm^{-1}are attributed to the C-H stretch of the terminal methyl groups, while N-C stretch bands associated with the pyrrolic nitrogen atoms lie between 1060−1360 cm^{-1}. A peak at 466 cm^{-1} can be assigned to C-H stretches at the 2,6-positions of the BODIPY core.

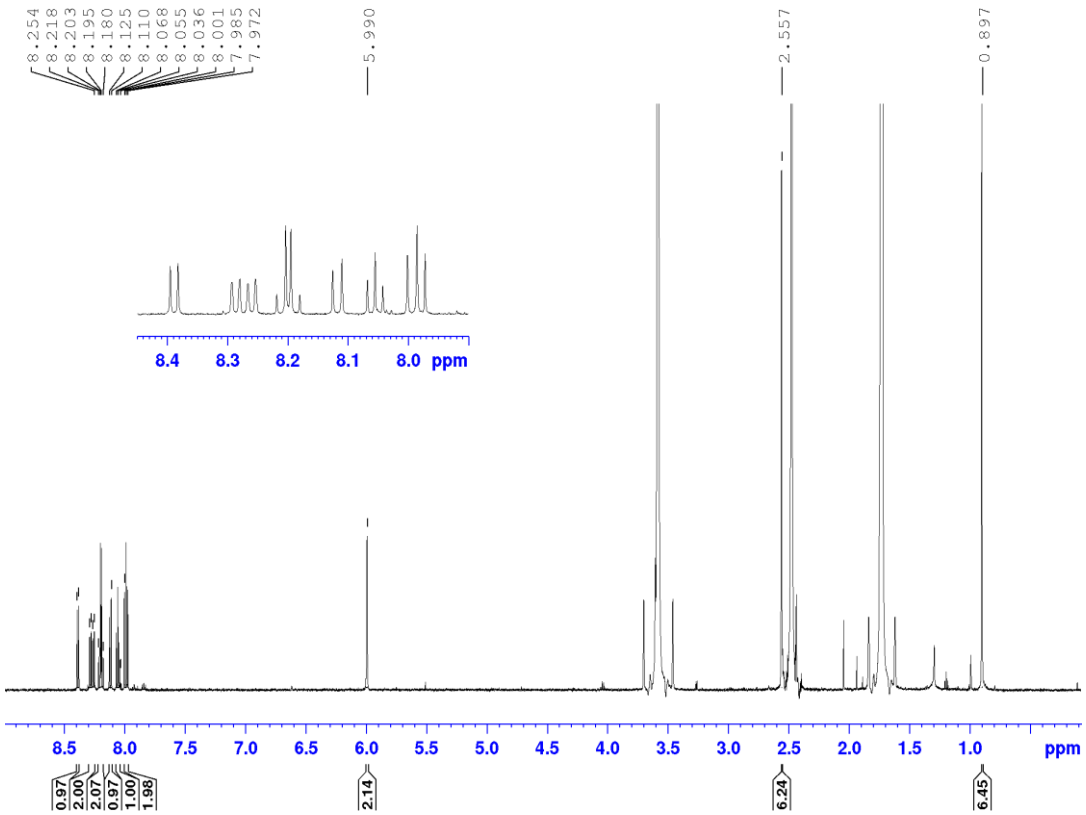

Figure 3.1. ^{1}H NMR spectrum of BODIPY **1a** in THF-d_8.

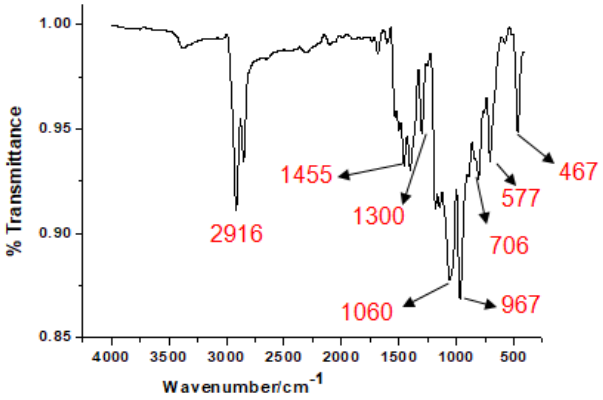

Figure 3.2. The FT-IR spectrum of BODIPY **1a**, highlighting peaks that can be attributed to the BODIPY core.

3.1.3. Spectroscopic properties of BODIPY 1a

BODIPY **1a** exhibits a typical *meso*-substituted BODIPY absorption spectrum with a band maximum at 506 nm in DMSO (**Figure 3.3**), similar to what has been reported previously [2,14]. There is no evidence of band broadening due to aggregation. The absorption, excitation and emission band maxima are summarised in **Table 1**. The emission spectrum is typical for a 1,3,5,7-tetramethyl BODIPY core [14]. The fluorescence quantum yield determination gave a value of 0.14 in DMSO. A singlet oxygen quantum yield value of 0.05 was obtained. In the course of irradiations, the main absorption band did not show any significant decrease, an indication of good photostability. The log ε value obtained for BODIPY **1a** is 4.84 in DMSO.

Table 1. Photophysical and photochemical data for BODIPY **1a**.

	λ_{Abs} (nm)	λ_{exc} (nm)	λ_{em} (nm)	Stokes shift (cm^{-1})	Φ_F	log ε	Φ_Δ
DMSO	506	502	512	231	0.14	4.84	---
EtOH	503	501	507	156	0.53	---	---
THF	503	501	508	195	0.24	---	0.05

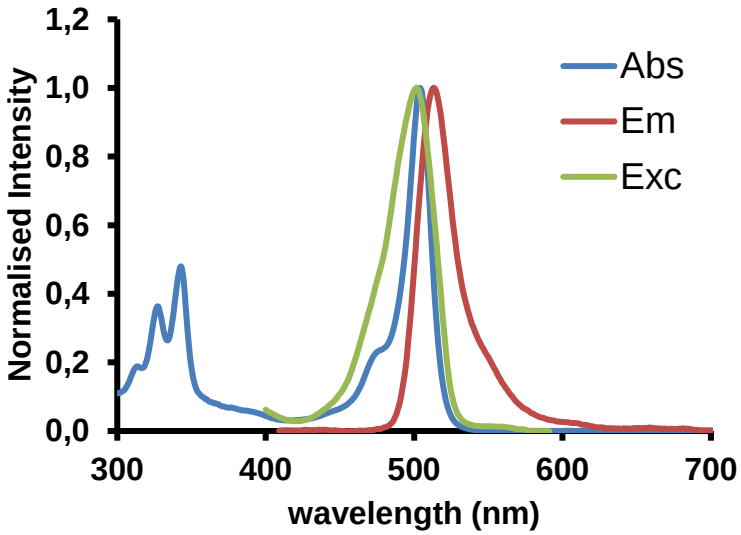

Figure 3.3. Normalised absorption (*blue*), excitation (*green*) and emission (*purple*) spectra of BODIPY **1a** in DMSO.

3.2. 8-Anthracyl-1,3,5,7-tetramethylBODIPY 1b.

3.2.1 Synthesis of BODIPY 1b

BODIPY **1b** has been reported previously [117] and was synthesised as a precursor for more complex analogues that are suitable for use in PACT. The synthesis route is analogous to that of BODIPY **1a** (**Scheme 11**).

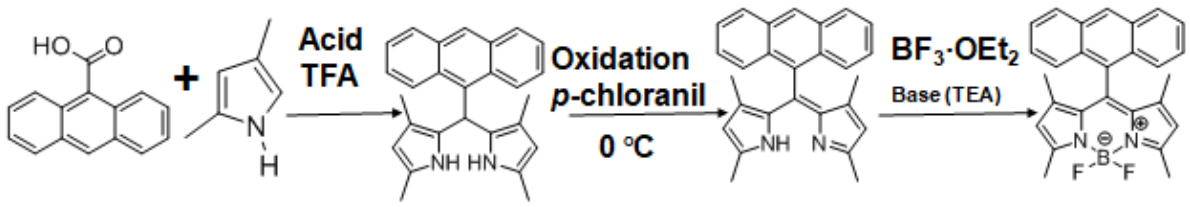

Scheme 11. One-pot acid-catalysed synthesis of BODIPY **1b**.

3.2.2 Characterisation of BODIPY 1b

On the ^{1}H proton NMR spectrum can be readily identified the signals for the twenty-three protons**.** The nine protons of the anthracene ring in the aromatic region integrate into the

following peaks that lie between 7.4−8.6 ppm. Two sets of signals that lie between 7.43−7.53 and 7.90-8.10 ppm integrate to four protons each, and a singlet peak that lies at 8.60 ppm integrates into one proton. A singlet at 5.92 ppm integrates to two protons and can be assigned to the 2,6-positions of the BODIPY core. The twelve protons at 0.67 and 2.65 ppm can be attributed to the twelve protons from the methyl group of the pyrrole core. In the FT-IR spectrum, the peaks normally expected for a BODIPY core dye are observed [115,116]. Bands that lie between 2853−2917 cm^{-1} are attributed to the C-H stretch of the terminal methyl groups, while N-C stretch bands associated with the pyrrolic nitrogen atoms lay between 1070−1499 cm^{-1}. A peak at 467 cm^{-1} can be assigned to C-H stretches at the 2,6-positions of the BODIPY core. The peaks expected for a BODIPY core were observed on the FT-IR.

3.2.3 Spectroscopic properties of BODIPY 1b

BODIPY **1b** exhibits a typical *meso*-substituted BODIPY absorption spectrum with a band maximum at 505 nm in DMSO (**Figure 3.4**). The dye exhibits good solubility in a range of organic solvents, and there is no evidence of band broadening due to aggregation. The absorption, excitation and emission band maxima are summarised in **Table 2**. The emission spectrum is typical for a 1,3,5,7-tetramethyl BODIPY core [2,14]. BODIPY **1b** exhibits low to moderate fluorescent and a very low singlet oxygen quantum yield (**Table 2**). During the course of the photoirradiation for the singlet oxygen quantum yield determination, the main absorption band did not show any significant decrease. This provides an indication of high photostability.

Table 2. Photophysical and photochemical data for BODIPY **1b**.

	λ_{Abs} (nm)	λ_{exc} (nm)	λ_{em} (nm)	Stokes shift (cm^{-1})	Φ_F	log ε	Φ_Δ
DMSO	505	504	515	384	0.05	4.43	---
EtOH	504	503	513	348	0.48	---	---
THF	503	502	511	311	0.14	---	(0.06)

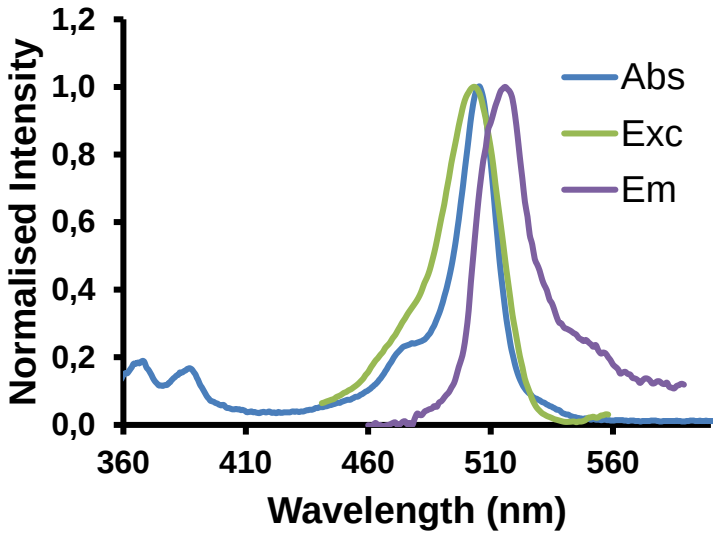

Figure 3.4. Normalised absorption (*blue*), excitation (*green*) and emission (*purple*) spectra of BODIPY **1b** in DMSO.

3.3. 8-(4-Nitrophenyl)-1,3,5,7-tetramethylBODIPY 1c

3.3.1 Synthesis of BODIPY 1c

BODIPY **1c** has been reported previously [118] and was synthesised as a precursor for further reduction of the *meso*-nitrophenyl moiety to a *meso*-aminophenyl moiety to prepare dyes suitable for conjugation to MNPs. The synthesis route is analogous to those of BODIPYs **1a** and **1b** (**Scheme 12**).

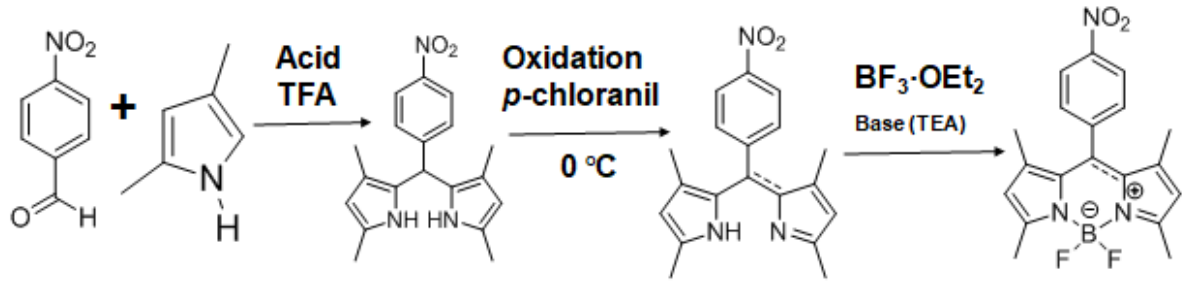

Scheme 12. One-pot acid-catalysed synthesis of BODIPY **1c**.

3.3.2 Characterisation of BODIPY 1c

The eighteen protons of BODIPY **1c** can be identified from the ^{1}H NMR spectrum signals. The doublets that lie at 8.34 and 7.51 ppm integrate to two protons each and represent the four phenyl protons. A singlet at 6.01 ppm can be assigned to the protons at the 2,6-positions on the BODIPY core. The twelve proton signals that lie at 1.33 and 2.53 ppm result from the twelve methyl protons on the pyrrole core. In the FT-IR spectrum, the peaks normally expected for a BODIPY core dye are observed. Bands that lie between 2852−2917 cm^{-1} are attributed to the C-H stretch of the terminal methyl groups, while N-C stretch bands associated with the pyrrolic nitrogen atoms lie between 1075−1408 cm^{-1}. A peak at 468 cm^{-1} can be assigned to C-H stretches at the 2,6-positions of the BODIPY core.

3.3.3. Spectroscopic properties of BODIPY 1c

BODIPY **1c** exhibits a typical *meso*-substituted BODIPY absorption spectrum with a band maximum at 503 nm in DMSO (**Figure 3.5**). There is no evidence of band broadening due to aggregation. The absorption, excitation and emission band maxima are summarised in **Table 3**. The emission spectrum is typical for a 1,3,5,7-tetramethyl BODIPY core. BODIPY **1c** is not highly fluorescent due to the presence of the *meso*-aryl group. There is also a very low singlet oxygen quantum yield since there are no heavy atoms on the BODIPY core.

Table 3. Photophysical and photochemical data for BODIPY **1c**.

	λ_{Abs} (nm)	λ_{exc} (nm)	λ_{em} (nm)	Stokes shift (cm^{-1})	Φ_F	log ε	Φ_Δ
DMSO	503	506	514	425	0.03	4.77	0.01
EtOH	503	504	512	349	0.02	---	---
THF	501	506	511	390	0.17	---	---

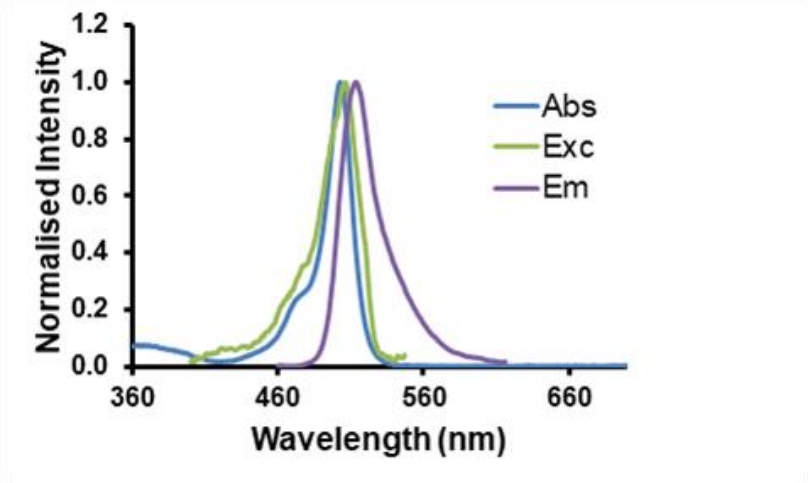

Figure 3.5. Normalised absorption (*blue*), excitation (*green*) and emission (*purple*) spectra of BODIPY **1c** in DMSO.

3.4. 8-(4-Dimethylaminophenyl)-1,3,5,7-tetramethylBODIPY 1d.

3.4.1. Synthesis of BODIPY 1d

BODIPY **1d** has been reported previously [119] and was synthesised as a precursor for π-extended BODIPY analogues that were used in non-linear optics and in photocatalytic degradation. The synthetic route is akin to that of BODIPYs **1a-c** and entails the TFA-catalysed ‘’one-pot three-step’’ condensation of 2, 4-dimethylpyrrole and 4-dimethylaminobenzaldehyde in DCM (**Scheme 13**).

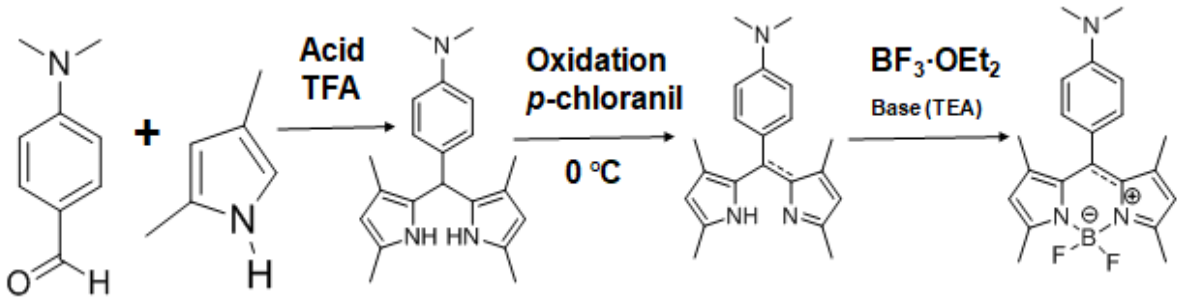

Scheme 13. Acid-catalysed one-pot synthesis of BODIPY **1d**.

3.4.2 Characterisation of BODIPY 1d

The twenty-four protons of BODIPY **1d** can are readily identified in the ^{1}H NMR spectrum. Singlet signals at 6.73 and 7.01 ppm integrate to two protons each and can be assigned to the four phenyl protons. Singlet signals at 1.43 and 2.49 ppm can be attributed to the twelve methyl protons on the pyrrole core, while a singlet signal at 2.96 ppm can be attributed to the six dimethylamino protons. The singlet signal at 5.91 ppm with two protons is assigned to the protons at the 2,6-positions of the BODIPY core. In the FT-IR spectrum, the peaks normally expected for a BODIPY core dye are observed [115,116]. Bands that lie between 2853−2911 cm^{-1} are attributed to the C-H stretch of the terminal methyl groups, while N-C stretch bands associated with the pyrrolic nitrogen atoms lie between 1049−1456 cm^{-1}. A peak at 468 cm^{-1}can is assigned to C-H stretches at the 2,6-positions of the BODIPY core.

3.4.3. Spectroscopic properties of BODIPY 1d

BODIPY **1d** exhibits a typical *meso*-substituted BODIPY absorption spectrum with a band maximum at 500 nm in DMSO (**Figure 3.6**). There is no evidence of band broadening due to aggregation. The absorption, excitation and emission band maxima are summarised in **Table 4**. The emission spectrum is typical of that of a 1,3,5,7-tetramethyl BODIPY core [14]. BODIPY **1d** is not highly fluorescent due to a PET (photoelectron transfer process) involving the lone pair of electrons on the dimethylamino nitrogen. BODIPY **1d** also exhibits a negligible singlet oxygen quantum yield.

Table 4. Photophysical and photochemical data for BODIPY **1d**.

	λ_{Abs} (nm)	λ_{exc} (nm)	λ_{em} (nm)	Stokes shift (cm^{-1})	Φ_F	log ε	Φ_Δ
DMSO	500	503	512	468	0.11	4.45	< 0.01
EtOH	499	503	509	393	0.13	---	---
THF	500	504	511	430	0.10	---	---

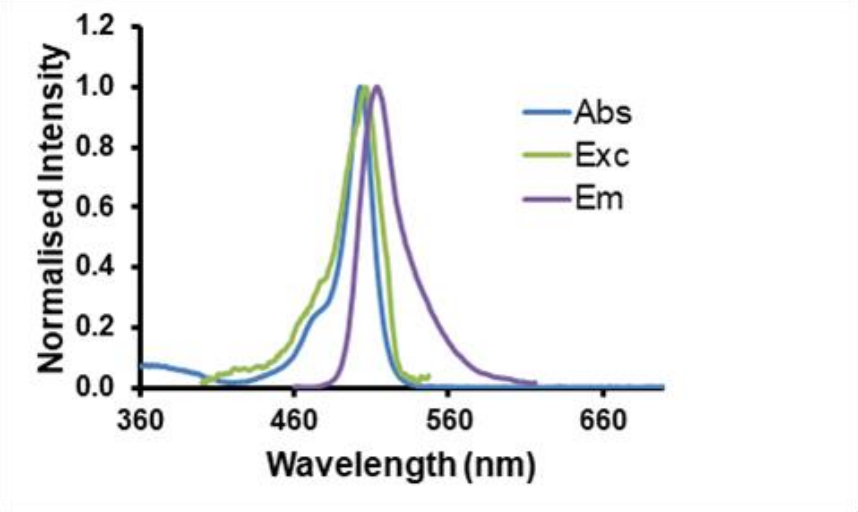

Figure 3.6. Normalised absorption (*blue*), excitation (*green*) and emission (*purple*) spectra of BODIPY **1d** in DMSO. 4,4'-Difluoro-8-(4-methoxyphenyl)-1,3,5,7-tetramethyl-4-bora-3a, 4a-diaza-*s*-indacene (**1e**).

3.5 8-(4-Carboxymethylphenyl)-1,3,5,7-tetramethylBODIPY 1e

3.5.1. Synthesis of BODIPY 1e

The synthesis of BODIPY **1e** has been reported previously [120]. **1e** was synthesised as a precursor for more complex analogues after hydrolysis of the ester moiety to enable conjugation to nanoparticles. The synthesis follows the classical "one-pot three-step" TFA-catalysed condensation of 2,4-dimethylpyrrole and methyl-4-formylbenzoate in DCM (**Scheme 14**).

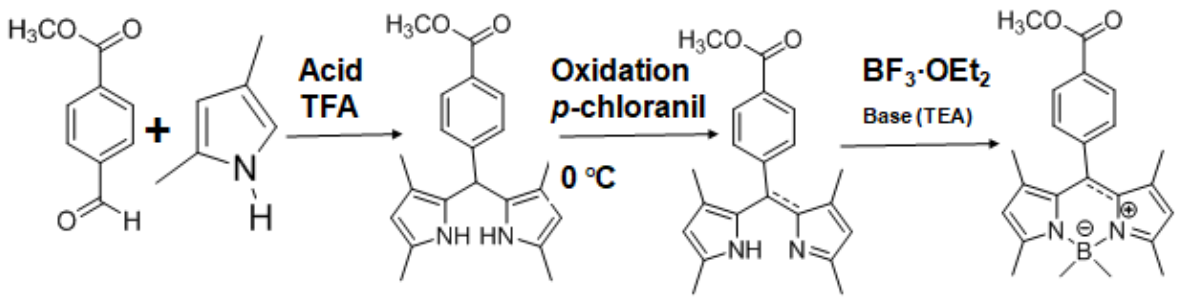

Scheme 14. Acid-catalysed one-pot synthesis of BODIPY **1e**.

3.5.2 Characterisation of BODIPY 1e

The twenty-three protons of BODIPY **1e** can be readily identified in the ^{1}H NMR spectrum. The singlet peaks at 7.42 and 8.20 ppm integrate to two protons each and can be assigned to the four phenyl protons. The singlet peak at 6.01 ppm integrates to two protons and can be assigned to the protons at the 2,6-positions of the BODIPY core. The singlet signals at 1.38 and 2.58 ppm can be attributed to the twelve methyl protons on the pyrrole core. A singlet at 4.00 ppm integrates to three protons and can be attributed to the methyl group of the *meso*-aryl ring. In the FT-IR spectrum, the peaks normally expected for a BODIPY core dye are observed [115,116]. Bands that lie between 2851−2920 cm^{-1} are attributed to the C-H stretch of the terminal methyl groups, while N-C stretch bands associated with the pyrrolic nitrogen atoms lie between 1190−1401 cm^{-1}. A peak at 509 cm^{-1} can be assigned to C-H stretches at the 2,6-positions of the BODIPY core.

3.5.3. Spectroscopic properties of BODIPY 1e

BODIPY **1e** exhibits a typical *meso*-substituted BODIPY absorption spectrum with a band maximum at 501 nm in DMSO (**Figure 3.7**). There is no evidence of band broadening due to aggregation. The absorption, excitation and emission band maxima are summarised in **Table 5**. The emission spectrum is typical of that of a 1,3,5,7-tetramethyl BODIPY core [1,2,14]. BODIPY **1e** is moderately fluorescent (**Table 5**) due to the absence of heavy atoms and negligible intersystem crossing. A low singlet oxygen quantum yield was obtained for this dye.

Table 5. Photophysical and photochemical data for BODIPY **1e**.

	λ_{Abs} (nm)	λ_{exc} (nm)	λ_{em} (nm)	Stokes shift (cm^{-1})	Φ_F	log ε	Φ_Δ
DMSO	501	500	515	542	0.35	4.56	0.04
EtOH	500	499	512	468	0.47	---	---
THF	502	501	515	503	0.37	---	---

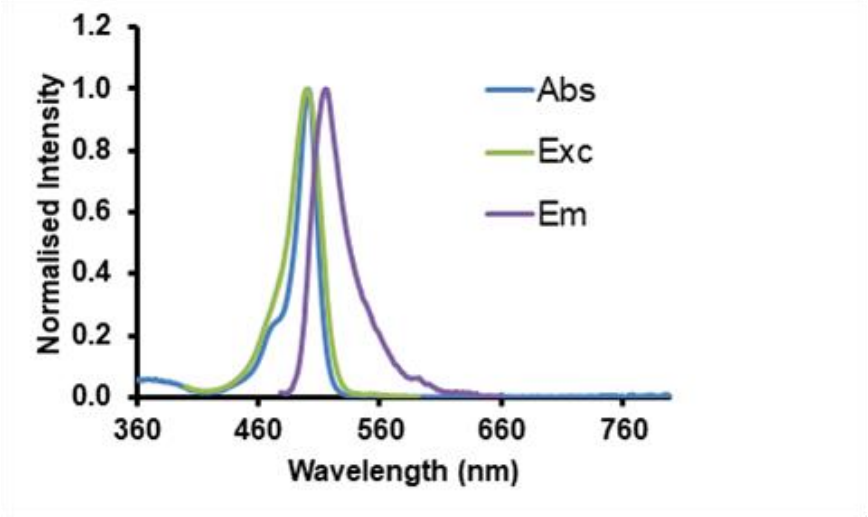

Figure 3.7. Normalised absorption (*blue*), excitation (*green*) and emission (*purple*) spectra of BODIPY **1e** in DMSO.

3.6. Synthesis and characterisation of BODIPY 2a

BODIPY **2b,** a compound that has been previously reported was synthesised from **(1b)** using NBS (**Scheme 16**) [121].

3.6.1. Synthesis of BODIPY 2a

The 2,6-positions of a 1,3,5,7-tetramethylBODIPYcore dye are the most positively charged, hence the most vulnerable position for an electrophilic attack. BODIPY **2a** was synthesised from BODIPY **1a** using NBS (**Scheme 15**). Due to the high reactivity of NBS; the duration of the reaction is relatively short**.**

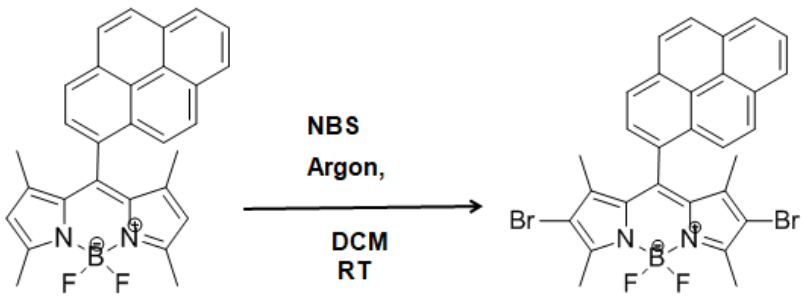

Scheme 15. Halogenations of BODIPY **1a** to yield BODIPY **2a**.

3.6.2 Structural Analysis of BODIPY 2a

In the ^{1}H NMR spectrum of BODIPY **2a**, all twenty-one protons can be readily identified (**Figure 3.8**). Within the aromatic region, the signals in the 7.88−8.33 ppm region again integrate to nine protons in a similar manner to those in the aromatic region of the spectrum of **1a** and can hence be attributed to the *meso*-pyrenyl ring. The singlet signals at 1.59 and 2.70 ppm integrate to six protons each and can be attributed to the six protons of the methyl groups on the BODIPY core. The absence of a singlet signal at 5.99 ppm confirms that the two protons at the 2,6-positions have been replaced by bromines. The predicted molecular mass for BODIPY **2a** is 606.1 amu. In the MALDI-TOF mass spectrum, the primary peak was observed at 605.5 m/z $[M]^{+}$. The FT-IR spectrum of BODIPY **2a** contains similar vibrations to that of BODIPY **1a**. The appearance of a peak at 524 cm^{-1} is an indication of the addition of bromine atoms at the 2,6-positions since this peak can be attributed to the C-Br stretch.

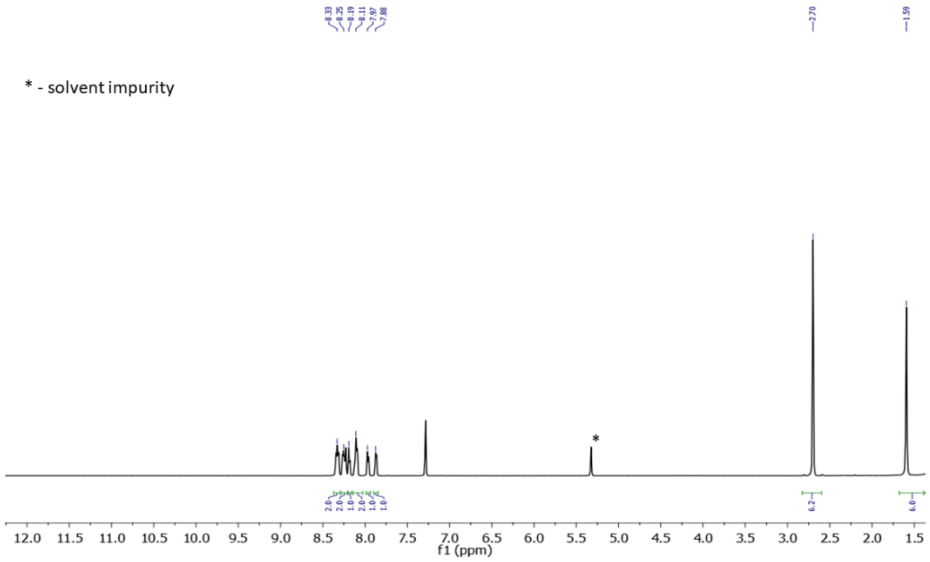

Figure 3.8. ^{1}H NMR spectrum of BODIPY **2a** in $CDCl_3$

3.6.3. Spectroscopic properties of BODIPY 2a

BODIPY**2a** has an absorption spectrum (**Figure 3.9**) that is typical for a 2,6-dibrominated BODIPY core dye with a red-shifted absorbance maximum at 531 nm in THF. The absorption,

excitation and emission band maxima are summarised in **Table 6**. There is no evidence of band broadening due to aggregation. The fluorescence quantum yield for the dye shows a drastic decrease with respect to the analogous non-brominated BODIPY cores due to the heavy atom effect. As anticipated, the dye has a very high singlet oxygen quantum yield value (**Figure 3.10**).

Table 6. Photophysical and photochemical data for BODIPY **2a**.

	λ_{Abs} (nm)	λ_{exc} (nm)	λ_{em} (nm)	Stokes shift (cm^{-1})	Φ_F	log ε	Φ_Δ
DMSO	541	538	546	169	0.05	4.56	---
EtOH	533	529	537	139	0.05	---	0.91
THF	531	526	536	140	0.06	---	---

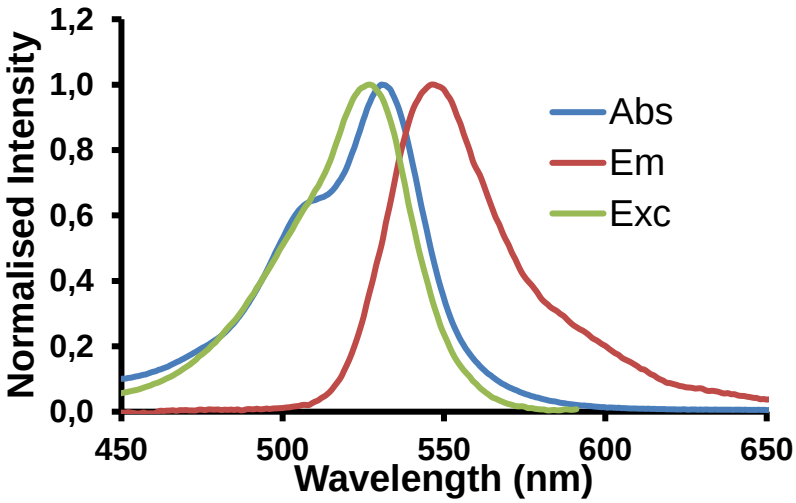

Figure 3.9. Normalised absorption (*blue*), excitation (*green*) and emission (*orange*) spectra of BODIPY **2a** in THF.

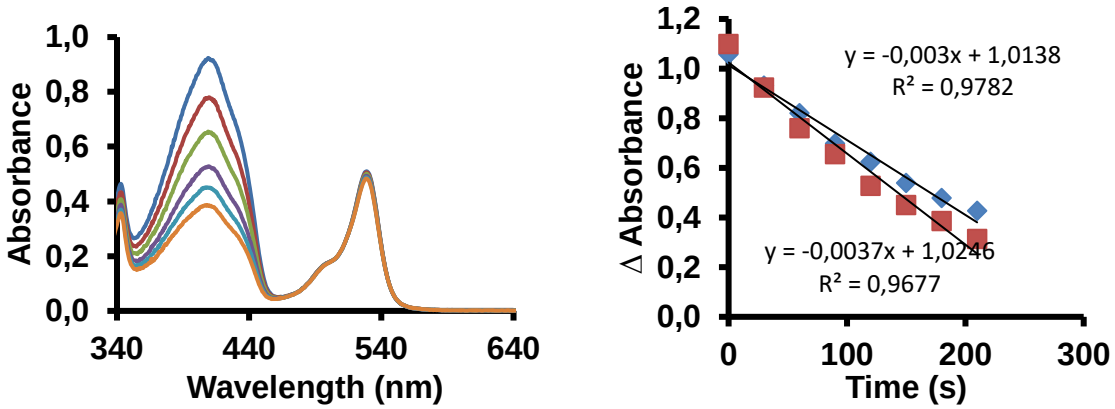

Figure 3.10. Photodegradation of DPBF by BODIPY **2a** monitored at 10 s intervals at 410 nm in EtOH. The Φ_{Δ} value for **2a** was determined using the comparative method with Rose Bengal in EtOH.

3.7. Synthesis and characterisation of BODIPY 2b

3.7.1. Synthesis of BODIPY 2b

BODIPY **2b** was synthesised from BODIPY **1b** using NBS (**Scheme 12**) in a similar manner to the procedure used to form **2a** from **1a.**

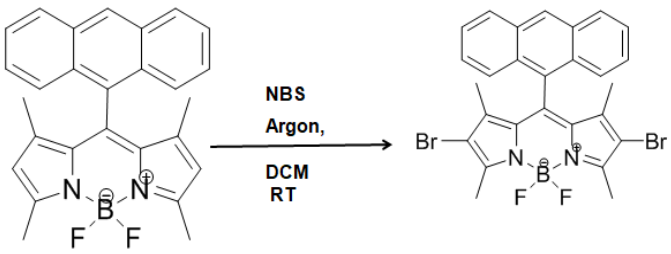

Scheme 16. Halogenation of BODIPY **1b** to yield BODIPY **2b**.

3.7.2 Characterisation of BODIPY 2b

In the ^{1}H NMR spectrum of BODIPY **2b**, twenty-one protons can be readily identified. Within the aromatic region, the signals in the 7.43−8.68 ppm region again integrate to nine protons in a similar manner to those in the aromatic region of the spectrum of **1b** and can hence be attributed to the *meso*-anthracyl ring. The singlet signals at 0.64 and 2.64 ppm integrate to six

protons each and can be attributed to the six protons of the methyl groups on the BODIPY core. The absence of the singlet signal of **1b** at 6.12 ppm confirms that the two protons at the 2,6-positions have been replaced by bromines. The predicted molecular mass for BODIPY **2b** is 582.01 amu. In the MALDI-TOF mass spectrum (**Figure 3.11**); the primary peak was observed at 583.01 m/z $[M+H]^+$. The FT-IR spectrum of BODIPY **2b** contains similar vibrations to that of BODIPY **1b**. The appearance of a peak at 521 cm^{-1} is an indication of the addition of bromine atoms at the 2,6-positions since this peak can be attributed to the C-Br stretch.

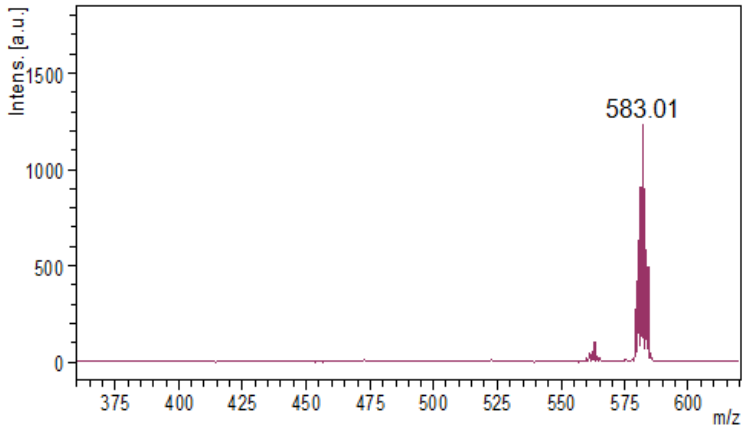

Figure 3.11. MALDI-TOF mass spectrum of BODIPY **2b**.

3.7.3 Spectroscopic properties of BODIPY 2b

BODIPY **2b** has an absorption spectrum (**Figure 3.12**) that is typical for a 2,6-dibrominated BODIPY core dye with a red-shifted absorbance maximum at 535 nm in THF. The absorption, excitation and emission band maxima are summarised in **Table 7**. There is no evidence of band broadening due to aggregation. The fluorescence quantum yield for the dye shows a drastic decrease with respect to the analogous non-brominated BODIPY cores due to the heavy atom effect. As anticipated, the dye has a very high singlet oxygen quantum yield value.

Table 7. Photophysical and photochemical data for BODIPY **2b**.

	λ_{Abs} (nm)	λ_{exc} (nm)	λ_{em} (nm)	Stokes shift (cm^{-1})	Φ_F	log ε	Φ_Δ
DMSO	542	538	549	235	0.003	4.56	---
EtOH	535	533	542	241	0.004	---	0.62
THF	535	534	541	207	0.04	---	---

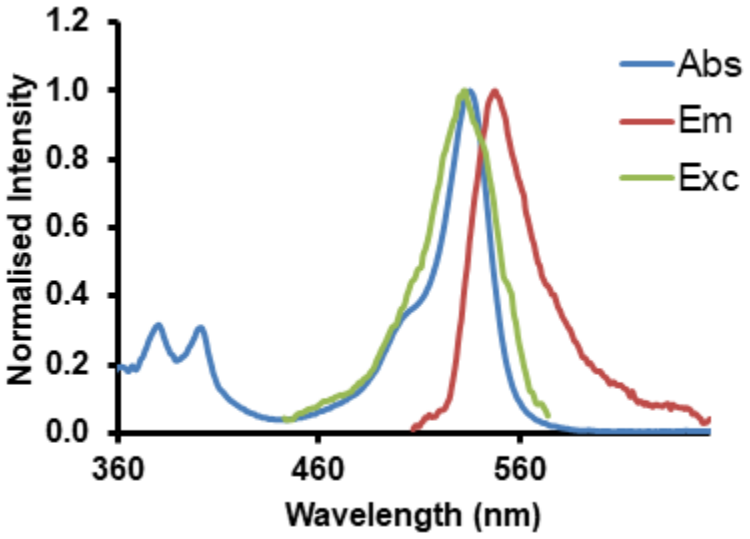

Figure 3.12. Normalised absorption (*blue*), excitation (*green*) and emission (*orange*) spectra of BODIPY **2b** in THF.

3.8. Synthesis and characterisation of BODIPYs 2-e

3.8.1 Synthesis of BODIPYs 2c-e.

The synthesis of BODIPY dyes **2c-e** with bromines substituted at the 2,6-positions to form a series of previously reported compounds [122], follows a similar halogenation procedure in the presence of NBS in DCM [11] by making use of BODIPYs **1c-e** as precursors (**Scheme 17**).

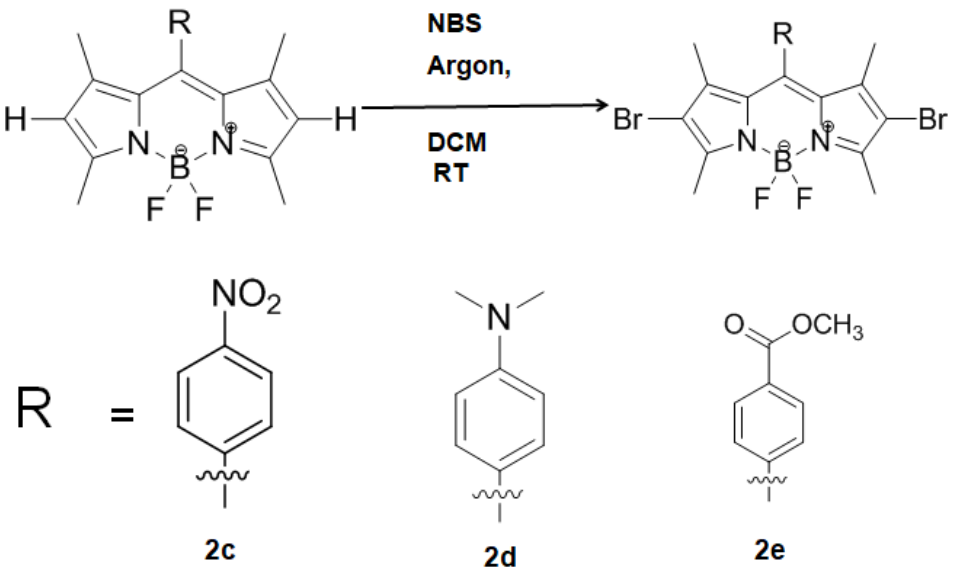

Scheme 17. Halogenation of BODIPYs **1c-e** to yield BODIPYs **2c-e**.

3.8.2. Characterisation of BODIPYs 2c-e

3.8.2.1. Characterisation of BODIPY 2c

The ^{1}H NMR spectrum contains all sixteen protons of BODIPY **2c**. Doublets that lie at 8.57 and 7.67 ppm integrate to two protons each and can be attributed to the four phenyl protons. Singlet signals at 2.76 and 1.50 ppm each integrate to six protons and can be assigned to the twelve methyl groups on the BODIPY core. The absence of a singlet peak at 6.22 ppm demonstrates that the hydrogen atoms at the 2,6-positions of the BODIPY core have been substituted with bromine atoms. The predicted molecular mass for BODIPY **2d** is 526.97 amu. In the MALDI-TOF mass spectrum, the primary peak was observed at 526.20 m/z $[M]^{+}$. The FT-IR spectrum of BODIPY **2c** contains similar bands to that of BODIPY **1c**. The appearance of a peak at 523 cm^{-1} is an indication of the addition of bromine atoms at the 2,6-positions since the peak can be attributed to the C-Br stretch.

3.8.2.2. Characterisation of BODIPY 2d

All twenty-two protons can be readily identified in the ^{1}H NMR spectrum of BODIPY **2d**. Two singlet peaks at 8.47 and 7.82 ppm which integrate into two protons each can be attributed to the four phenyl protons. The singlet at 3.39 ppm is attributed to the six methyl group protons of the dimethylamino group, while singlets at 1.37 and 1.24 ppm integrate to six protons each and can be assigned to the four methyl group on the BODIPY core. The absence of a singlet peak at 6.22 ppm demonstrates that the hydrogen atoms at the 2,6-positions of the BODIPY core have been substituted with bromine atoms. The predicted molecular mass for BODIPY **2d** is 525.02 amu. In the MALDI-TOF mass spectrum, the primary peak was observed at 526.08 m/z $[M+H]^{+}$. The FT-IR spectrum of BODIPY **2d** contains similar bands to that of BODIPY **1d**. The appearance of a peak at 522 cm^{-1} is an indication of the addition of bromine atoms at the 2,6-positions since the peak can be attributed to the C-Br stretch.

3.8.2.3. Characterisation of BODIPY 2e

The ^{1}H NMR spectrum contains all nineteen protons anticipated for BODIPY **2e.** Doublet signals which integrate into two protons each at 7.42 and 8.26 ppm can be assigned to the four phenyl protons. A singlet signal integrating to three protons at 4.02 ppm arises from the protons of the ester group, while peaks at 1.27 and 0.89 ppm integrate to six protons and can be assigned to the twelve methyl group protons of the BODIPY core. The absence of a singlet signal at 6.22 ppm with respect to BODIPY **1e** demonstrates that the hydrogen atoms at the 2,6-positions of the BODIPY core have been substituted with bromine atoms. The predicted molecular mass for BODIPY **2e** is 539.54 amu. In the MALDI-TOF mass spectrum, the primary peak was observed at 540.0 m/z $[M]^{+}$. The FT-IR spectrum of BODIPY **2e** contains similar vibrations to that of BODIPY **1e**. The appearance of a peak at 521 cm^{-1} is an indication of the addition of bromine atoms at the 2,6-positions since the peak can be attributed to the C-Br stretch.

3.8.3. Spectroscopic properties of BODIPYs 2c-e

Generally, BODIPYs **2c-e** exhibit absorption spectra (**Figure 3.13**) typical of 2,6-dibrominated BODIPY core dyes with red-shifted absorbance maxima at 534, 536 and 534 nm, respectively, in THF. The absorption, excitation and emission band maxima are summarised in **Table 8**. There is no evidence of band broadening due to aggregation. The fluorescence quantum yield for the dyes shows a significant decrease with respect to the analogous non-brominated BODIPY cores due to the heavy atom effect. As anticipated, the dyes also have very high singlet oxygen quantum yield values.

Table 8. Photophysical and photochemical data for BODIPYs **2c-e**.

	λ_{Abs} (nm)	λ_{exc} (nm)	λ_{em} (nm)	Stokes shift (cm^{-1})	Φ_F	log ε	Φ_Δ
				2c			
DMSO	534	531	542	276	0.07	4.56	---
EtOH	532	529	539	244	0.004	---	0.62
THF	534	530	541	242	0.31	---	---
				2d			
DMSO	538	536	547	305	---	---	---
EtOH	534	533	542	276	---	---	0.56
THF	536	534	541	207	---	---	---
				2e			
DMSO	536	535	544	274	0.04	---	---
EtOH	535	534	540	173	0.31	---	0.65
THF	534	531	541	242	0.26	---	---

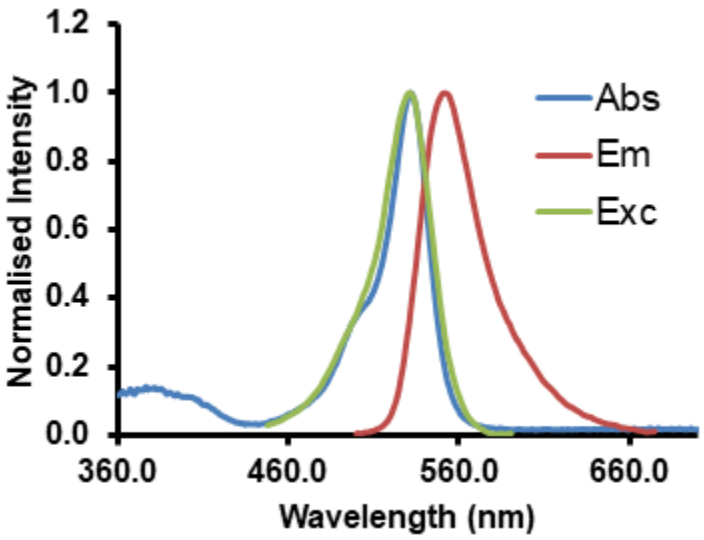

Figure 3.13. Normalised absorption (*blue*), excitation (*green*) and emission (*orange*) spectra of BODIPY **2c** in DMSO as a typical example.

3.9. 8-Pyrenyl-1,7-dimethyl-2,6-dibromo-3,5-di-4-carboxystyrylBODIPY 3

3.9.1. Synthesis of BODIPY 3

The synthesis of BODIPY **3** (**Scheme 18**) was achieved using a modified Knovenagel condensation reaction by using BODIPY **2a** and 4-formylbenzoic acid as precursors.

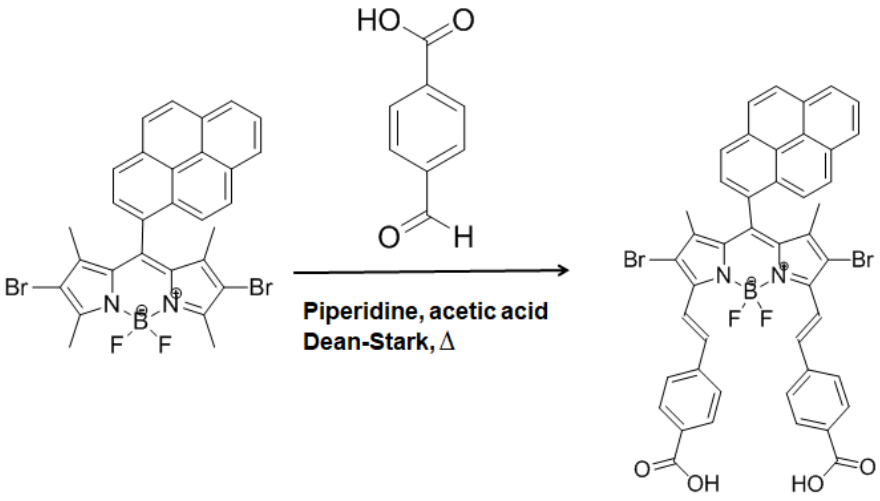

Scheme 18. Knoevenagel condensation reaction to form BODIPY **3**.

3.9.2. Structural Analysis of BODIPY 3

In the ^{1}H NMR spectrum of BODIPY **3**, all twenty-nine protons can be readily identified**.** A two proton singlet at 13.02 ppm can be attributed to the carboxy-phenyl protons. A four proton singlet at 8.67 ppm and a four proton multiplet signal at 6.99−7.05 ppm can be attributed to the eight protons of the styryl phenyl rings. Two proton singlets at 8.38 and 8.13 ppm can be assigned to the four protons of the bridging alkenes between the styryl group and the BODIPY core. A four proton multiplet signal that lies between 7.90−7.97 ppm, a two proton doublet signal at 7.81 ppm, and a three proton multiplet at 7.48−7.52 ppm, can be attributed to the nine protons of the *meso*-pyrenyl ring. A six proton singlet at 3.25 ppm can be assigned to the methyl groups on the BODIPY core. The molecular mass predicted for BODIPY **3** is 870.34 amu. In the MALDI-TOF mass spectrum, the primary peak lies at 870.66 m/z (**Figure 3.14**)**.** A second peak at 851.61 corresponds to **3** with a fluorine atom removed.

The FT-IR spectrum of **3** contains many of the same peaks as core dye **2a**, including peaks anticipated for the BODIPY core [115,116], including a band at 2850 cm^{-1} assigned to the C-H stretch of the terminal methyl groups, and pyrrolic N-C stretch bands from 1060−1435 cm^{-1}. The C=O carboxylic stretch is observed at 1683 cm^{-1}, while the carboxylic hydroxyl stretch lies at 3154 cm^{-1}. The C-Br stretch lies at 516 cm^{-1} and a styryl C=C stretch lies between 1520−1604 cm^{-1}.

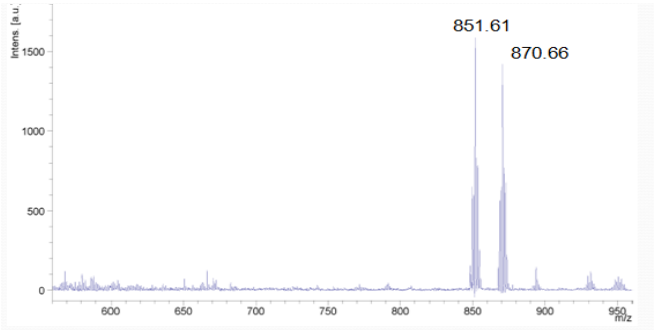

Figure 3.14. MALDI-TOF mass spectrum of BODIPY **3**.

3.9.3. Spectroscopic properties of BODIPY 3

The absorption spectrum for BODIPY **3** (**Figure 3.15**) is typical for a 3,5-distyrylBODIPY dye with an absorbance maximum observed at 657 nm in DMSO. The absorption, emission and excitation band maxima values are summarised in **Table 9**. There is no sign of band broadening due to aggregation. The relatively intense absorption between 320−400 nm is associated with the *meso*-pyrenyl substituent. The fluorescence quantum yield of BODIPY **3** is relatively low due to the heavy atom effect associated with the bromine atoms, and there is a moderately high singlet oxygen quantum yield value (**Figure 3.16**).

Table 9. Photophysical and photochemical data for BODIPY **3**.

	λ_{Abs} (nm)	λ_{exc} (nm)	λ_{em} (nm)	Stokes shift (cm^{-1})	Φ_F	log ε	Φ_Δ
DMSO	657	659	669	273	0.02	4.10	---
EtOH	649	651	658	210	0.15	---	0.32
THF	650	653	659	210	0.24	---	---

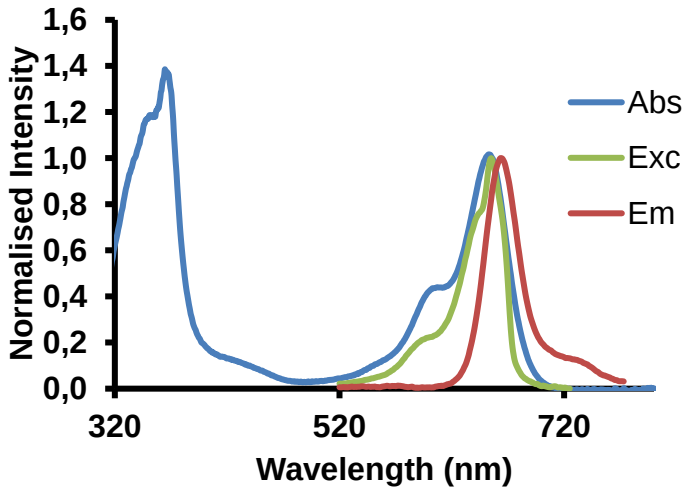

Figure 3.15. Normalised absorption *(blue)*, excitation *(green)* and emission *(orange)* spectra of BODIPY **3** in DMSO.

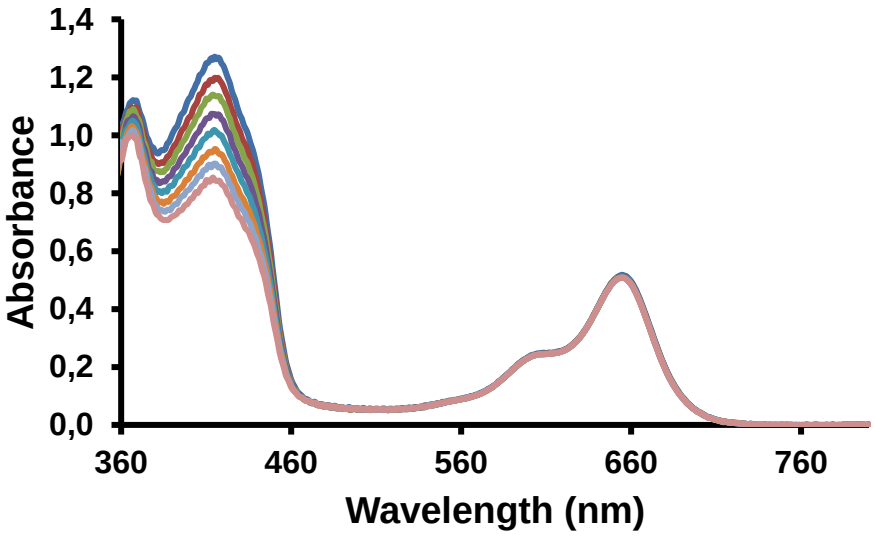

Figure 3.16. Photocatalytic degradation of DPBF monitored at 410 nm in EtOH by BODIPY **3**at 10 s intervals. The Φ_{Δ} value for **3** was determined using the comparative method with ZnPc in DMSO.

3.10. 8-Phenyl-1,7-dimethyl-2,6-diiodo-3,5-di-2-thienylvinyleneBODIPY 4

3.10.1 Synthesis of BODIPY 4

BODIPY **6** was synthesised by Dr Lizhi Gai at Nanjing University in the manner reported previously [90].

3.10.2. Structural analysis of BODIPY 4

All twenty-one protons were readily assigned in the ^{1}H NMR spectrum of BODIPY **4** [90]. Within the aromatic region from 8.5−7.0 ppm, the peaks integrate to the anticipated fifteen protons. Below 7.0 ppm, the absence of a singlet signal that integrates into two protons confirms the addition of bromines at the 2,6-positions, replacing the hydrogen atoms at this position. The absence of a singlet peak slightly below 7.0 ppm that integrates to 2 protons confirmed that the hydrogen atoms at the 2,6-positions had been replaced with iodine atoms.

3.10.3. Spectroscopic properties of BODIPY 4

The absorption spectrum for BODIPY **4** is typical of a 3,5-distyrylBODIPY dye (**Figure 3.17**), with an absorbance maximum at 673 nm in DMSO. The absorption, emission and excitation band maxima values in DMSO are summarised in **Table 10**. Shows the absorption, emission and excitation spectra in DMSO with no signs of aggregation.

Table 10. Photophysical and photochemical data for BODIPY **4** in DMSO.

	λ_{Abs} (nm)	λ_{exc} (nm)	λ_{em} (nm)	Stokes shift (cm^{-1})	Φ_F	τ_F (ns)	log ε	Φ_Δ
DMSO	673	675	699	552	0.04	3.92	4.73	0.45

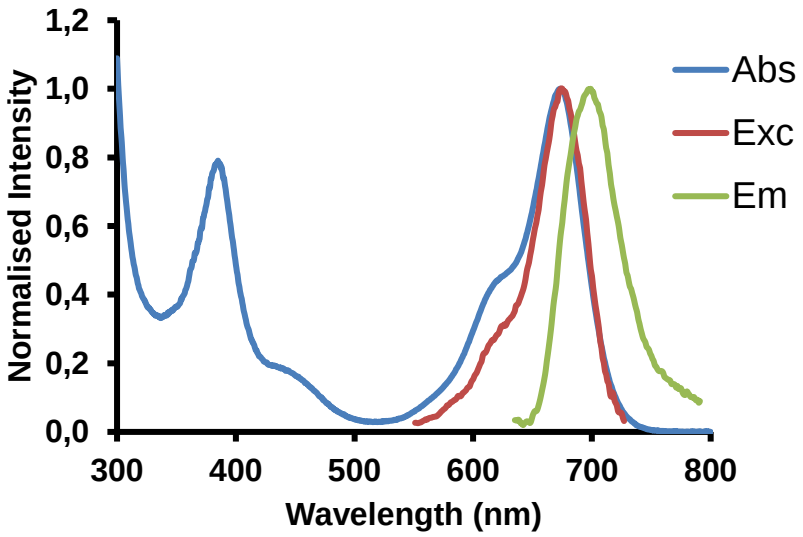

Figure 3.17. Normalised absorption *(blue)*, excitation *(orange)* and emission *(purple)* spectra of BODIPY **4** in DMSO.

3.11. 8-Anthracyl-1,7-dimethyl-2,6-dibromo-(4-carboxy)-3,5-distyrylBODIPY 5

3.11.1. Synthesis of BODIPY 5

A modified Knoevenagel condensation was used (**Scheme 19**) for the synthesis of BODIPY (**5**) from 4,4′-Difluoro-2,6-dibromo-(8-anthracyl)-1,3,5,7-tetramethyl-2,6-dibromo-4-bora-

3a,4a-diaza-*s*-indacene **(2b)**. The solution changed colour from deep-blue to green indicating the formation of a distyrylBODIPY dye. BODIPY **5** was obtained using column chromatography with chloroform: methanol (3:2) used as the eluent.

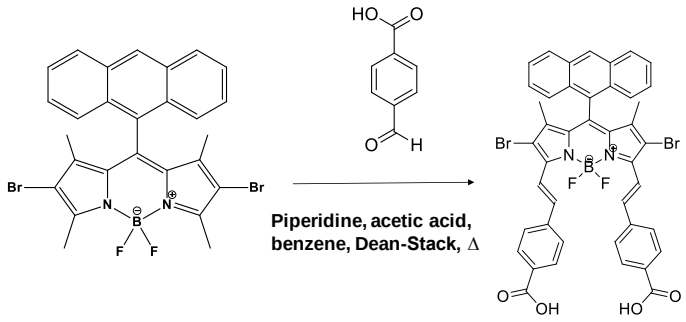

Scheme 19. Knoevenagel condensation reaction to form BODIPY **5**.

3.11.2. Characterisation of BODIPY 5

All twenty-nine protons can be identified in the ^{1}H NMR spectrum of BODIPY **5**. A two proton singlet signals at 8.24 ppm can be attributed to the carboxyl groups. A four proton doublet signal at 6.32 ppm and a four proton multiplet between 6.21−6.28 ppm can be assigned to the eight protons of the styryl phenyl rings. A four proton singlet of 6.12 ppm, a three proton doublet signal at 6.03 ppm, and a two proton singlet at 5.96 ppm can be assigned to the nine protons of the *meso*-anthracyl ring. Singlet signals at 4.73 and 4.64 ppm integrate to two protons each and can be assigned to the bridging alkene groups between the styryl and the BODIPY core. A six proton singlet at 0.67 ppm can be assigned to the methyl group in the BODIPY core. The molecular mass predicted for BODIPY **5** was 846.36 amu, and this was confirmed by MALDI-TOF mass spectrometry by the primary peak obtained at 846.88 m/z (**Figure 3.18**). The second peak observed at 827.88 m/z corresponds to the BODIPY dye with a fluorine atom removed.

The FT-IR spectrum contains the peaks anticipated for the BODIPY core [115,116]. The C-H stretch of the terminal methyl groups on the BODIPY core lies at 2838 cm^{-1}, while the pyrrolic

N-C stretch bands lie between 1025−1456 cm^{-1}. The hydroxyl stretch for the carboxylic acid groups lies at 3151 cm^{-1}, and the C=O carboxylic stretch lies at 1687 cm^{-1}. The C-Br stretch lies at 517 cm^{-1}, while the styryl C=C stretch lies between 15253−1606 cm^{-1}.

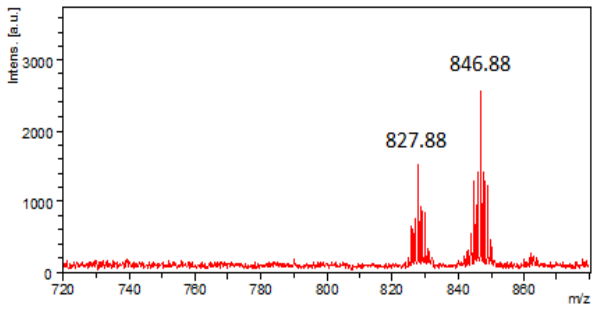

Figure 3.18. MALDI-TOF mass spectrum of BODIPY **5**.

3.11.3. Spectroscopic properties of BODIPY 5

The absorption spectrum of BODIPY **5** is typical of that of a 3,5-distyrylBODIPY dye, with an absorbance maximum at 663 nm in DMSO. The absorption, emission and excitation band maxima values in different solvents are summarised in **Table 11**. There is no sign of aggregation. The relatively intense absorption between 320−400 nm regions is probably associated with the *meso*-anthracyl substituent. A Φ_Δ value of 0.37 was obtained in ethanol (**Figure 3.19**).

Table 11. Photophysical data for BODIPY **5** in different solvents.

	λ_{Abs} (nm)	λ_{exc} (nm)	λ_{em} (nm)	Stokes shift (cm^{-1})	Φ_F	τ_F (ns)	log ε	Φ_Δ
DMSO	663	658	679	355	0.03	2.65	4.58	---
EtOH	659	657	674	337	0.04	---	---	0.37
THF	661	659	677	357	0.05	---	---	---

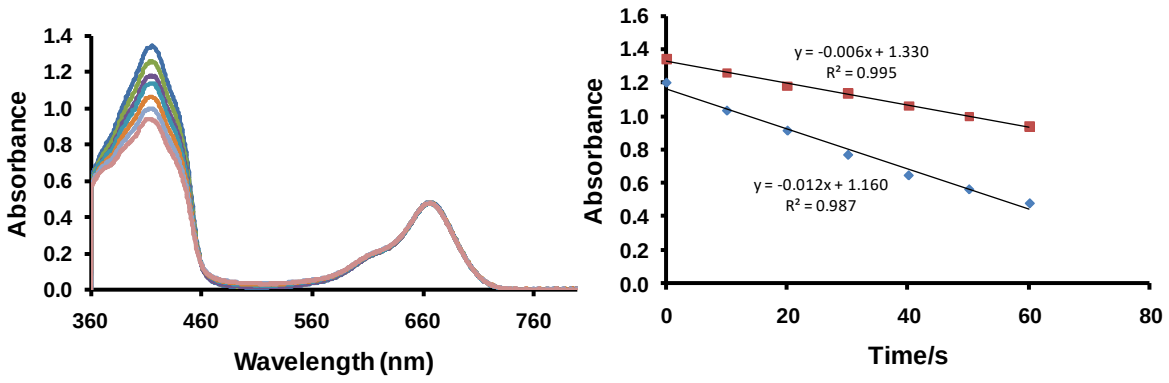

Figure 3.19. Photocatalytic degradation of DPBF (λ_{max} = 410 nm) in EtOH by BODIPY **5** (λ_{max} = 648 nm) at 10 s intervals. The Φ_{Δ} value for **5** was determined using the comparative method with ZnPc in DMSO as the standard (*right*).

3.12 Concluding remarks

BODIPY cores **1a-e**, were synthesised through the classic "one-pot three-step" Lewis acid-catalysed condensation reaction and various techniques were employed for structural characterisation of these dyes. Structurally the cores differ in their *meso*-aryl rings. Photophysical characterisation was conducted on BODIPYs **1a-e,** which generally exhibited similar absorption properties, since the *meso*-aryl ring lies orthogonal to the BODIPY core. The dyes exhibited fluorescence properties that are dependent on solvent polarity. However, both the lifetimes and quantum yields lie in the range generally expected for BODIPY dyes [1]. BODIPYs **1a-e** were brominated at the 2,6-positions to yield BODIPYs **2a-e** with red shifted absorption maxima in the range of ca. 30 nm, relative to their parent BODIPY core dyes. As anticipated, significant singlet oxygen quantum yields were calculated for BODIPYs **2a-e**. BODIPYs **1a-e**, **2a** and **2c-e** have been previously reported. The main novelty in this regard was in their photophysical characterisation. BODIPY **2a** was used to synthesise BODIPY **3**, a new di-styryl BODIPY dye, and another new di-styryl BODIPY **5**, was synthesized from BODIPY **2b.** The two new distyryl dyes were synthesised using a modified version of the Knoevenagel condensation reaction. The main absorption band maxima for BODIPYs **3** and **5** are red shifted far beyond 532 nm, the second harmonic of the Nd:YAG laser which is used to study the optical limiting properties of BODIPY **3** as

discussed in Chapter 7. BODIPYs **3** and **5** were red-shifted into the therapeutic window, with absorption maxima at 657 and 663 nm in DMSO. Their singlet oxygen generating properties (Φ_Δ = 0.32 and 0.37 in DMSO) make these dyes suitable for use as photosensitizers in PACT as discussed in Chapter 6 and in PDT.

CHAPTER 4

4. PHOTOTRANSFORMATION OF ORGANIC POLLUTANTS

This chapter discusses the photocatalytic degradation of organic pollutants using immobilised BODIPY dyes. To the best of our knowledge, the work described in this chapter was the first to apply immobilised BODIPY dyes as photocatalysts in the photodegradation of organic pollutants (Orange G and Methyl Orange). BODIPYs **2a** and **4** were selected for this study because of their high singlet oxygen quantum yields and the ability to form π-π and hydrophobic interactions with the aromatic portion of the polystyrene structure. This chapter of the thesis has been published in two peer-reviewed papers that demonstrated that BODIPY dyes can be used as photocatalysts in solution or when embedded onto solid supports such as polymer fibres. [123]. **Table 12** summarises the photocatalysts used in the degradation of Orange G and Methyl Orange

Table 12. Photocatalysts used and their sizes

	Size of support (μm)	Dye degraded
BODIPY **2a**/PS	1.5-2	Orange G (OG)
BODIPY **4**/PS	2.5	OG and MO

PS fibre = polystyrene fibre, OG = Orange G, MO = Methyl Orange

4.1. Electrospun Polymer nanofibre

This section reports on the spectroscopic and photophysichochemical properties of electrospun polymer fibres that have been functionalised with BODIPY dyes.

4.1.1 Characterisation of functionalised electrospun fibres

Polystyrene was used to embed BODIPY dye complexes (BODIPY **2a**/PS and BODIPY **4**/PS) for use in applications as photocatalysts in the photocatalytic degradation of organic pollutants

(azo dyes). Polystyrene is an aromatic polymer; so there is the possibility of enhanced π-π and hydrophobic interactions between the BODIPY complexes and polystyrene, which hinder leaching out of the dye.

4.1.1.1. Scanning Electron Microscopy (SEM)

Scanning electron microscopy (SEM) analysis was undertaken to determine the size distribution and morphology of the electrospun fibres (**Figure 4.1**). The SEM images reveal that the fibres are cylindrical, unbranched, with a smooth surface even after embedding unto the BODIPY complexes. The size distribution showed that PS alone has an average size of ca.1.0 µm. When the BODIPY complexes were embedded into the PS fibres the average size increases to ca. 2.5 µm for BODIPY **4**/PS and size distribution of between 1.5-2 µm was observed for BODIPY **2a**/PS.

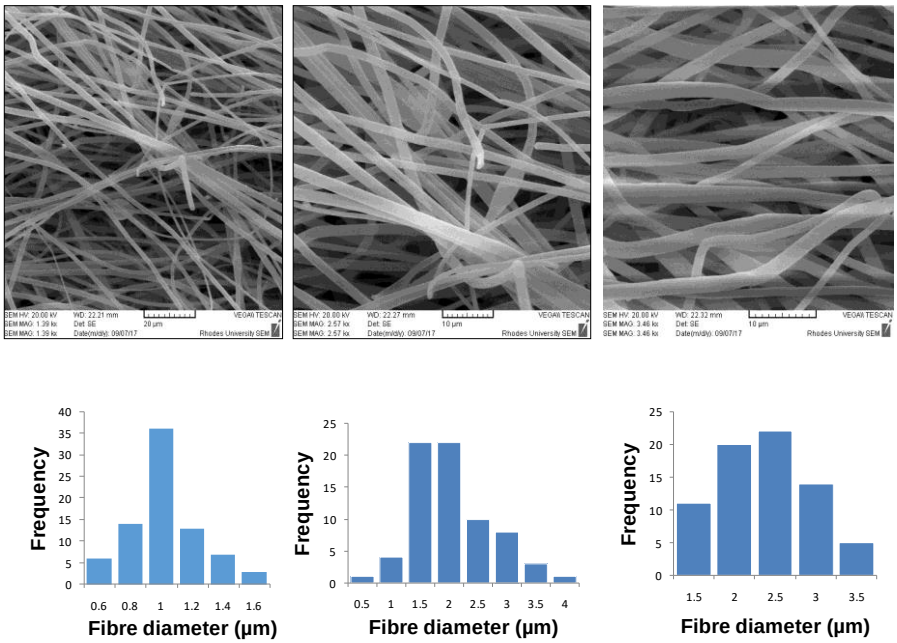

Figure 4.1. SEM images of (A) PS alone, (B) BODIPY **2a**/PS and (C) BODIPY **4**/PS.

4.1.1.2. Energy Dispersive X-ray Spectra

An EDX analysis was conducted to investigate the presence of the expected elements for the PS alone, BODIPY **4**/PS and BODIPY **2a**/PS (**Figure 4.2**). The EDX spectrum for PS alone had the expected C peak, while BODIPY **4**/PS spectrum shows S, Br, B, and F, similar data were obtained for BODIPY **2a**/PS, but Br was observed instead of I since the halogenation in this regard was with bromine and not iodine.

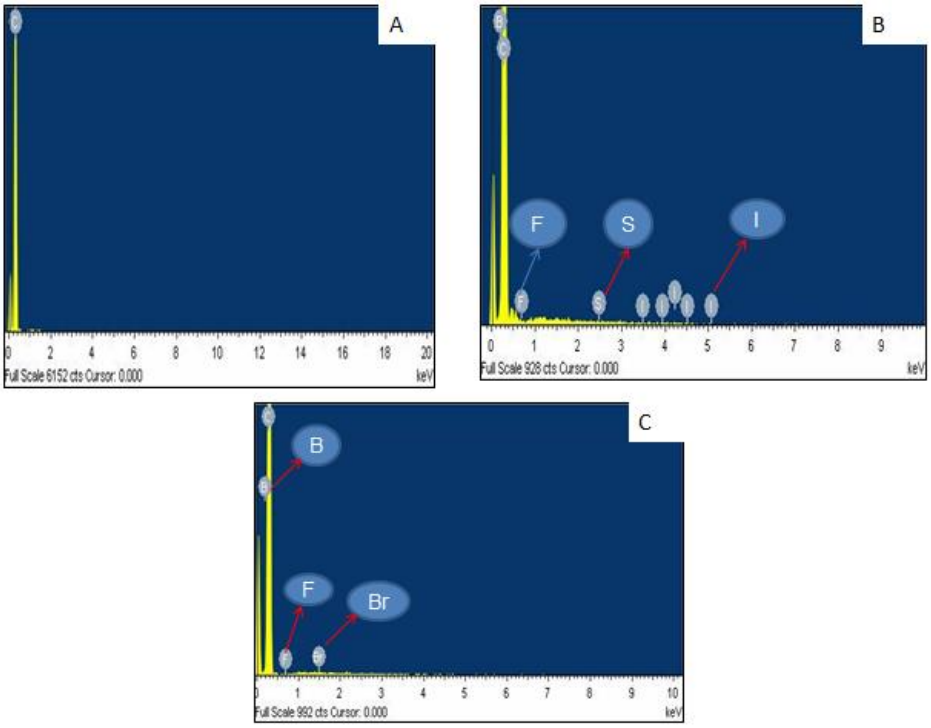

Figure 4.2. EDX data for (A) PS alone, (B) BODIPY **4**/PS and (C) BODIPY **2a**/PS.

4.1.1.3. Solid-state UV-visible absorption spectroscopy

The solid-state UV-visible absorption spectra of BODIPY **2a**/PS and BODIPY **4**/PS are shown in **Figure 4.3**. The main BODIPY spectral band for BODIPY **2a**/PS is red-shifted from 534 nm in solution to 536 nm in the solid state (**Figure 4.3A**), while that of BODIPY **6**/PS blue-shifted from 673 nm in solution to 649 nm. Both spectra showed broadening due to aggregation as is typical for solid state spectra.

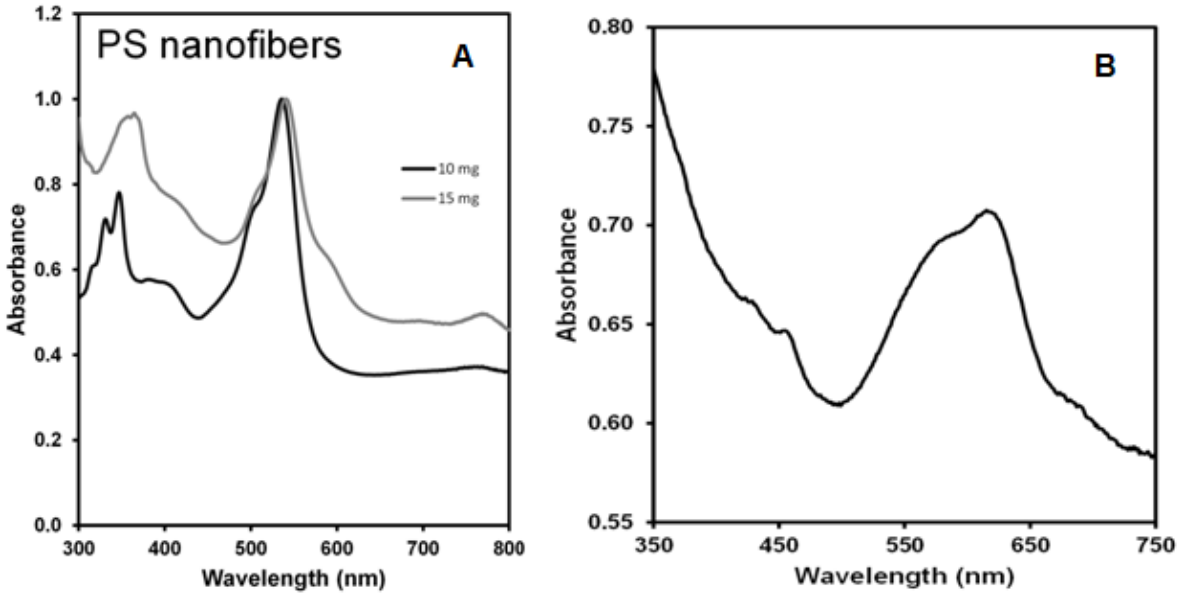

Figure 4.3. UV-visible absorption spectra of A) BODIPY **2a**/PS and BODIPY **4**/PS in the solid state.

4.1.1.4. Singlet Oxygen quantum yields

The role of singlet oxygen in photocatalytic degradation is of great significance, so there is a need to determine the quantum yield of singlet oxygen of the modified fibres in aqueous media. The direct chemical method was used for the studies due to the lack of suitable standards. Determination of the singlet oxygen quantum yield Φ_Δ for BODIPY **4**/PS and BODIPY **2a**/PS in fibres was carried out in a buffered solution (pH 6.7), with ADMA used as the singlet oxygen scavenger and its degradation was monitored at 380 nm (**Figure 4.4**). Prior to irradiation in each case, 20 mg of the modified fibres was submerged in an aqueous solution of ADMA and irradiated at two min intervals. The Φ_Δ values for the BODIPY/PS complexes are listed in (**Table 13**). The data demonstrate that BODIPY/PS complexes maintain their singlet oxygen production properties in the fibres making the modified fibres suitable for use in photocatalytic degradation.

Table 13. Summary of the characterisation of polymer embedded complexes.

Functionalised fibres	Fibre diameter (μm)	λ_{abs}[a]	Φ_{Δ}[a]
PS alone	1.0	---	---
BODIPY **2a**/PS	1.5−2.0	536 (534)	0.25 (0.91)
BODIPY **4**/PS	2.5	649 (673)	0.10 (0.45)

[a]values in brackets are for the photocatalysts in DMSO solution.

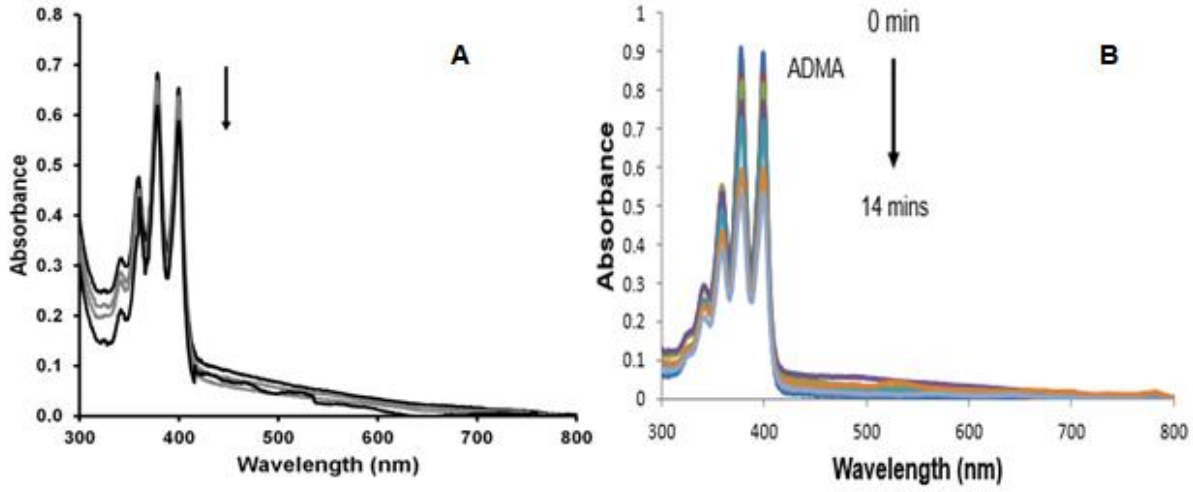

Figure 4.4. UV-visible absorption changes observed using ADMA as a singlet oxygen scavenger in the presence of 20 mg of BODIPY **2a**/PS (**Figure 4.3A**) and BODIPY **4**/PS (**Figure 4.3B**) in aqueous solution.

4.2. Photocatalytic degradation of Orange G

4.2.1. UV-visible absorption spectral changes

The efficacy of BODIPY **2a**/PS and BODIPY **4**/PS as photocatalysts for the photocatalytic degradation of Orange G and Methyl Orange was investigated by following the progress of phototransformation by UV-visible absorption spectroscopy. The observed spectral changes for Orange G upon illumination in the presence of the photocatalysts are provided in **Figures 4.5 A** and **B.** The maximum absorption peak at 478 nm gradually decreases in intensity with

increased irradiation time, and this demonstrates that there is a decrease in the concentration of Orange G. It was observed that in the absence of the photocatalysts, there was no significant decrease in the Orange G peak under a series of similar irradiations.

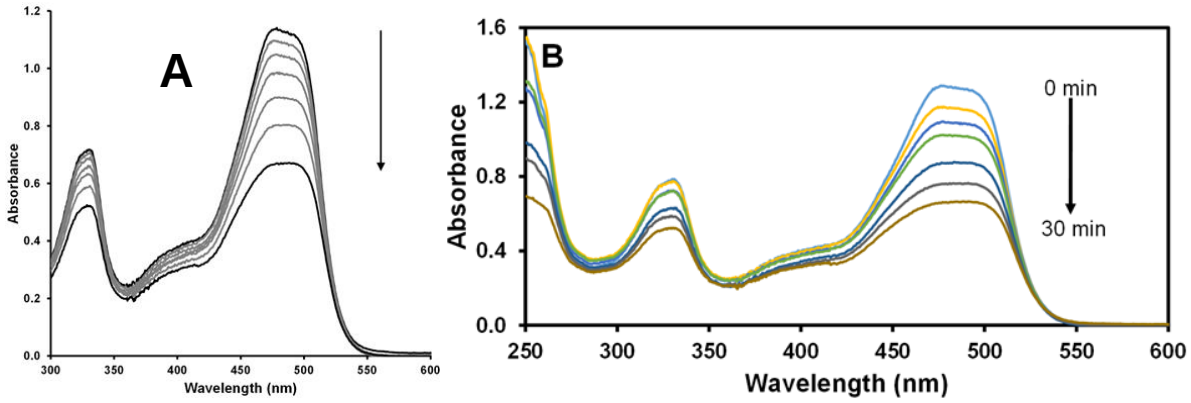

Figure 4.5. UV-visible absorption changes during the photocatalysis of Orange G through the irradiation with 20 mg of BODIPY **2a**/PS (A) and BODIPY **4**/PS (B) nanofibres at pH 6.7 with 530 and 660 nm Thorlabs LEDs, respectively.

Attempted photolysis with electrospun polystyrene in the absence of embedded BODIPYs **2a** and **4** as photocatalysts using visible region light had no effect on the Orange G photodegradation. This demonstrates that the degradation of Orange G is largely initiated by the ROS produced upon photoexcitation of the BODIPY dyes.

4.2.2. Reaction kinetics

Plots of Orange G concentration *vs* irradiation time are shown in **Figure 4.6**, and the kinetic information derived from these plots are presented in **Figure 4.7** and **Table 16**. The linearity of the plots of $\ln(C_o/C_t)$ *vs* irradiation time is an indication that the reaction followed the pseudo-first order kinetics. In all of the studies, it was observed that the rate (k_{obs}) of degradation of BODIPY **2a**/PS was larger than that of BODIPY **4**/PS under similar conditions **Table 14**. The half-life represents the time it takes for half the concentration of Orange G to be degraded. In this study, it was observed that as the half-life decreases with increasing Orange

G concentration, the reaction rate, initial reaction rate and percentage degradation increase (**Table 14**). **Figure 4.7A** provides the plot of initial rate *vs* concentration of Orange G, and **Figure 4.7B** shows the plot of the reciprocal of initial rate *vs* the reciprocal of Orange G concentration. Both plots indicate that there is an increase in the initial rate of degradation of Orange with increasing Orange G concentration, an indication of the efficiency of the photocatalysts in the degradation of the pollutants.

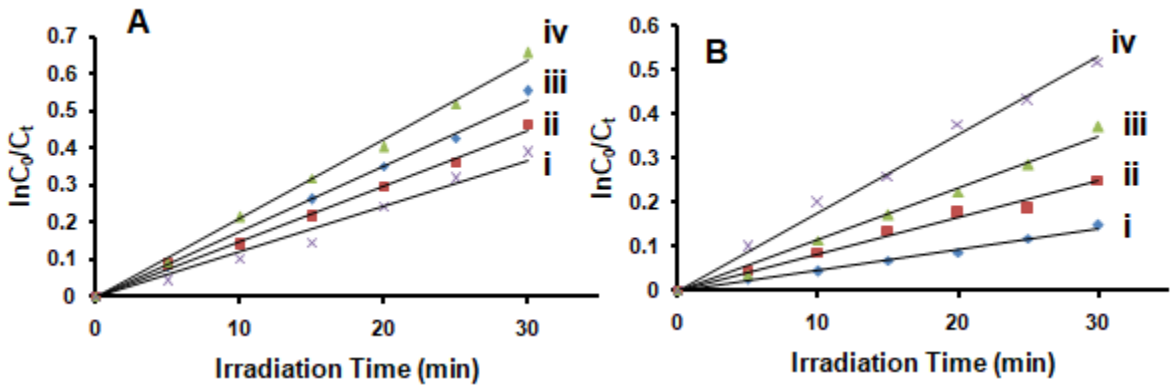

Figure 4.6. First-order kinetics plots for the photodegradation of Orange G using BODIPY **4**/PS (A) and BODIPY **2a**/PS (B) as photocatalysts at pH 6.7.

Since these effluents from the textile industry are discharged into the environment at varying pH ranges, the efficiency of the photocatalysts was investigated under different pH conditions. The photodegradation of Orange G is known to be greatly influenced by the pH of the aqueous media [124]. The properties of BODIPY **2a**/PS was examined to provide an example in this context. Degradation studies were conducted at pH 3.0, 4.0, 6.7, 10.0 and 11.0 using the photocatalysts. A plot of percentage degradation against pH (**Figure 4.8**) shows that the dye degrades more quickly at basic pH than at acidic pH over the same time intervals with the rate of degradation reaching a maximum at pH 6.7.

Table 14 A. Photodegradation kinetics data for the BODIPY **2a**/PS nanofibres.

[OG] ($\times 10^{-5}$ mol.L^{-1})	Initial rate (r_0) ($\times 10^{-7}$ mol.L^{-1}.min^{-1})	Half-life ($\tau_{½}$) (min)	Degradation (η) (% at 30 min)	k_{obs} ($\times 10^{-3}$ min^{-1})
4.1	1.86	123.8	14.9	5.6
6.4	7.30	59.2	32.7	11.7
9.3	14.3	43.6	38.6	15.9
11.8	29.8	27.5	54.8	25.2

Table 14 B. Photodegradation kinetics data for the BODIPY **4**/PS nanofibres.

[OG] ($\times 10^{-5}$ mol.L^{-1})	Initial rate (r_0) ($\times 10^{-7}$ mol.L^{-1}. min^{-1})	Half-life ($\tau_{½}$) (min)	Degradation (η) (% at 30 min)	K_{obs} $\times 10^{-2}$ min^{-1}
3.5	4.3	57.8	32.0	1.2
3.9	6.0	49.5	37.2	1.5
35.6	10.2	40.8	42.6	1.8
7.3	15.8	33.0	48.1	2.1

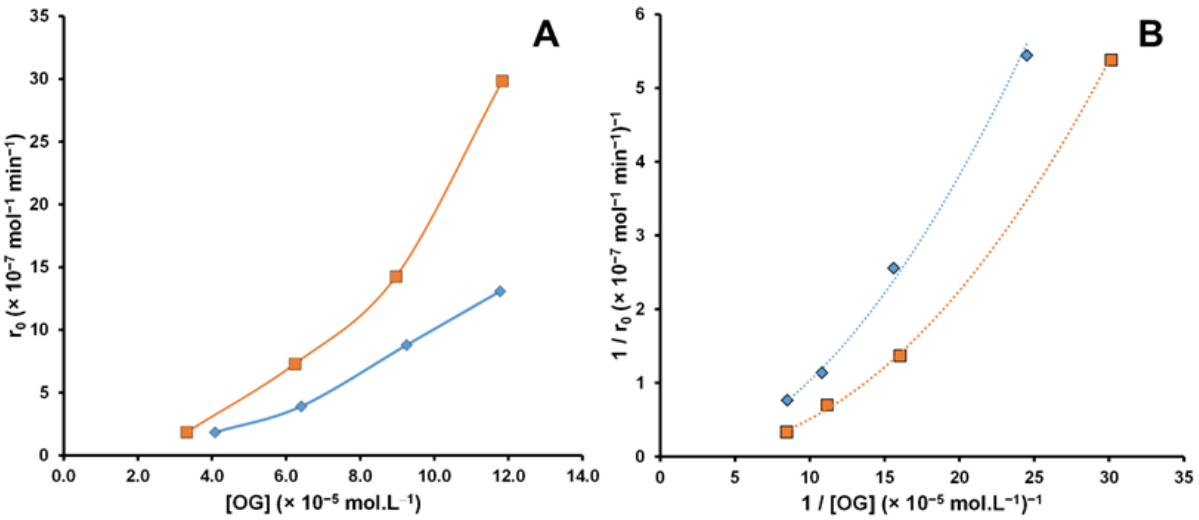

Figure 4.7. The rate of photodegradation of Orange G *vs* initial concentration during the initial use of BODIPY **2a**/PS nanofibres as catalysts in water (blue diamonds) and their subsequent reuse (orange squares).

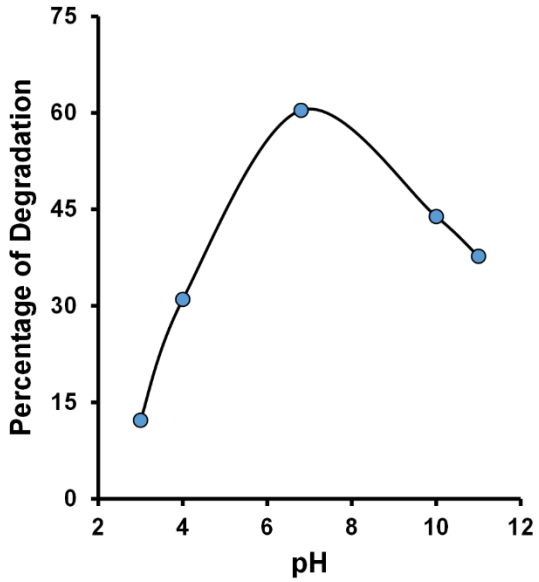

Figure 4.8. Effect of pH on the percentage degradation of Orange G (Orange G = 1.5×10^{-4} mol^{-1}.L, catalyst = 25 mg, Thorlabs LED = 530 nm, time of irradiation = 3 h).

The dependence of degradation efficiency on the initial dye concentration is of importance from an applications point of view [125]. **Table 14** shows the effect of initial Orange G concentration on the photocatalytic degradation at pH = 6.7. The studies show that in the presence of the photocatalysts, the reaction rates (k_{obs}) increases as the concentration of Orange G increases (**Table 14**). The results demonstrate that the number of photons absorbed by the catalysts was not dependent on initial dye concentration and that for all concentrations studied, an increase in the reaction rate was accompanied with shorter half-lives.

4.2.3. Catalyst stability and recyclability

The stability of the functionalised polymer fibre catalysts was examined with the degradation of Orange G using BODIPY **2a**/PS selected as an example (**Figure 4.9**). Prior to reuse, the catalyst was washed several times with water and dried at room temperature. The percentage dye photodegradation of Orange G after illumination of time t was calculated using **Equation 24**:

$$\% \text{ Photodegradation } (\eta) = (1 - C_t/C_0) \times 100 \quad \textbf{(24)}$$

where C_0 and C_t are the Orange G concentrations before and after illumination for time t. **Figure 4.9** shows that the photocatalytic efficacy of the catalyst remained relatively unchanged upon re-use, as evidenced by the lack of significant changes in the percentage of dye degradation (η). This provides confirmation of the stability and efficiency of BODIPY nanofibre complexes for the degradation of Orange G under visible light illumination and demonstrates that the catalyst can easily be separated for re-use.

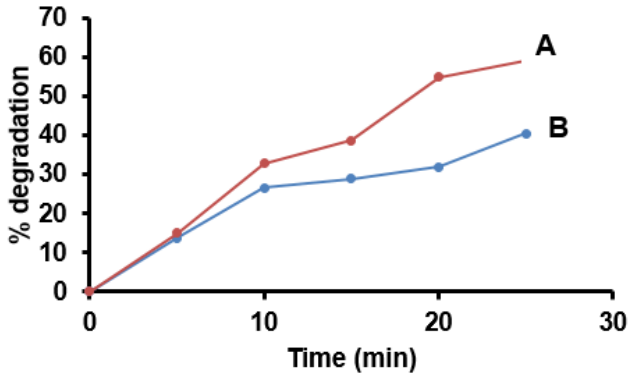

Figure 4.9. Percentage degradation of Orange G *vs* irradiation time, showing catalyst stability upon re-use (B) compared to the initial use (A).

4.3. Photocatalytic degradation of Methyl Orange

4.3.1. UV-visible absorption spectral changes

The photodegradation of Methyl Orange was also undertaken with the BODIPY **4**/PS nanofibres used as photocatalysts. Different concentrations of Methyl Orange were irradiated at 5 min intervals at pH 6.7, and the spectral changes were monitored at 470 nm. The UV-visible absorption spectrum of Methyl Orange (**Figure 4.10**) has two major absorption bands, an n-π* band at 470 nm that arises from the conjugated structure of the azo bond [125] and a band at 273 nm that can be attributed to the aromatic rings of the dye molecule (**Figure 4.10**). During photocatalysis, there was a significant decrease in the intensity of both absorption bands, with the observed change at 470 nm providing direct spectroscopic evidence that the

dye is being degraded by breaking the azo bond. Different concentrations of Methyl Orange were irradiated for 30 min at 5 min time intervals, and the spectral changes were monitored at 470 nm. In the absence of the photocatalyst, there were no changes in the absorption band of Methyl Orange. This implies that the degradation is initiated by the reaction with reactive oxygen species generated upon illumination of the BODIPY **6**/PS nanofibres.

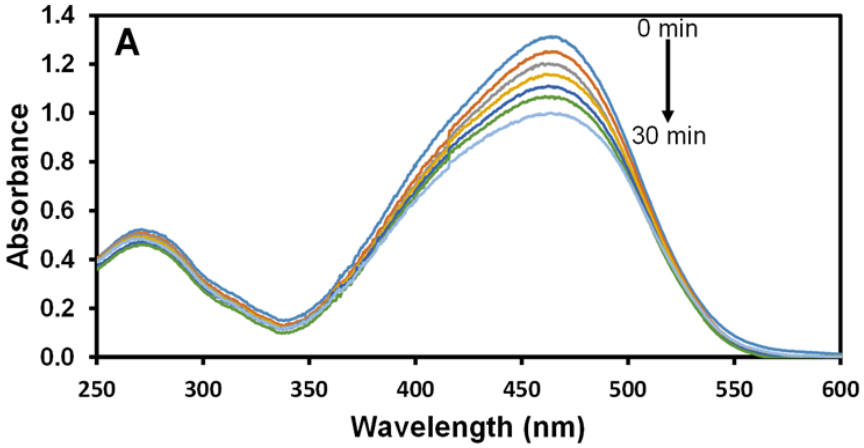

Figure 4.10. UV-visible absorption changes measured at 5 min intervals during the photocatalysis of Methyl Orange with a 660 nm LED, using 20 mg of BODIPY **6**/PS nanofibres at pH 6.7.

4.3.2. Reaction kinetics

The photocatalytic kinetics of the immobilised photocatalyst was investigated at different concentrations of Methyl Orange and in a similar manner to the Orange G experiments, linear plots of ln (C_0/C_t) *vs* time were obtained, indicating that there is pseudo-first order kinetics for the photodegradation reactions of the immobilised catalyst (**Figure. 4.11**). These values were consistent with the Orange G experiments described above [123]. The reaction rate, initial rate, and half-lives were determined from these plots and tabulated in **Table 15**. From these results, an increase in the rate of photodegradation (k_{obs}) of Methyl Orange with increasing concentration can be observed. In a similar manner to what was observed during the

degradation of Orange G, the half-life of degradation was observed to decrease with increasing Methyl Orange concentration, initial rate, percentage degradation, and reaction rate.

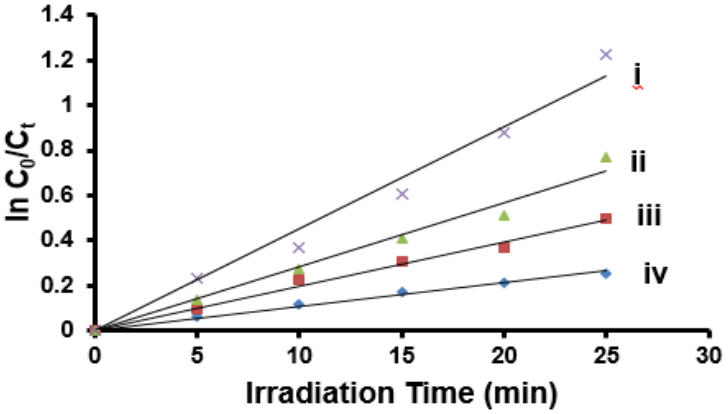

Figure 4.11. First-order kinetics plots for the photodegradation of Methyl Orange at different concentrations with BODIPY **4**/PS. Studies were carried out in water at pH = 6.7.

Table 15. Photodegradation kinetics data for the photodegradation of Methyl Orange using BODIPY **4**/PS nanofibres.

[MO] ($\times 10^{-4}$ mol.L^{-1})	Initial rate (r_0) ($\times 10^{-6}$ mol.L^{-1}.min^{-1})	Half-life ($\tau_{½}$) (min)	Degradation (η) (% at 30 min)	k_{obs} ($\times 10^{-3}$ min^{-1})
9.0	1.8	347	6.0	2.0
11.1	4.1	187	10.3	3.7
14.5	7.6	133	14.1	5.2
17.5	15.6	77.9	24.3	8.9

MO = Methyl Orange, values in brackets were obtained in water using ADMA.

4.4. Concluding remarks

This chapter examined the photocatalytic degradation of Orange G and Methyl Orange, which are azo dyes that are present in the environment as pollutants from the textile industry. Electrospun polystyrene fibres functionalised with BODIPY dyes were used to photodegrade of Orange G. At the highest concentrations of the pollutant, BODIPY **2a**/PS gave a higher

value for percentage degradation than BODIPY **4**/PS (**Table 14**). This is due to the higher singlet oxygen quantum yield generated by BODIPY **2a**/PS with respect to BODIPY **4**/PS, because of the enhanced π-π interaction between polystyrene and BODIPY **2a** which possesses a pyrene ring at the *meso*-position. It was also observed that the percentage of degradation is pH-dependent. The photocatalysts did not show significant differences in percentage degradation value upon re-use. The kinetics studies demonstrate that the photodegradation followed the pseudo-first order kinetics with reaction rates and initial rates increasing with concentration resulting in decreasing half-life values.

CHAPTER 5

5. BODIPY CONJUGATES OF MAGNETIC NANOPARTICLES

5.1. Magnetic nanoparticles and their BODIPY conjugates.

Cobalt ferrite nanocomposites are known to enhance the generation of singlet oxygen quantum yield of photosensitiser dyes when the dye is conjugated to the nanoparticle. Magnetic nanocomposites enhance intersystem crossing to the triplet state through an external heavy atom effect, and this should result in enhanced singlet oxygen generation by the BODIPY dye. This chapter describes the synthesis of magnetic nanocomposites, and their conjugation to BODIPY dyes, along with their characterisation and a preliminary examination of their photophysical properties.

5.2. Synthesis of intermediate BODIPY 2f from 2c

The reduction of the 4-aminophenyl group of BODIPY **2c** to form 4-aminophenylBODIPY **2f** for the purpose of conjugation to MNPs through amide bonds was achieved. FT-IR spectroscopy was used to confirm the conversion of the NO_2 group, which is associated with the peak at 3493 cm^{-1} (**Figure 5.1**). MALDI-TOF mass spectrometry also provided molecular ion peaks consistent with the target BODIPY compound.

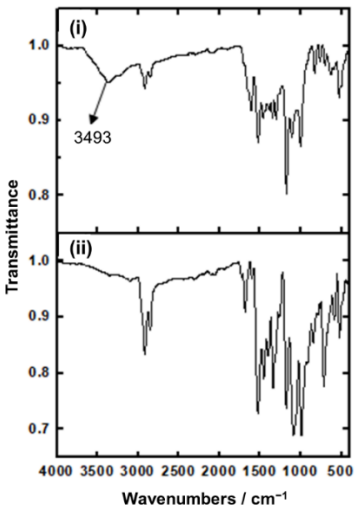

Figure 5.1. FT-IR spectra of BODIPYs **2c** (i) and **2f** (ii), highlighting the appearance of the 4-aminophenyl group after reduction of the 4-aminophenyl group.

5.3. Hydrolysis of BODIPY 2e to give intermediate 2g

BODIPY **(2g):** 4,4′-Difluoro-8-(4-carboxyphenyl)-1,3,5,7-tetramethyl-2,6-dibromo-4-bora-3a,4a-diaza-*s*-indacene. The hydrolysis of BODIPY **2e** was achieved under basic conditions to prevent the decomplexation of the BF_2 moiety (**Scheme 17**), and the presence of the BODIPY **2g** was confirmed prior to conjugation to MNPs through the formation of amide bonds. FT-IR spectroscopy was used to confirm the conversion of the ester group to a carboxylic acid based on the appearance of an OH carboxylic acid peak at 3151 cm^{-1} and the C=O carboxylic acid peak at 1694 cm^{-1} (**Figure 5.2**).

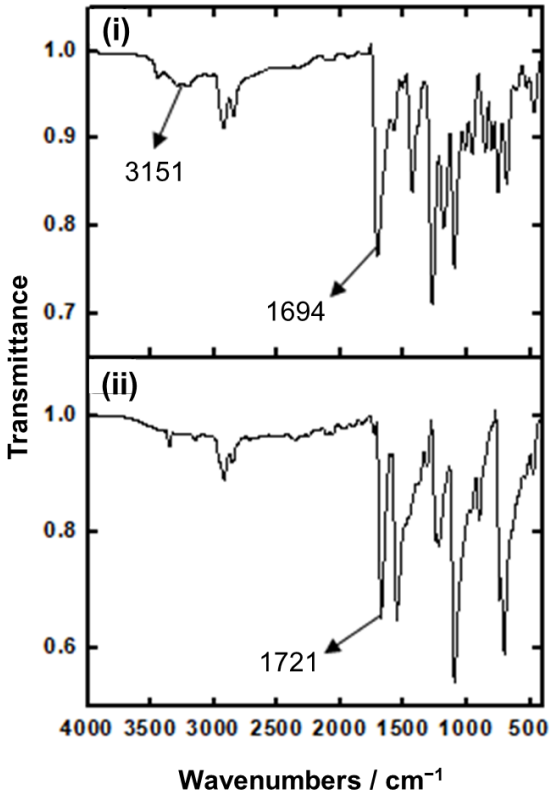

Figure 5.2. FT-IR spectrum of BODIPYs **2e** (ii) and **2g** (i), highlighting the appearance of the 4-carboxyphenyl group at 3151 cm^{-1} after hydrolysis.

5.4. Synthesis of $CoFe_2O_4$ MNPs

The synthesis of two different substituted $CoFe_2O_4$ MNPs is reported in this study; $CoFe_2O_4$-NH_2 MNPs (**Scheme 20**) and $CoFe_2O_4$-COOH MNPs. The functionalisation of $CoFe_2O_4$-NH_2 using succinic anhydride yielded $CoFe_2O_4$-COOH MNPs (**Scheme 20**)**.** The synthesis of both MNP conjugates followed a previously reported conventional co-precipitation method [49,50].

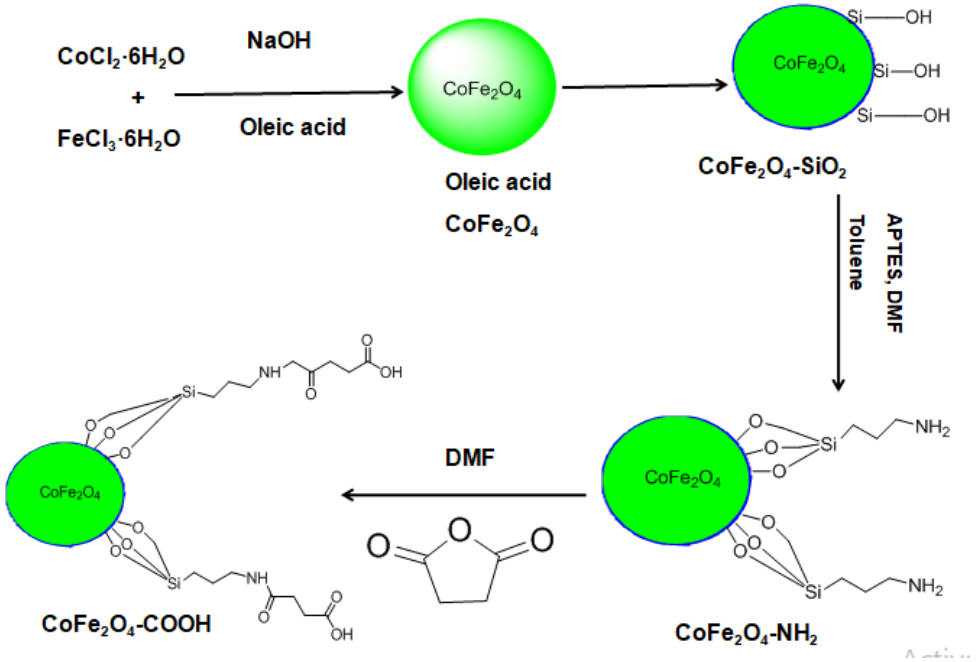

Scheme 20. Synthesis of $CoFe_2O_4$-NH_2 and $CoFe_2O_4$-COOH MNPs.

5.5. Conjugation of BODIPY dyes to the $CoFe_2O_4$ MNPs.

The linking of the $CoFe_2O_4$-NH_2 MNPs to the BODIPY complexes was achieved through the carboxylic acid functional group on the BODIPY. Prior to linking, the carboxylic functional groups of **2f** and **3** were activated with DCC/NHS to form conjugates **2f**-$CoFe_2O_4$ and **3**-$CoFe_2O_4$, respectively (**Scheme 21**).

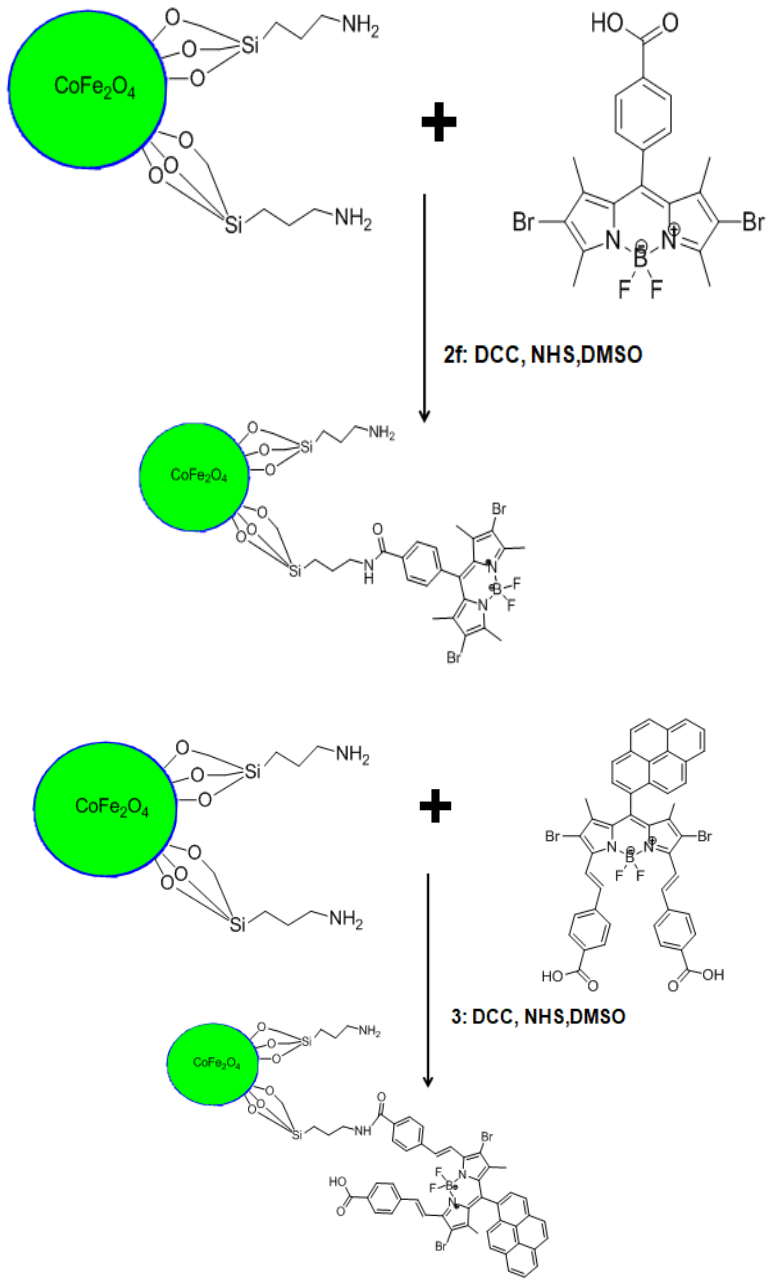

Scheme 21. Conjugation of complexes **2f** and **3** to $CoFe_2O_4$-NH_2 MNPs.

The carboxylic group on the $CoFe_2O_4$-COOH MNPs were activated with DCC prior to conjugation, followed by the formation of an amide bond with complex **2g** to form **2g**-$CoFe_2O_4$-COOH (**Scheme 22**).

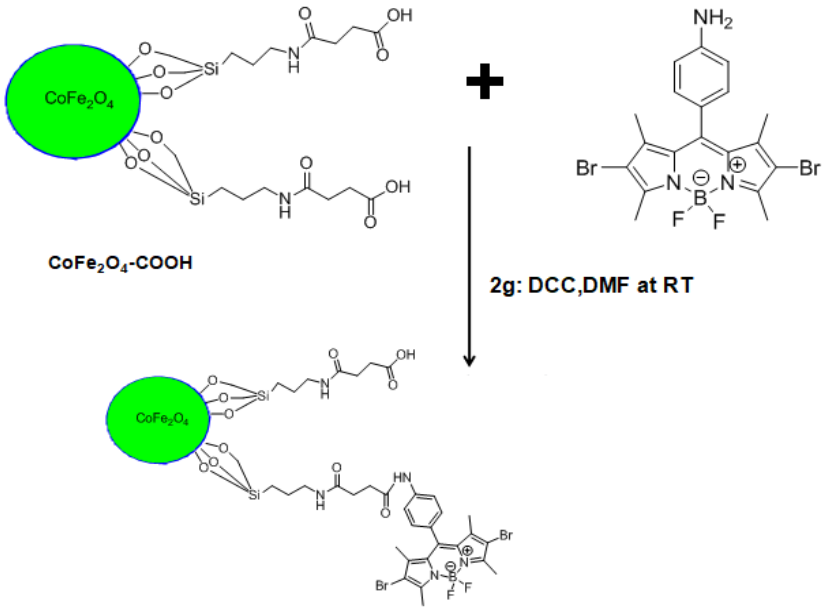

Scheme 22. Conjugation of complex **2g** to $CoFe_2O_4$-COOH MNPs.

5.6 Characterisation of the complexes

Characterisation techniques used to confirm the synthesis of $CoFe_2O_4$ MNPs and BODIPY-$CoFe_2O_4$ MNP conjugates include X-ray diffraction, FT-IR spectroscopy, Energy dispersive X-ray spectroscopy (EDS), and Transmission electron microscopy (TEM).

5.6.1. X-ray Diffraction (XRD)

The XRD patterns of the BODIPYs, $CoFe_2O_4$ MNPs, and their corresponding conjugates were analysed and compared (**Figure 5.3**), using $CoFe_2O_4$-NH_2 MNPs and complex **3** as an example. Characteristics peaks attributed to a cubic spinel structure was observed for $CoFe_2O_4$-NH_2 with peaks at 2Θ = 30, 54, 57 and 63º which corresponds to hkl Miller indices of (220), (511), and (440), respectively. These characteristic peaks agree with values that have been previously reported [126]. The presence of peaks in **3**-$CoFe_2O_4$-NH_2 corresponding to both complex **3** and $CoFe_2O_4$-NH_2 is an indication that the conjugate is a composite of the two photocatalysts and that the $CoFe_2O_4$-NH_2 MNPs retains their crystalline nature when conjugated to BODIPYs. Similar diffraction patterns were obtained for the other BODIPYs and their MNP conjugates,

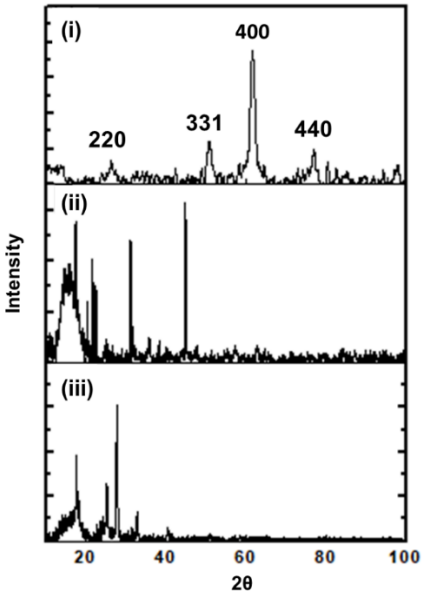

Figure 5.3. XRD diffractograms of (i) $CoFe_2O_4$-NH_2, (ii) **3**-$CoFe_2O_4$-NH_2 and (iii) BODIPY **3**.

and it was also observed that upon amide bond formation, the peaks of the XRD shifted slightly. Crystalline size determination was carried out using the XRD data to determine the sizes of the MNPs and BODIPY-MNP conjugate for comparison using the Debye-Scherrer (**Equation 25**) [66]:

$$d = \frac{k\lambda}{\beta \cos\theta} \qquad (25)$$

where *k* is an empirical constant equal to 0.9, λ is the wavelength of the X-ray source, (1.5405 Å), β is the full width at maximum diffraction peak, and θ denotes the angular position of the peak. The sizes of the MNPs and respective conjugates are listed in **Table 16**.

Table 16. Sizes of the complexes determined from TEM and XRD data.

	TEM (nm)	**XRD (nm)**
$CoFe_2O_4$-NH_2	9.98	11.14
$CoFe_2O_4$-COOH	11.76	12.35
2f-$CoFe_2O_4$-NH_2	12.52	15.20
2g-$CoFe_2O_4$-COOH	13.45	16.89
3-$CoFe_2O_4$-NH_2	15.78	16.41

5.6.2. Fourier transfer infrared spectroscopy (FT-IR)

The formation of a covalent bond between the BODIPYs and the MNPs was investigated using FT-IR with the following complexes used to provide an example ($CoFe_2O_4$-NH_2, BODIPY **3,** **3**-$CoFe_2O_4$-NH_2). The characteristic peak for the N-H bend of a primary amine (-NH_2) group is observed in the $CoFe_2O_4$-NH_2 spectrum at 1640 cm^{-1} (**Figure 5.4**). In the BODIPY **3** spectrum, a C=O vibration at 1694 cm^{-1} and a broadened peak from 3100 to 3400 cm^{-1} can be attributed to the -OH group of the carboxyl moiety (**Figure 5.4**). In the **3**-$CoFe_2O_4$-NH_2 conjugate spectrum (**Figure 5.4**), the amide bond peaks at 1566 and 1624 cm^{-1} and an N-H primary amine stretch peak at 3322 cm^{-1}, provide an indication of covalent bond formation between $CoFe_2O_4$-NH_2 and BODIPY **3.**

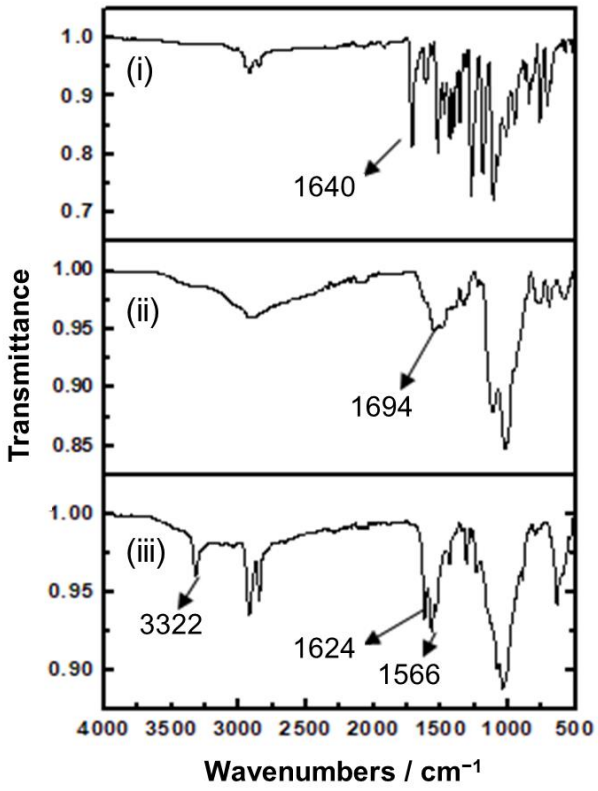

Figure 5.4. FT-IR spectra of (i) $CoFe_2O_4$-NH_2, (ii) BODIPY **3** and (iii) **3**-$CoFe_2O_4$-NH_2 conjugate.

5.6.3. Energy Dispersive X-ray Spectroscopy

The elemental composition of the $CoFe_2O_4$-NH_2 MNPS and their respective BODIPY-MNP conjugates were studied by energy dispersive X-ray spectroscopy. BODIPY **3** and **3**-$CoFe_2O_4$-NH_2 are used as examples in this regard. For BODIPY **3,** the expected elements were obtained (**Figure 5.5A**). Since the elemental compositions for $CoFe_2O_4$-NH_2 and $CoFe_2O_4$-COOH are the same, the spectrum of $CoFe_2O_4$-NH_2 MNPs is shown as an example (**Figure 5.5B**). In the spectrum for the conjugate (**Figure 5.5C**), the expected peaks for the MNPs were observed along with additional peaks (Br, F, B) that are only present in the presence of BODIPY dyes. This provides an indication that the conjugates are composites of the BODIPY dyes and $CoFe_2O_4$-NH_2 MNPs. Similar results were observed for other BODIPY dyes and their MNP conjugates.

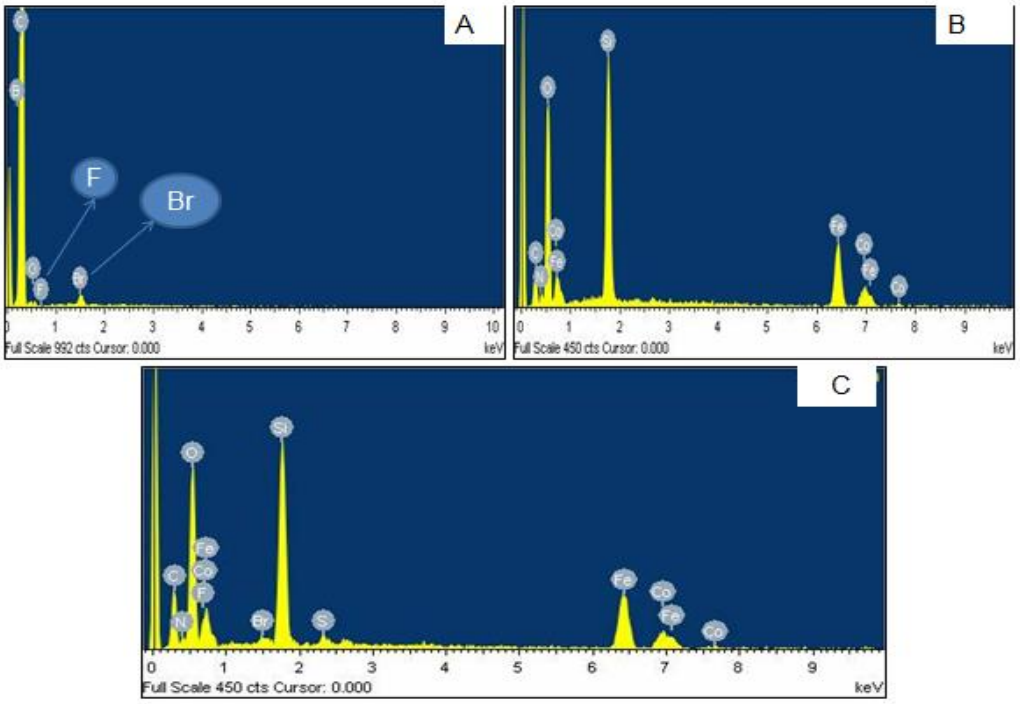

Figure 5.5. EDS spectra of (A) BODIPY **3**, (B) $CoFe_2O_4$-NH_2 MNPs and (C) **3**-$CoFe_2O_4$-NH_2.

5.6.4. Transmission Electron Microscopy (TEM)

TEM analyses were conducted yo determine the size, morphology, and dispersion of the $CoFe_2O_4$-NH_2 MNPs and their BODIPY-MNP conjugates. Using $CoFe_2O_4$-NH_2 and **3**-$CoFe_2O_4$-NH_2 for illustration, as shown in (**Figure 5.6**), the TEM images show that the MNPs are aggregated; this can be attributed to their superparamagnetic nature. The enhanced aggregation observed from the TEM images of **3**-$CoFe_2O_4$-NH_2 can be attributed to π-π interactions between the BODIPY dyes on neighbouring MNPs. The TEM images reveal that both the MNPs and their conjugates are mostly spherical in shape with average sizes of 10.0 and 15.8 nm for $CoFe_2O_4$-NH_2 and **3**-$CoFe_2O_4$-NH_2, respectively (**Figure 5.6** and **Table 16**). The results show that upon conjugation to BODIPY dyes, the size and morphology of the MNPs changes significantly.

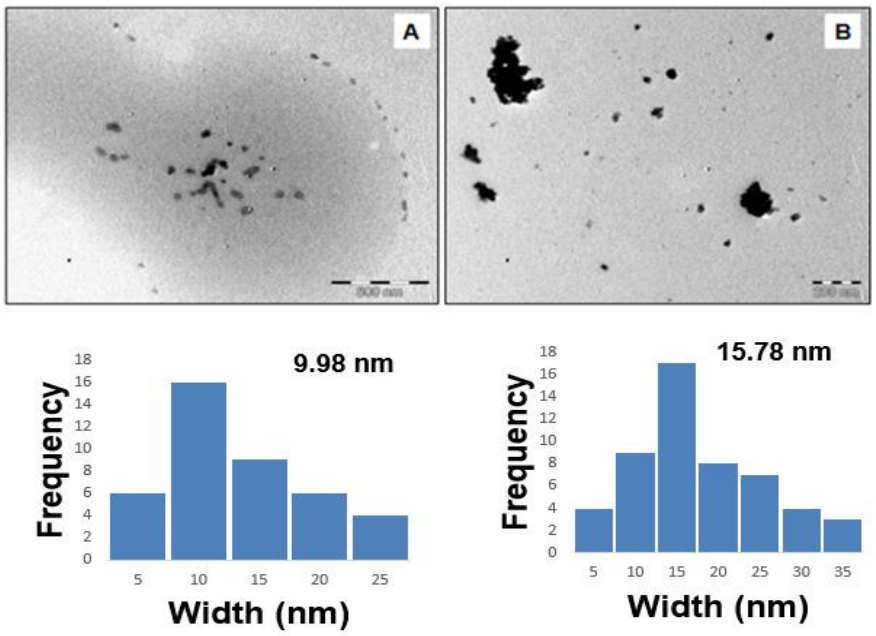

Figure 5.6. TEM images of (A) $CoFe_2O_4$-NH_2 MNPs, and (B) **3**-$CoFe_2O_4$-NH_2, and histograms showing the size distributions.

5.6.5. X-ray Photoelectron Spectroscopy

The surface chemistry and functionalisation of the $CoFe_2O_4$-NH_2 MNPs were analysed using X-ray photoelectron spectroscopy (XPS). The wide scan XPS conducted showed that the BODIPY complexes, $CoFe_2O_4$-NH_2 MNPs, and BODIPY-MNP conjugates possess the anticipated elemental compositions. The $CoFe_2O_4$-NH_2 MNPs, BODIPY **3** and **3**-$CoFe_2O_4$-NH_2 series will be used as an example (**Figure 5.7**). The survey spectra contained all the expected elements for the $CoFe_2O_4$-NH_2 MNPs, due to the presence of the O_{1s}, C_{1s}, N_{1s}, and Si_{1s} peaks. All the expected elements were observed in the BODIPY **3** and **3**-$CoFe_2O_4$-NH_2 samples with the **3**-$CoFe_2O_4$-NH_2 containing additional elements that can be attributed to both the BODIPY dyes and the MNPs. This provides further confirmation that **3**-$CoFe_2O_4$-NH_2 is a composite of $CoFe_2O_4$-NH_2 MNPs and BODIPY **3.**

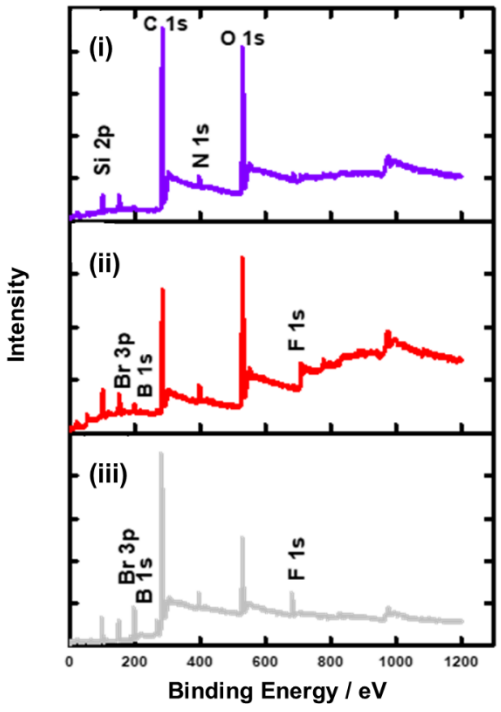

Figure 5.7. XPS survey spectra of (i) the $CoFe_2O_4$-NH_2 MNPs, (ii) the **3**-$CoFe_2O_4$-NH_2 conjugate and (iii) BODIPY **3**.

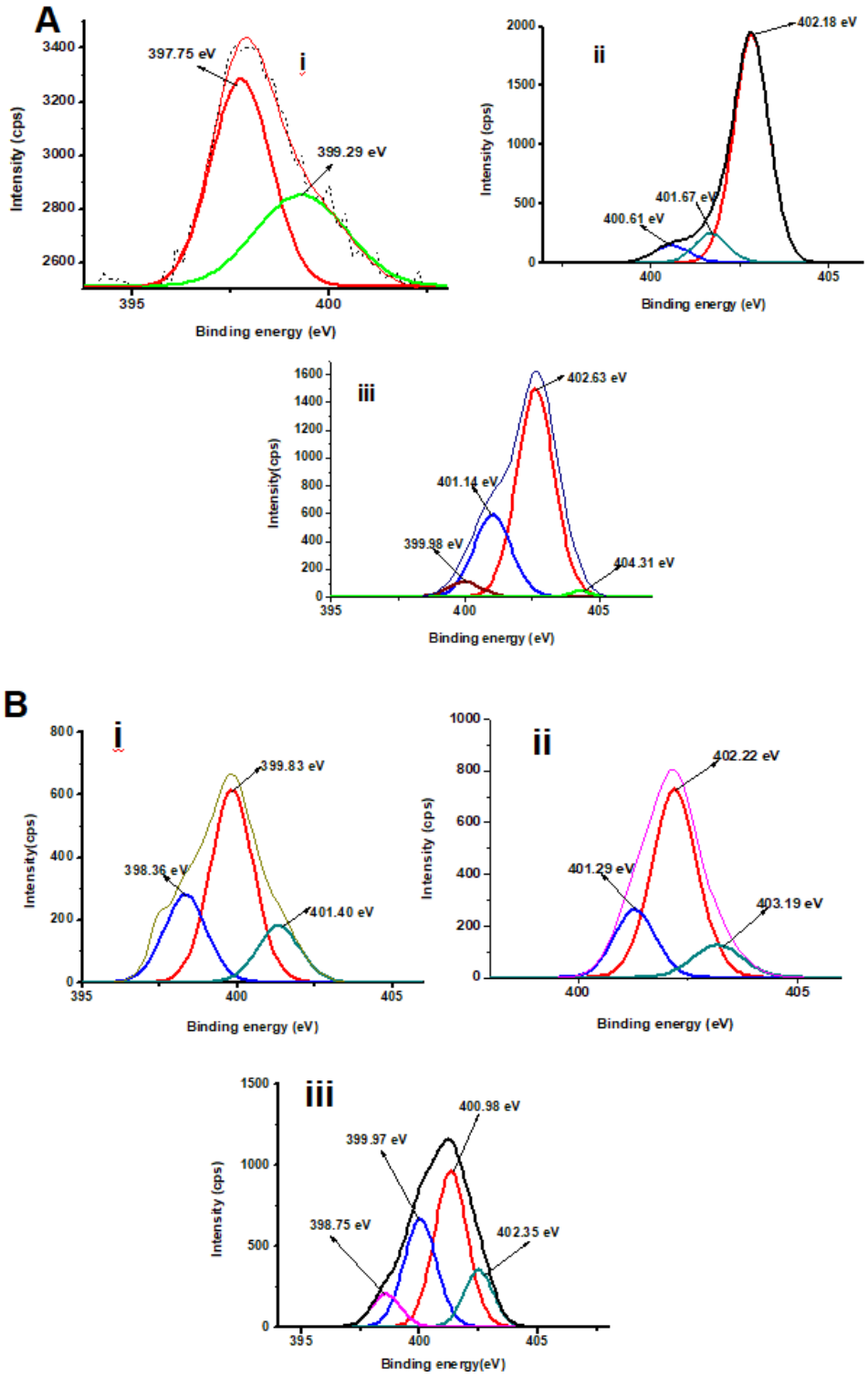

Figure 5.8. High-resolution XPS (N_{1s}) spectra for (A) (i) $CoFe_2O_4$-NH_2 MNPs, (ii) **2g**, (iii) **2g**-$CoFe_2O_4$-NH_2 MNPs and (B) (i) $CoFe_2O_4$-COOH MNPs (ii), **2f** and (iii) **2f**-$CoFe_2O_4$-COOH MNPs.

In order to determine the efficacy of the functionalisation of the MNPs, high-resolution XPS analysis was undertaken. The N_{1s} peak for the $CoFe_2O_4$-NH_2 MNPs was deconvoluted to give two components at 397.75 eV (N-C) and 399.29 eV (N-H) (**Figure 5.8A**). On the other hand, deconvolution of the N_{1s} high-resolution peak for **2g** gave three components at 400.61, 401.67 and 402.18 eV, which can be attributed to the C=N, C-N and N-H bands, respectively (**Figure 5.8A**). High-resolution XPS analysis was undertaken to provide evidence for the amide bond linkage between **2g** and $CoFe_2O_4$-NH_2 to form **2g**-$CoFe_2O_4$-NH_2 (**Figure 5.8A**). In this regard, the high-resolution N_{1s} peak was deconvoluted to give four components at 399.98, 401.14, 402.63 and 404.31 eV, which can be attributed to (N=C), (N), (N-C) and (N-C=O), respectively. The presence of the high binding energy component at 404.31 eV, in the **2g**-$CoFe_2O_4$-NH_2 spectrum, is an indication of bond formation between **2g** and $CoFe_2O_4$-NH_2MNPs, since it is absent in the $CoFe_2O_4$-NH_2 and **2g** (**Figure 5.8A**) spectra.

In **Figure 5.8B**, the high-resolution N_{1s} peak for $CoFe_2O_4$-COOH MNPs was deconvoluted to give three components at 398.36, 399.83 and 401.40 eV, which correspond to the (N-C), (N-H) and (N-C=O) bonds, respectively. The appearance of the 401.40 eV components at high binding energy is due to amide bond formation between $CoFe_2O_4$-NH_2 MNPs and succinic anhydride. This band is absent in the spectrum of $CoFe_2O_4$-NH_2 MNPs alone. This confirms the efficient functionalisation of $CoFe_2O_4$-NH_2 MNPs to form the $CoFe_2O_4$-COOH MNPs. The deconvolution of the N_{1s} high-resolution peak for BODIPY-NH_2 (**Figure 5.8B**), also yielded three components at 401.29, 402.22 and 403.19 eV, corresponding to the C-N, C=N and N-H bonds, respectively. Finally, the high-resolution N_{1s} peak for **2f**-$CoFe_2O_4$-COOH MNPs was deconvoluted, and four components are observed at 398.75, 399.97, 400.98 and 402.35 eV due to the (N=C), (N-C) and (N-C=O) nitrogen atoms, respectively (**Figure 5.8B**). A significant increase in the relative intensity of the higher binding energy component at 402.35 eV provides

an indication of an increase in the percentage of amide bonds in the conjugate and hence that $CoFe_2O_4$-COOHMNPs and **2f** were covalently linked through the formation of an amide bond.

5.7. Singlet oxygen generation properties of the conjugates

The singlet oxygen quantum yield of complex **3**-$CoFe_2O_4$ was used as an example to investigate the ability of heavy atoms such as the magnetic nanoparticles to enhance singlet oxygen generating proficiency of photosensitisers. DPBF was used as a singlet oxygen scavenger, and the singlet oxygen quantum yield of complex **3**-$CoFe_2O_4$ increased to 0.40 with respect to that of BODIPY **3** alone which was found to be 0.32 (**Figure 5.9**). This demonstrates that these MNP conjugates merit further in-depth investigation in the context of applications such as the photocatalytic degradation of azo dyes.

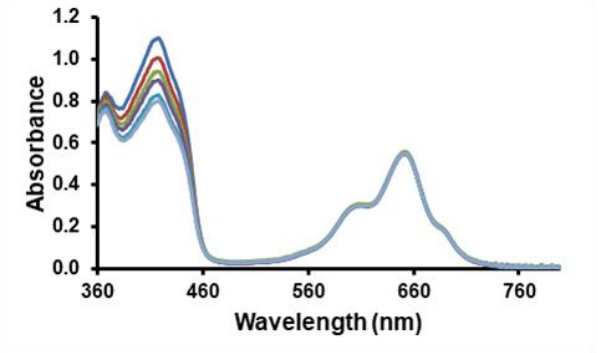

Figure 5.9. Photocatalytic degradation of DPBF (λ_{max} = 410 nm) in EtOH by complex **3**-$CoFe_2O_4$ (λ_{max} = 660 nm) at 10 s. The Φ_Δ value was determined using the comparative method with ZnPc in DMSO as the standard.

5.8. Concluding remarks

In this chapter, successful conjugation of BODIPYs **2f**, **2g** and **3** with cobalt-ferrite MNPs was described. BODIPYs **2f** and **3** have carboxylic acid functional groups that were conjugated to $CoFe_2O_4$-NH_2 through amide bond formation. In a similar way, BODIPY **2g** has amino

functional groups that form amide bonds with $CoFe_2O_4$-COOH. The conjugates were successfully characterised using the following techniques: XRD, FT-IR spectroscopy, TEM, EDS and XPS. The singlet oxygen generating proficiency of BODIPY **3** was enhanced upon conjugation to form **3**-$CoFe_2O_4$. This demonstrates that MNP conjugates of this type merit further in-depth study for use in applications.

CHAPTER 6

6. PHOTODYNAMIC ANTIMICROBIAL CHEMOTHERAPY (PACT)

This chapter discusses the results of the PACT studies using neutral brominated BODIPY dyes. To the best of our knowledge, this is the first example of a study of this type. The BODIPY complexes were effective when employed as singlet oxygen generating photosensitisers in the photoinactivation of *Staphylococcus aureus* (gram-positive bacteria), with negligible dark toxicity observed for all the BODIPY complexes studied. Similar studies were undertaken on *Escherichia coli* (gram-negative bacteria); the results showed that the drugs were not effective in photoinactivation of *Escherichia coli*. The different results obtained from the studies of *Escherichia coli* and *Staphylococcus aureus* can be attributed to the differences in the cell wall structures of gram-positive and gram-negative bacteria strains.

6.1. PACT Studies of *Escherichia coli* and *Staphylococcus aureus* in solution

Photodynamic antimicrobial studies were undertaken in 0.2% DMF solutions, because the BODIPY dye complexes (**2a**, **3** and **5**) used in this study were insoluble in PBS, but exhibited solubility in the presence of 0.2% DMF after sonication. In each case, 0.75 μg/mL of the complexes were used. It is known that bacteria such as *Staphylococcus aureus* are resistant to DMF [127]. The ability of the microbial species to survive was tested in PBS with 0.2% DMF (in the absence of BODIPY dyes) (control in **Figure 6.1**). The plots show that the media has a negligible impact on the overall results. Studies were also undertaken to determine if the BODIPY complexes have the capability to inactivate the microorganisms without illumination, so the studies were carried out in the dark. The dark toxicity studies (**Figure 6.1**) confirm that the BODIPY complexes had no significant dark toxicity even at high concentrations, and indicate that the microbial inactivation was due solely to the production of cytotoxic oxygen species by the BODIPY complexes upon illumination. Similar dark toxicity studies were undertaken for *Escherichia coli* (**Figure 6.4**).

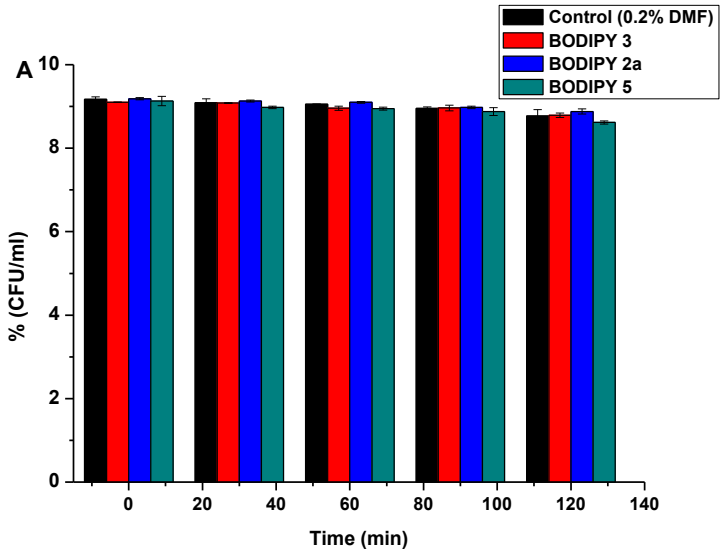

Figure 6.1. Dark toxicity studies in the presence of *Staphylococcus aureus* in 0.2% DMF in PBS for **2a**, **3** and **5**.

Brominated BODIPY complexes **2a**, **3** and **5** were found to be effective when employed as singlet oxygen generating photosensitisers in the photoinactivation of *Staphylococcus aureus* (**Figure 6.2**). BODIPY **3** proved to be the most effective. The log reduction values are relatively high for all of the complexes (**Table 17**); this can be attributed to the solubility exhibited by the BODIPY complexes in PBS with 0.2% DMF. Other factors that might have contributed to the high log reduction value obtained from this study are that BODIPY dyes are neutral (zwitterionic) molecules with relatively small size, and hence, they are favourable for cellular uptake. *Staphylococcus aureus* is a gram-positive bacteria with relatively porous cell walls as a result of the peptidoglycan layer having pore sizes of 9–10 nm and does not possess an extra polysaccharide layer above the peptidoglycan layer [128]. It is hence known that gram-positive bacteria can easily take up photosensitisers and can readily undergo photoinactivation [127, 129].

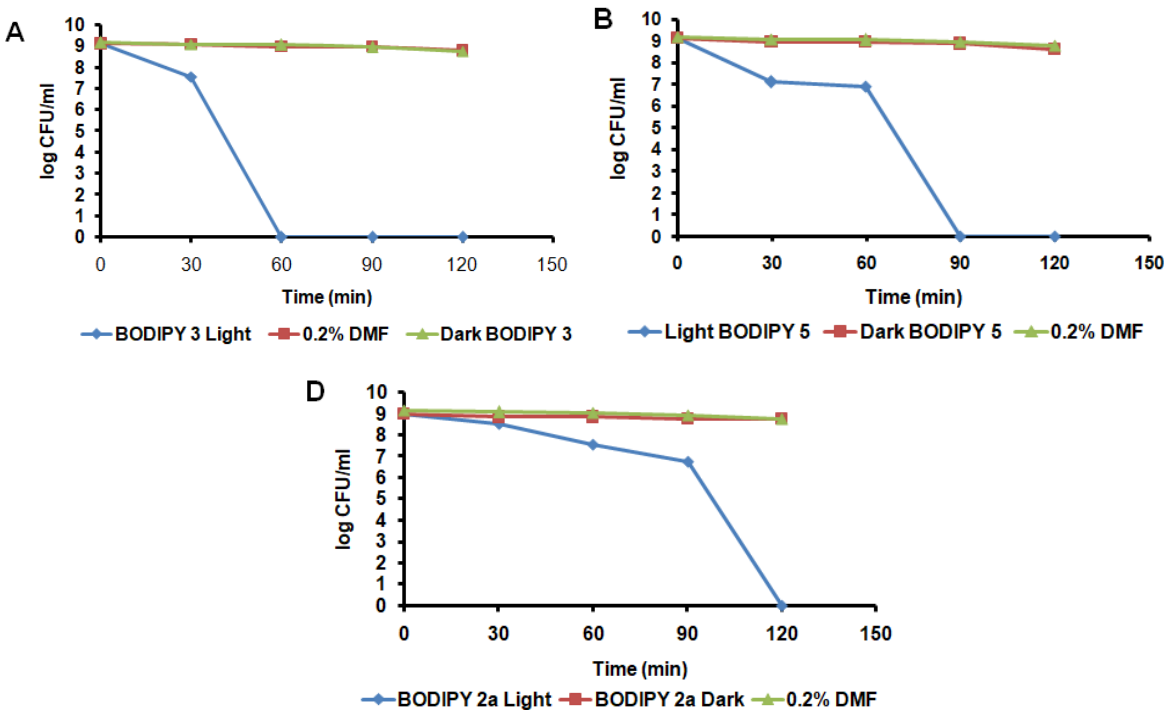

Figure 6.2. Survival curves of *Staphylococcus aureus* in solutions of (A) **3**, (B) **5** and (C) **2a**.

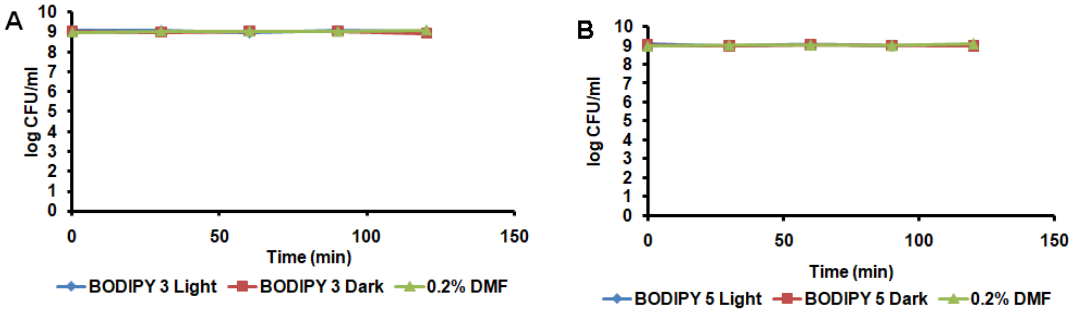

Figure 6.3. Survival curves of *Escherichia coli* in solutions of **3** (A) and **5** (B).

In contrast, *Escherichia coli* is a gram-negative bacteria which contains an extra outer membrane in the cell wall structure which envelopes the peptidoglycan layer. It is known that the outer membrane is vital to the physiology of gram-negative bacteria such as *Escherichia coli*, making them resistant to most antimicrobial treatment modalities [130]. The *Escherichia coli* outer membrane is a layer produced from porin proteins and lipopolysaccharides that can act both as an effective permeation barrier while allowing the efficient diffusion of nutrients. The outer membrane also makes the bacteria outer surface strongly hydrophobic, allowing

hydrophobic solutes to cross the outer membrane through the very narrow porin channels. Unlike in *Staphylococcus aureus* which has larger pores through the peptidoglycan layer and can allow relatively larger molecules to pass through, the narrow porin channels in *Escherichia coli* effectively act as a barrier to the passage of large or hydrophobic compounds [127].

Fluorometric studies have shown that the complexed outer membrane and cell wall of gram-negative bacteria shield the cytoplasmic membrane, hence preventing porphyrins and porphyrin-like molecules such as BODIPY dyes from binding to the membrane [131]. This renders gram-negative bacteria completely resistant to photoinactivation mediated by neutral BODIPY dye complexes. The very low log reduction values obtained from the photoinactivation studies on *Escherichia coli* (**Figure 6.3** and **Table 17**); as opposed to the high values obtained from studies undertaken on *Staphylococcus aureus* can be attributed to the aforementioned factors. The dark toxicity studies (**Figure 6.4**), again demonstrate that the BODIPY complexes exhibit no dark toxicity in this context.

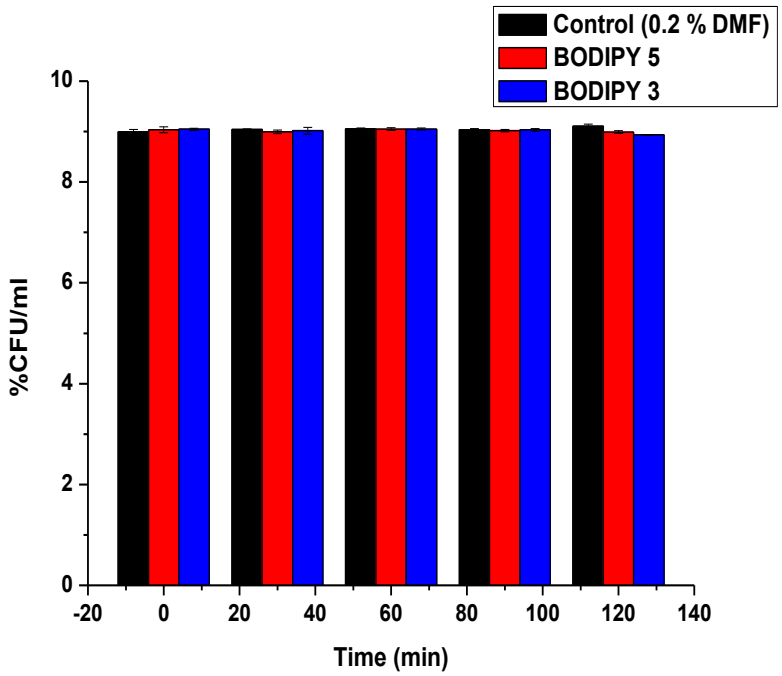

Figure 6.4: Dark toxicity studies in the presence of *Escherichia coli* in 0.2% DMF in PBS.

Table 17. Log reduction values in PBS (0.2% DMF) with standard deviations in brackets.

Micro-organism		**Log reduction**	**Φ_Δ**
S. aureus	**3**	9.18 (0.01)	0.32
	5	9.13 (0.03)	0.37
	2a	9.01 (0.05)	0.91
E. coli	**3**	0.04 (0.05)	0.32
	5	0.05 (0.02)	0.37

6.2. Concluding remarks

This chapter described the PACT activities of novel BODIPYs **3**, and **5** and the previously reported BODIPY **2a**. The studies were undertaken and completed for both *Escherichia coli* and *Staphylococcus aureus*. The results obtained from the studies in solution were analysed in terms of log reductions with BODIPY **3** being the most effective compound with a value of 9.18 for *Staphylococcus aureus*. In contrast, the log reduction results for *Escherichia coli* were very low (**Table 17**). This can be attributed to the differing cell wall physiology of *Escherichia coli*.

CHAPTER 7

7. OPTICAL LIMITING PROPERTIES OF BODIPY DYES

In this chapter, we report on the investigation of the efficacy of the 3,5-distyrylBODIPY dyes as optical limiters. BODIPY **3** (**Figure 7.1**) was investigated by open aperture Z-scan measurements (**Figure 7.2**). The nonlinear optical limiting parameters studied include the nonlinear absorption coefficient (β), the second-order hyperpolarisability (γ), the imaginary third-order susceptibility (Im[$\chi^{(3)}$]); and the optical limiting threshold (I_{lim}) (**Table 18**).

7.1. BODIPY dyes for NLO studies

Studies have demonstrated that molecules with extensive π-conjugated systems possess large electronic polarisabilities [80,81]. Conjugated molecules are hence expected to exhibit substantial second-order hyperpolarisability values [79,81,82]. Furthermore, it is known that molecules that possess donor and acceptor moieties that are separated by a π-conjugation system (D–π–A), exhibit large third-order susceptibility values [79,84]. In this work, BODIPY **3** (**Figure 7.1**) was investigated to evaluate its potential utility for optical limiting applications.

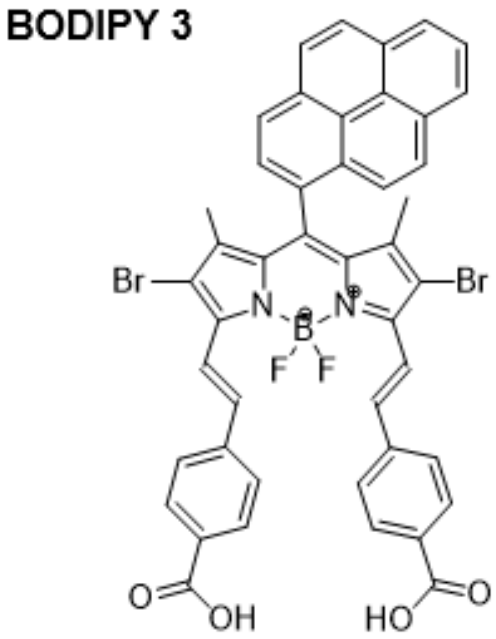

Figure 7.1.BODIPY dye used for the NLO studies.

The electron-donating pyrene group that is incorporated at the *meso*-position of BODIPY **3** is separated from the BODIPY core (acceptor) through a conjugated π-system. In this regard, the expectation was that these dyes should show enhanced third-order susceptibility values in a similar manner to what has been reported for other BODIPY dyes by Mack and coworkers [90-92,132-135]. Upon extension of the π-conjugation system via the addition of styryl groups at the 3,5-positions, the main spectral bands of the dyes are shifted to significantly longer wavelengths, hence resulting in relatively weak absorbance at 532 nm. BODIPY **3** contains bromine atoms at the 2,6-positions. In this regard, BODIPY **3** has the potential for utility as optical limiting materials in non-linear optical applications where the second harmonic of Nd/YAG lasers is concerned.

During the Z-scan measurements, consistent efforts were made to ensure the dyes studied did not aggregate in solution by checking the UV-visible absorption spectra before and after measurement, because aggregation could lead to significant NLS and hence interfere with the NLA results. In this study, the Z-scan setup used employs nanosecond rather than femtosecond laser pulses. The RSA responses obtained as the focal point is approached during the studies are hence not due to 2PA alone. The intrinsic β value cannot be measured; instead, the effective nonlinear absorption coefficient (β_{eff}) is derived because the ESA that occurs on a nanosecond timescale can also result in an RSA response [86].

7.2. Nonlinear optical parameters

A study of the nonlinear optical parameters was undertaken for novel BODIPY **3** in solution using an open aperture z-scan set-up. The studies were carried out in DMSO solution since its high boiling point limits differential temperature effects due to the intense incident laser pulses. The optical limiting parameters of BODIPY **3** are summarised in **Table 18**. Although the efficacy of an optical limiting material cannot be ascertained by one particular parameter in

isolation, the γ value is particularly important as it is independent of concentration and can therefore be used to provide a meaningful comparison of samples.

7.2.1. Nonlinear absorption coefficient (β)

The nonlinear absorption coefficient (β) is measured in order to determine the degree of nonlinear absorptivity of the optical limiting material. The laser wavelength used is 532 nm. Molecules whose linear absorption is zero at this wavelength can have an RSA response that is solely due to 2PA, but since that is not the case in this study linear absorption will populate the S_1 and hence the T_1 states after internal conversion. The z-scan plots for **3** are shown in **Figure 7.2**. Typical nonlinear absorption behaviour with RSA profiles were observed and the transmittance was decreased below 50% at the two different energies studied in DMSO (**Figure 7.2**). In order to determine the nonlinear absorption coefficient (β_{eff}) for each sample, the **Equations 7-22** described in Chapter 1 were applied. The results obtained are summarised in **Table 18**. The experimental β_{eff} values were found to be 1.62 and 1.70 × 10^{-7} mW^{-1} at input energies of 32 and 45 μJ, respectively. As anticipated, the transmittance is decreased when the input energy is increased. The magnitude of the β values for BODIPY **3** lie within the range of values previously reported for other organic compounds as being suitable for use in optical limiting applications [81].

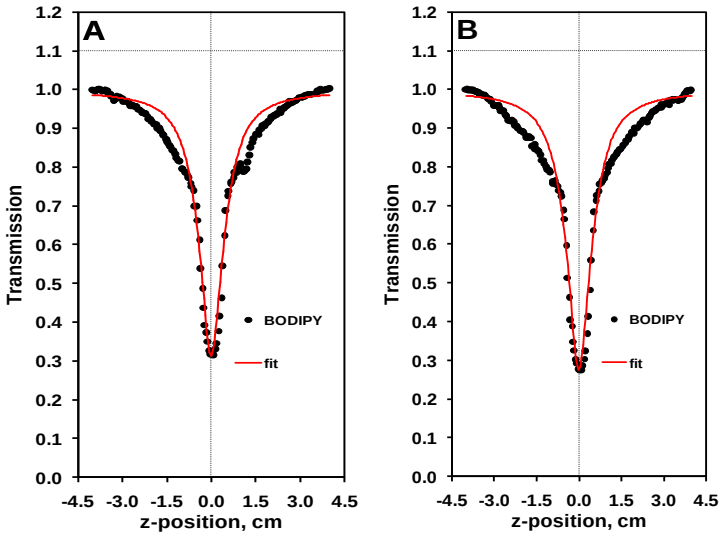

Figure 7.2. Characteristic open-aperture z-scans of BODIPY **3** in DMSO at input energies of 32 and 45 μJ (A and B) and a concentration of 1.36×10^{-4} M.

Table 18. NLO parameters for BODIPY **3** in DMSO.

	Conc. (M)	Energy (μJ)	α (cm^{-1})	β_{eff} ($cm.GW^{-1}$)	Im[$\chi^{(3)}$] (esu)	γ (esu)	I_{lim} $J.cm^{-2}$
3	1.36×10^{-4}	32	0.53	1.62×10^{-7}	3.79×10^{-10}	4.13×10^{-30}	1.05
		45		1.70×10^{-7}	3.98×10^{-10}	4.33×10^{-30}	0.90

7.2.2. Second-order hyperpolarisability and third-order nonlinear susceptibility

At a molecular level, the second-order hyperpolarisability, γ,value describes the interaction of an incident photon with the permanent dipole moment of the BODIPY complexes, while the ultrafast response of a nonlinear optical material determined by the third-order nonlinear susceptibility, Im[$\chi^{(3)}$], value. Optimal Im[$\chi^{(3)}$] and γ values are typically in the range of 10^{-9}–10^{-15} and 10^{-29}–10^{-34}, respectively, for optical limiting materials [79,97]. **Table 18** summarises the Im[$\chi^{(3)}$] and γ values of BODIPY **3** in DMSO solution. The values obtained fall within the reported optimal ranges**.** When the input laser pulse energy is increased from 32 to 45 μJ, the Im[$\chi^{(3)}$] value for **3** decreased (**Table 18**), as would be expected for a good optical limiting material [79,97]. The nonlinear absorption per mole of the OL material is described by the γ

value and is especially useful when the efficiencies of different optical limiters are being compared.

7.2.3. Optical limiting threshold (I_{lim})

The optical limiting threshold or fluence, I_{lim}, describes the input fluence value at which the nonlinear transmittance is at 50% of the linear transmittance [95,97]. The I_{lim} values of BODIPY **3** were determined by using plots of input fluence *vs* output fluence (**Figure 7.3**), and transmittance *vs* input fluence (**Figure 7.4**). The I_{lim} values obtained for BODIPY **3** in solution are shown in **Table 18**, and as with the other parameters, they decrease with increasing input laser pulse energy. It can be concluded that **3** exhibits good nonlinear optical behaviour and on the basis of the RSA profiles obtained, it is reasonable to conclude that dyes of this type warrant further in depth investigation for use in optical limiting.

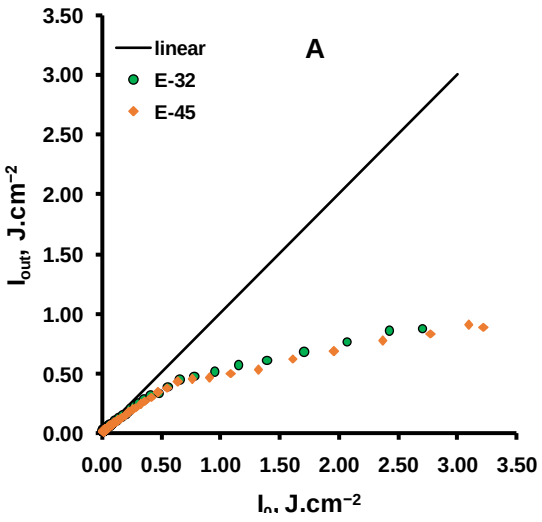

Figure 7.3. Plot of I_{out} vs. I_{in} for BODIPY **3** at input energies of 32 and 45 µJ.

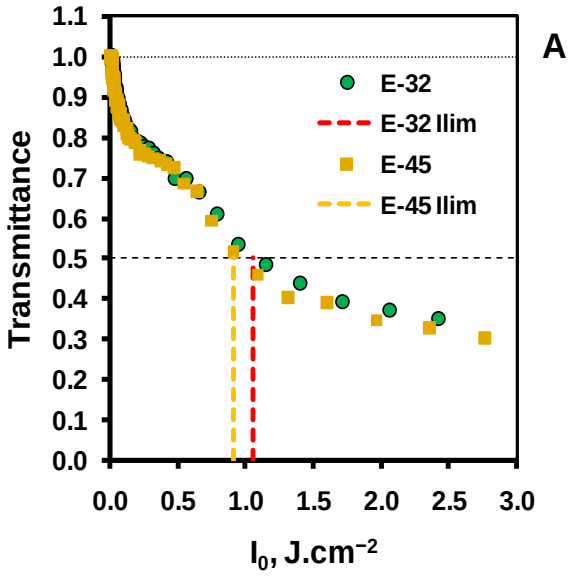

Figure 7.4. Normalised transmittance *vs.* input fluence curves for BODIPY **3**. Grey dotted lines indicate 50 % transmittance and are used to determine the $\boldsymbol{I_{lim}}$ values at input energies of 32 and 45 µJ for both dyes.

7.3. Concluding remarks

Substitution at the 3,5-positions of the BODIPY core caused a red-shifting of the main spectral bands to 648 nm for **3**. As a consequence of this, there is limited absorbance at 532 nm, and RSA behaviour is observed in DMSO solution during z-scan measurements. BODIPY **3** has bromine atoms at its 2,6-positions, which introduces a heavy atom effect, so their OL activity may arise from either 2PA or single photon absorption followed by ESA in the singlet and/or triplet manifolds. At the higher incident laser pulse energy that was studied, **3** exhibited a relatively low I_{lim} value of 0.90 J.cm^{-2}. This demonstrated that the dye is potentially suitable for use in practical applications.

CHAPTER 8

8. MOLECULAR MODELLING

8.1. Geometry Optimisation and TD-DFT calculations

The structure-property relationships and predicted spectral trends of a series of related BODIPY dyes were investigated using molecular modelling calculations. In this study, the electronic structure and TD-DFT calculations of BODIPYs **1a**, **1b**, **2a**, **2b**, **3** and **5** were investigated to elucidate trends in their HOMO and LUMO energies and hence their HOMO−LUMO energy gaps that determine changes in the wavelengths of their main spectral bands. The geometry optimisation calculations were performed with the Gaussian software package [136] by using the Beck, three-parameter, Lee-Yang-Parr (B3LYP) functional with 6-31G(d) basis sets in density functional theory (DFT) geometry optimisations. The B3LYP functional does not take sufficient account of long-range charge transfer that is often found in π-extended BODIPY dyes [14], so the Coulomb-attenuated B3LYP (CAM-B3LYP) functional was used instead for the TD-DFT calculations [14,137]. CAM-B3LYP contains a long-range correction for the exchange potential by incorporating an increasing fraction of the Hartree-Fock (HF) exchange. Correcting for the interelectronic separation enhances the analysis of compounds with significant charge transfer in the electronically excited states [137].

7.2. Molecular modelling for BODIPYs 1a, 1b, 2a, 2b, 3 and 5

The TD-DFT calculations predict that the lowest-lying $S_0 \rightarrow S_1$ transition can be attributed mainly to the HOMO → LUMO one-electron transition (**Table 19**). Complexation of BODIPY dyes with a boron trifluoride ligand leads to the HOMO and LUMO derived from an indacene ring system MOs being energetically well separated from other MOs, (**Figure 8.1**). In this regard, upon consideration of the effect of these structural changes on the optical properties of the dyes, changes in the HOMO and LUMO energies are primarily considered since the other MOs are usually not involved in the changes observed in the energies of the main spectral band.

The structural changes and concomitant effects cause a red-shift of the BODIPY main spectral band as a result of the narrowing of the HOMO−LUMO energy band gap.

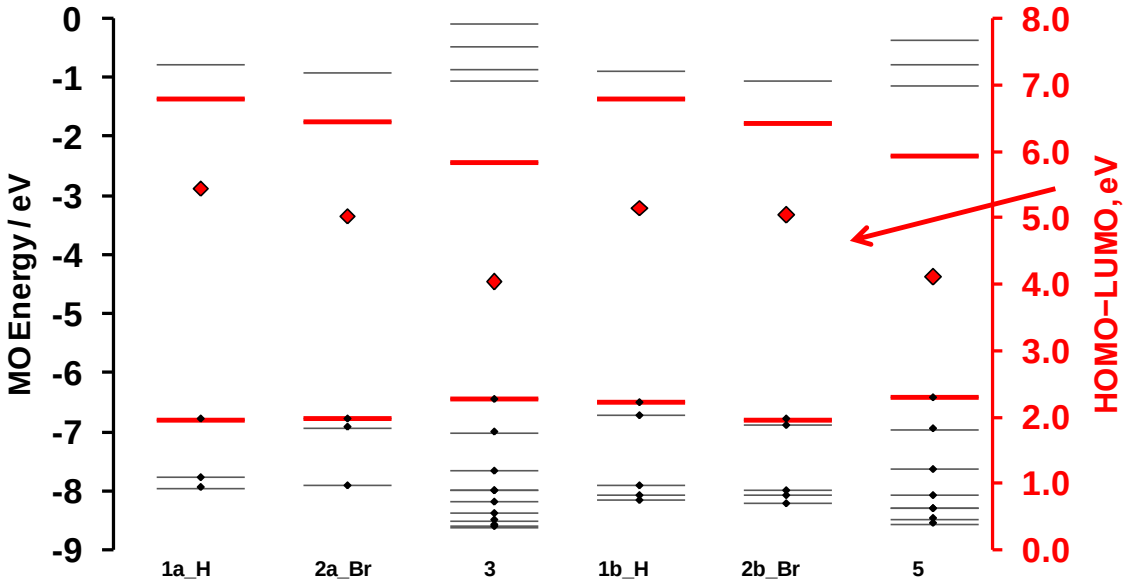

Figure 8.1. MO energies of BODIPYs **1a**, **2a**, **3**,**1b, 2b** and **5** at the CAM-B3LYP/6-31G(d) level of theory. The HOMO–LUMO gaps are plotted against a secondary axis and are denoted by large red diamonds. The occupied MOs are highlighted with small black squares.

In moving from BODIPYs **1a** to **2a** and **3** (**Figure 8.2**), there was an observable increase in the number of nodal planes and changes in electron density. Firstly, the addition of bromine atoms at the 2,6-positions on moving from **1a** to **2a** causes an electron-donating mesomeric effect that leads to a relative destabilisation of the HOMO, due to there being larger MO coefficients at these positions than is the case with the LUMO (**Figure 8.2**). This results in a narrowing of the HOMO–LUMO band gap (**Figure 8.1**). This results in the ca. 18 nm red-shift predicted for BODIPYs **2a** and **2b** in the calculated TD-DFT spectra. This red shift is consistently observed upon the substitution with bromine atoms at the 2,6-positions of BODIPY dyes [11].

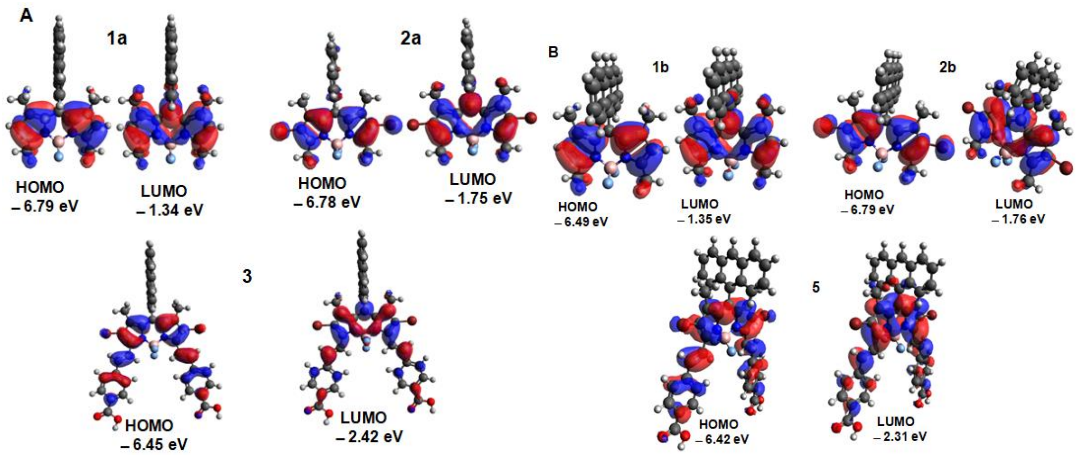

Figure 8.2. Angular nodal patterns and MO energies for the HOMO and LUMO (at an isosurface value of 0.02 a.u) of BODIPYs **1a**, **2a**, **3** (A), **1b, 2b** and **5** (B).

The MO coefficients at the 3,5-positions are unevenly distributed on the HOMO and LUMO of BODIPYs **3** and **5**. The evidence for this can be observed in the large MO coefficients in the HOMO with respect to the LUMO (**Figure 8.2**). In this regard, structural changes at the 3,5-positions are expected to give rise to a change in the size of the HOMO−LUMO band gap because the HOMO is affected more significantly. As can be observed, the introduction of the styryl groups at the 3,5-positions results in a further red-shift of ca. 138 nm for BODIPY **3** and ca. 116 nm for BODIPY **5** (**Figure 8.3** and **Table 19**). The different substituents present on the styryl groups are expected to have an effect on the extent of red-shifting observed on the main spectral bands, since this will change the degree of destabilisation of the HOMO with respect to the LUMO. Other transitions are predicted to result in intense bands in the visible region [14]. This is evident from the large oscillator strengths that are predicted both for the main absorption band (**Table 19**) and the absorption bands observed in the 300–450 nm region as shown in (**Figure 8.3**). Critically, however, from the standpoint of optical limiting, there is a large energy gap between the S_1 and S_2 excited states. This means that there is relatively weak absorbance across most of the visible region. Ideally, an optical limiter should not absorb significantly under ambient light conditions, so this enhances the suitability of **3** for this application.

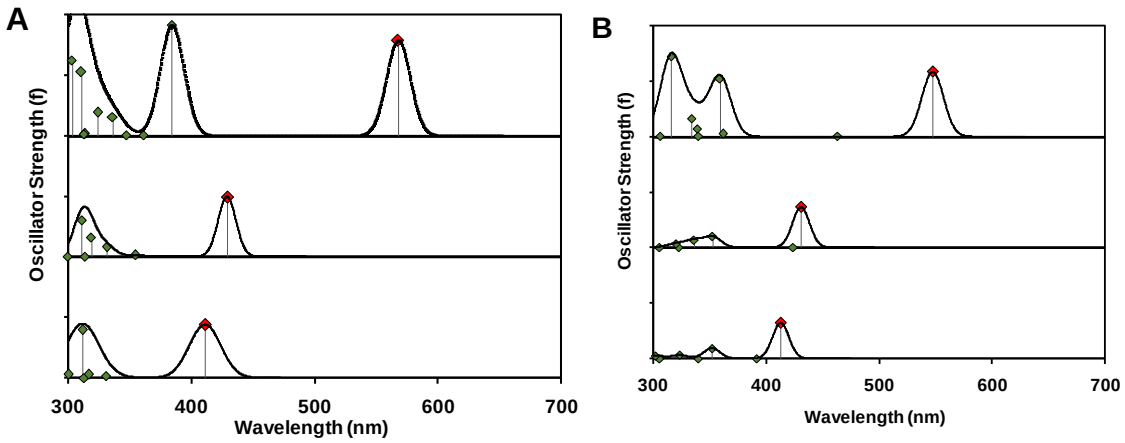

Figure 8.3. Calculated TD-DFT spectra of BODIPYs **1a**, **2a**, **3** (A), and **1b**, **2b**, and **5** (B) at the CAM-B3LYP/6-31G(d) level of theory. The main spectral bands associated with the HOMO→LUMO transition are found between 400 and 500 nm for BODIPYs **1a**, **1b**, **2a**and **2b**, and between 500 and 670 nm for BODIPYs **3** and **5**. Simulated spectra were calculated using the Chemcraft program [138] by using bandwidths of 30 nm.

Table 19. TD-DFT calculations at the CAM-B3LYP/6-31G(d) level of theory for the B3LYP optimised geometries of BODIPY **1a**, **1b**, **2a**, **2b**, **3** and **5**.

	#[a]	Energy (eV)[b]	λ_{calc} (nm)[c]	f[d]	Wavefunction[e] =
1a	1	3.01	411	0.53	96% H→L;…
	2	3.74	330	0.02	73% H–1→L;…
	3	3.91	316	0.04	72% H–3→L;…
	4	4.12	300	0.04	89% H–4→L;…
2a	1	2.89	429	0.59	92% H→L;…
	2	3.49	354	0.01	87 % H–1→L;…
	3	3.74	331	0.10	90% H–3→L;…
	4	3.89	318	0.19	87% H–4→L;…
3	1	2.18	567	0.94	95% H →L;…
	2	3.22	384	1.09	93% H–1→L;…
	3	3.68	336	0.18	90% H→L+1; 3% H–3→L;…
	4	3.82	324	0.23	89% H–6→L; 2% H–9→L;…
	5	3.98	310	0.63	75% H–2→L+1; 9% H→L+3; 7% H–4→L+2;….
	6	4.08	303	0.74	73% H→L+3); 8% H–4→L; 7% H–2→L+1;…
1b	1	3.00	413	0.52	97% H→L;…
	2	3.16	391	0.00	97% H–1→L;…
	3	3.52	352	0.15	97% H–1→L+1;…
	4	3.64	340	0.00	97% H→L+1;…
2b	1	2.87	431	0.58	97% H→L;…
	2	2.92	423	0.00	97% H–1→L;…
	3	3.69	336	0.11	93% H–2→L;….
	4	3.84	322	0.00	95% H→L+1;….
5	1	2.26	547	0.93	96% H→L;…
	2	2.67	463	0.00	94% H–1→L;…
	3	3.42	361	0.04	86% H–3→L; …
	4	3.45	359	0.83	72% H–1→L+1; 23% H–2→L;…
	5	3.64	340	0.00	90% H→L+1; …
	6	3.71	334	0.25	75% H–5→L; 19% H–2→L;…

a - Excited state number assigned in increasing energy in the TD-DFT calculations. b - Calculated band energies in eV. c - Calculated wavelengths in nm. d - Calculated oscillator strengths. e - Wavefunctions of MOs involved in the transition, and their respective contributions, based on eigenvectors predicted by TD-DFT. H and L refer to the HOMO and LUMO, respectively.

8.3. Concluding remarks

The TD-DFT calculations are a useful tool for studying the structure-property relationships of BODIPY dyes by predicting trends in the energies of the frontier MOs of the dyes and providing insights into the spectroscopic properties that result from different structural modifications. This is useful in the design of specific BODIPY dyes for various applications such as photocatalytic degradation, photodynamic antimicrobial chemotherapy where red-shifted brominated analogues are needed, and in optical limiting where the main spectral band of the dyes must be significantly red-shifted above 500 nm. The trends in the calculations match the experimental electronic absorption spectra, as observed not only in the series of BODIPY dyes modelled but also those of other dyes that have been synthesised.

CHAPTER 9

9. CONCLUSIONS, LIMITATIONS AND FUTURE PROSPECTS

9.1. Conclusions

The main aim of this work was to synthesise and characterise a series of structurally modified BODIPY dyes with properties that make them suitable for use as photosensitiser dyes in PACT, as optical limiting materials in NLO, and as photocatalysts during the photocatalytic degradation of environmental pollutants. The latter application involved the preparation of BODIPY-dye-embedded polymer fibres for the photocatalytic degradation of organic pollutants. A study of the photophysical properties of these dyes was undertaken to enable an understanding of the properties of these dyes for intended applications.

In order to achieve the aims listed above, the first step was to synthesise five BODIPY core dyes **1a-e**, by using the classic "one-pot three-step" Lewis acid catalysed condensation reaction. The synthesised BODIPY dyes have similar optical properties, since BODIPY dyes derived from 2, 4-dimethylpyrrole have *meso*-aryl rings that lie orthogonal to the BODIPY core. Significant differences are observed in their fluorescence properties, even when studied in different solvents. BODIPYs **1a**, **1b**, and **1e** exhibited fluorescent properties, which are independent of solvent polarity, while BODIPY **1c** has low fluorescence quantum yields as a result of the quenching effect of the strong electron-withdrawing nitro group.

BODIPY core dyes **1a-e** was brominated at the 2,6-positions to yield BODIPYs **2a-e**. The main spectral bands are red-shifted by ca. 30 nm relative to those of their parent dyes. The brominated BODIPY dyes have relatively high singlet oxygen quantum yields in the different solvents studied. This makes them suitable for use in singlet oxygen applications such as PACT and the photocatalytic degradation of organic pollutants, which do not require further red-shifted photosensitiser. BODIPYs **2a** and **4** were embedded as heterogenous photocatalysts in electrospun polymer fibres for the photocatalytic degradation of azo dyes (Orange G and

Methyl Orange). The studies were carried out in aqueous solution. The singlet oxygen generating proficiency of the dye embedded polymer fibres was assessed by using ADMA as a singlet oxygen scavenger in aqueous solution. A significant reduction in the main absorption band of ADMA was observed, and this provided an indication of the ability of the dye to generate singlet oxygen when embedded in PS nanofibres. The photocatalytic degradation of organic environmental pollutants Orange G and Methyl Orange was undertaken using BODIPY embedded nanofibres, which proved to be efficient photocatalysts during the photodegradation of azo dyes.

For some of the possible applications, a red shift of the main BODIPY absorption band is required. Two novel distyryl BODIPY dyes **3** and **5** were synthesised from BODIPYs **2a** and **2b**; by following a modified version of the Knoevenagel condensation reaction. Their main absorption band maxima are red-shifted into the therapeutic window with absorption maxima at 657 and 663 nm in DMSO. The red-shifted absorbance, coupled with their moderate singlet oxygen quantum yield values makes BODIPYs **3** and **5** potentially suitable for use as singlet oxygen generating photosensitisers in PDT applications, as well as in PACT and in photocatalysis. BODIPYs **2a**, **3** and **5** proved to be effective photosensitiser dyes during the PACT inactivation of *Staphylococcus aureus*, with log reduction values of 9.01, 9.18 and 9.13 respectively, while lacking effectiveness for the photoinactivation of *Escherichia coli*. This can be attributed to the fact that *Escherichia coli*, is a gram-negative bacteria which contains an extra outer membrane in the cell wall structure which envelopes the peptidoglycan layer. The red-shifted absorption maxima of the 3,5-distyryl dyes lie over 100 nm from 532 nm, the wavelength of the second harmonic of the Nd:YAG laser and this makes the dyes suitable for use as optical limiting materials in NLO applications. BODIPY **3** showed very promising optical limiting responses on the nanosecond timescale in solution over the range of energies studied, further demonstrating that the π-expanded BODIPY dyes have considerable potential in this regard.

9.2 Limitations and future prospects

- With respect to applications as photosensitiser dyes in PACT, water solubility is an important requirement. Scope exists to conjugate the BODIPY dyes to drug nanocarriers to improve solubilisation in water, and it is also possible to introduce water-solubilising groups directly to the BODIPY dyes. Application of the BODIPY-MNP conjugates in PACT in this study was not effective due to problems of solubility. In this regard, gold nanoparticles could be conjugated to the dyes in order to improve solubility and achieve higher singlet oxygen generation as a result of the heavy atom effect.
- With respect to the photocatalytic degradation of environmental pollutants, although the use of polystyrene was effective because of the π-π interactions between the BODIPY dyes and the aromatic styryls of the polystyrene structure, which improved the stability and enabled the recycling of the photocatalysts. The introduction of functional groups to the BODIPY dyes that can form covalent linkages with other types of polymers may prove to be more effective. Further research on incorporating MNP-BODIPY conjugates into electrospun nanofibres for the photodegradation of pollutants is merited, since this would enhance the ability to reuse the fibres by making use of their magnetic properties to remove them from solution.
- The NLO studies were undertaken in solutions only, but from the standpoint of practical applications, the fabrication of thin films is an important consideration for future work. The remarkable OL response from BODIPY **3** provides the basis for the rational design of more novel BODIPY dyes with donor-π-acceptor type structures for use as optical limiters on the nanosecond timescale, at 532 nm

References

[1] Ulrich, G.; Ziessel, R.; Harriman, A. The chemistry of fluorescent bodipy dyes: versatility unsurpassed. *Angew. Chem. Int. Ed.* **2008**, *47*, 1184-1201.

[2] Loudet, A.; Burgess, K. BODIPY dyes and their derivatives: syntheses and spectroscopic properties. *Chem. Rev.* **2007**, *107*, 4891-4932.

[3] Sun, J.; Qiao, L.; Sun, S.; Wang, G. Photocatalytic degradation of Orange G on nitrogen-doped TiO_2 catalysts under visible light and sunlight irradiation. *J. Hazard. Mater.* **2008**, *155*,312-319.

[4] Zugle, R.; Nyokong, T. Comparative phototransformation of environmental pollutants using metallophthalocyanines supported on electrospun polymer fibers. *J. Appl. Polym. Sci.* **2013**, *128*, 1131-1142.

[5] Domınguez, C.; Garcıa, J.; Pedraz, M.; Torres, A.; Galan, M. Photocatalytic oxidation of organic pollutants in water. *Catal. Today* **1998**, *40*, 85-101.

[6] Wainwright, M. Photodynamic antimicrobial chemotherapy (PACT). *J. Antimicrob. Chem.* **1998**, *42*, 13-28.

[7] Shen, Y. *The Principles of Nonlinear Optics*. Wiley-Interscience: New York, 1984.

[8] Banerjee, P.P. *Nonlinear optics: Theory, Numerical Modeling, and Applications*; CRC Press: Boca Raton, Florida, 2003.

[9] Boens, N.; Leen, V.; Dehaen, W. Fluorescent indicators based on BODIPY. *Chem. Soc. Rev.* **2012**, *41*, 1130-1172.

[10] DeRosa, M.C.; Crutchley, R.J. Photosensitized singlet oxygen and its applications. *Coord. Chem. Rev.* **2002**, *233*, 351-371.

[11] Jiao, L.; Pang, W.; Zhou, J.; Wei, Y.; Mu, X.; Bai, G.; Hao, E. Regioselective stepwise bromination of boron dipyrromethene (BODIPY) dyes. *J. Org. Chem.* **2011**, *76*, 9988-9996.

[12] Treibs, A.; Kreuzer, F. Difluorboryl-Komplexe von Di und Tripyrrylmethenen. *Justus Liebigs Ann. Chem.* **1968**, *718*, 208-223.

[13] Kamkaew, A.; Lim, S.H.; Lee, H.B.; Kiew, L.V.; Chung, L.Y.; Burgess, K. BODIPY dyes in photodynamic therapy. *Chem. Soc. Rev.* **2013**, *42*, 77-88.

[14] Lu, H.; Mack, J.; Yang, Y.; Shen, Z. Structural modification strategies for the rational design of red/NIR region BODIPYs. *Chem. Soc. Rev.* **2014**, *43*, 4778-4823.

[15] Spiller, W.; Kliesch, H.; Wöhrle, D.; Hackbarth, S.; Röder, B.; Schnurpfeil, G. Singlet oxygen quantum yields of different photosensitizers in polar solvents and micellar solutions. *J. Porphyrins Phthalocyanines* **1998**, *2*, 145-158.

[16] Schmitt, A.; Hinkeldey, B.; Wild, M.; Jung, G. Synthesis of the Core Compound of the BODIPY Dye Class: 4,4′-Difluoro-4-bora-(3a,4a)-diaza-*s*-indacene. *J. Fluoresc.* **2009**, *19*,755-758.

[17] Ni, Y.; Wu, J. Far-red and near-infrared BODIPY dyes: synthesis and applications for fluorescent pH probes and bio-imaging. *Org. Biomed. Chem.* **2014**, *12*, 3774-3791.

[18] Tram, K.; Yan, H.; Jenkins, H. A.; Vassiliev, S.; Bruce, D. The synthesis and crystal structure of unsubstituted 4,4-difluoro-4-bora-3a,4a-diaza-*s*-indacene (BODIPY). *Dyes Pigments* **2009**, *82*, 392-395.

[19] Arroyo, I. J.; Hu, R.; Merino, G.; Tang, B.Z.; Pena-Cabrera, E. The smallest and one of the brightest. Efficient preparation and optical description of the parent boron-dipyrromethene system. *J. Org. Chem.* **2009**, *74*, 5719-5722.

[20] Boens, N.; Verbelen, B.; Dehaen, W. Postfunctionalization of the BODIPY core: synthesis and spectroscopy. *Eur. J. Org. Chem.* **2015**, *2015*, 6577-6595.

[21] Uppal, T.K. Synthesis and Characterization of Red and Near-Infrared BODIPY-based fluorophores for various Biological Applications. PhD Thesis, Louisiana State University, Baton Rouge, Louisiana, 2012.

[22] Wood, T.E.; Thompson, A. Advances in the chemistry of dipyrrins and their complexes. *Chem. Rev.* **2007**, *107*, 1831-1861.

[23] Goud, T. V.; Tutar, A.; Biellmann, J. Synthesis of 8-heteroatom-substituted 4, 4-difluoro-4-bora-3a, 4a-diaza-*s*-indacene dyes (BODIPY). *Tetrahedron* **2006**, *62*, 5084-5091.

[24] Leen, V. Synthesis and application of reactive BODIPY dyes. PhD Thesis, Katholieke Universiteit, Leuven, Belgium, 2010.

[25] Dost, Z.; Atilgan, S.; Akkaya, E.U. Distyryl-boradiazaindacenes: facile synthesis of novel near IR emitting fluorophores. *Tetrahedron* **2006**, *62*, 8484-8488.

[26] Deniz, E.; Isbasar, G.C.; Bozdemir, O.A.; Yildirim, L. T.; Siemiarczuk, A.; Akkaya, E. U. Bidirectional switching of near IR emitting boradiazaindacene fluorophores. *Org. Lett.* **2008**, *10*, 3401-3403.

[27] Ekmekci, Z.; Yilmaz, M.D.; Akkaya, E.U. A monostyryl-boradiazaindacene (BODIPY) derivative as a colorimetric and fluorescent probe for cyanide ions. *Org. Lett.* **2008**, *10*, 461-464.

[28] Rohand, T.; Baruah, M.; Qin, W.; Boens, N.; Dehaen, W. Functionalisation of Fluorescent BODIPY Dyes by Nucleophilic Substitution. *Chem. Commun.* **2006**, *43*, 266-268

[29] Chen, J.; Burghart, A.; Derecskei-Kovacs, A.; Burgess, K. 4,4-Difluoro-4-Bora-3a,4a-Diaza-*s*-Indacene (BODIPY) Dyes Modified for Extended Conjugation and Restricted Bond Rotations. *J. Org. Chem.* **2000**, *65*, 2900-2906.

[30] Yogo, T.; Urano, Y.; Ishitsuka, Y.; Maniwa, F.; Nagano, T. Highly efficient and photostable photosensitizer based on BODIPY chromophore. *J. Am. Chem. Soc.* **2005**, *127*, 12162-12163.

[31] Li, L.; Nguyen, B.; Burgess, K. Functionalization of the 4,4-difluoro-4-bora-3a,4a-diaza-*s*-indacene (BODIPY) core. *Bioorg. Med. Chem. Lett.* **2008**, *18*, 3112-3116.

[32] Ulrich, G.; Goze, C.; Guardigli, M.; Roda, A.; Ziessel, R. Pyrromethenedialkynylborane complexes for "Cascatelle" energy transfer and protein labeling. *Angew. Chem.* **2005**, *117*, 3760-3764.

[33] Qin, W.; Rohand, T.; Dehaen, W.; Clifford, J.N.; Driesen, K.; Beljonne, D.; Van Averbeke, B.; Van der Auweraer, M.; Boens, N. Boron dipyrrometheneanalogs with phenyl, styryl, and ethynylphenyl substituents: synthesis, photophysics, electrochemistry, and quantum-chemical calculations. *J. Phys. Chem. A.* **2007**, *111*, 8588-8597.

[34] Harriman, A.; Izzet, G.; Ziessel, R. Rapid energy transfer in cascade-type bodipy dyes. *J. Am. Chem. Soc.* **2006**, *128*, 10868-10875.

[35] Benniston, A.C.; Copley, G. Lighting the way ahead with boron dipyrromethene (Bodipy) dyes. *Phys. Chem. Chem. Phys.* **2009**, *11*, 4124-4131.

[36] Boens, N.; Leen, V.; Dehaen, W.; Wang, L.; Robeyns, K.; Qin, W.; Tang, X.; Beljonne, D.; Tonnelé, C.; Paredes, J.M. Visible absorption and fluorescence spectroscopy of conformationally constrained, annulated BODIPY dyes. *J. Phys. Chem. A* **2012**, *116*, 9621-9631.

[37] McDonnell, S.O.; O'Shea, D.F. Near-infrared sensing properties of dimethylamino-substituted BF_2-azadipyrromethenes. *Org. Lett.* **2006**, *8*, 3493-3496.

[38] Donyagina, V.F.; Shimizu, S.; Kobayashi, N.; Lukyanets, E.A. Synthesis of N,N-difluoroboryl complexes of 3,3′-diarylazadiisoindolylmethenes. *Tetrahedron Lett.* **2008**, *49*, 6152-6154.

[39] Wang, D.; Liu, R.; Chen, C.; Wang, S.; Chang, J.; Wu, C.; Zhu, H.; Waclawik, E.R. Synthesis, photophysical and electrochemical properties of aza-boron-diquinomethene complexes. *Dyes Pigments* **2013**, *99*, 240-249.

[40] Liu, H.; Lu, H.; Zhou, Z.; Shimizu, S.; Li, Z.; Kobayashi, N.; Shen, Z. Asymmetric core-expanded aza-BODIPY analogs: facile synthesis and optical properties. *Chem. Commun.* **2015**, *51*, 1713-1716.

[41] Adarsh, N.; Avirah, R.R.; Ramaiah, D. Tuning photosensitized singlet oxygen generation efficiency of novel aza-BODIPY dyes. *Org. Lett.* **2010**, *12*, 5720-5723.

[42] LópezArbeloa, F.; Banuelos, J.; Martínez, V.; Arbeloa, T.; LópezArbeloa, I. Structural, photophysical and lasing properties of pyrromethene dyes. *Int. Rev. Phys. Chem.* **2005**, *24*, 339-374.

[43] Lopez, A.F.; Lopez, A.T.; Lopez, A.I.; Garca-Moreno, I.; Costela, A.; Sastre, R.; Amat-Guerri, F. Photophysical and lasing properties of pyrromethene567 dye in liquid solution.-Environment effects. *Chem. Phys.* **1998**, *236*, 331-341.

[44] Magde, D.; Wong, R.; Seybold, P. G. Fluorescence Quantum Yields and Their Relation to Lifetimes of Rhodamine 6G and Fluorescein in Nine Solvents: Improved Absolute Standards for Quantum Yields. *Photochem. Photobiol.* **2002**, *75*, 327-334.

[45] Pavlopoulos, T.G. Scaling of dye lasers with improved laser dyes. *Prog. Quant. Electron.* **2002**, *26*, 193-224.

[46] F. P. Schäfer, *Dye Lasers*, 3rd Ed., Springer-Verlag, Berlin, 1990.

[47] Kubheka, G.; Uddin, I.; Amuhaya, E.; Mack, J.; Nyokong, T. Synthesis and photophysicochemical properties of BODIPY dye functionalized gold nanorods for use in antimicrobial photodynamic therapy. *J. Porphyrins Phthalocyanines* **2016**, *20*, 1016-1024.

[48] Gandin, E.; Lion, Y.; Van de Vorst, A. *Photochem. Photobiol*. **1983**, *37*, 271-278.

[49] Maaz, K.; Ihsan, A.; Fatima, I.; Masood, F.; Karim, S. Synthesis of Co_xNi_1-XFe_2O_4 (X= 0.0, 0.5, 1.0) Nanoparticles by Chemical Co-Precipitation Route. *Int. J. Nano Stud. Technol.* **2014**, *3*, 55-58.

[50] Aygar, G.; Kaya, M.; Özkan, N.; Kocabıyık, S.; Volkan, M. Preparation of silica coated cobalt ferrite magnetic nanoparticles for the purification of histidine-tagged proteins. *J. Phys. Chem. Solids* **2015**, *87*, 64-71.

[51] Rahul, P.; Lisa, R.; Weihong, T. Surface modifications of silica nanoparticles to reduce aggregation and nonspecific binding. *Langmuir*. **2004**, *20*, 8336-8342.

[52] Artuor, A.; Hontago, W.; Dongxu, Z.; Hunter, S.; Gary, C.; Bradley, J.; Robert, M.; Zhaoxia, J. Stability and Aggregation of Metal Oxide Nanoparticles in Natural Aqueous Matrices. *Environ. Sci. Technol*. **2010**, *44*, 1962-1967.

[53] Serena, A.; Yurry, P.; Yurii, K. Multifunctional Magnetic-fluorescent Nanocomposites for Biomedical Applications. *Nanoscale Res. Lett.***2008**, *3*, 87-104.

[54] Gopal, C.; Manorama, S.; Rao, V. Semiconducting gas sensor for chlorine based on inverse spinel nickel ferrite. *Sensors Actuators B* **1999**, *55*, 90-95.

[55] Eric, C.; Virender, K.S.; Xiang-Zhong, L. Synthesis and photocatalytic activity of ferrites under visible light. *Sep. Purif. Technol.* **2012**, *87*, 1-14.

[56] Dippong, T.; Toloman, D.; Levei, E.A.; Cadar, O.; Mesaros, A. A possible formation mechanism and photocatalytic properties of $CoFe_2O_4$/PVA-SiO_2 nanocomposites. *Thermochim. Acta*. **2018**, *666*, 103-115.

[57] Maaz, K.; Mumtax, A.; Hasanain, S.K.; Ceylan, A. Synthesis and magnetic properties of cobalt ferrite ($CoFe_2O_4$) nanoparticles prepared by wet chemical route. *J. Magn. Magn. Mater.* **2007**, *308*, 289-295.

[58] Dutta, P.K.; Pehkonen, S.O.; Sharma, V.K.; Ray, A.K. Photocatalytic oxidation of arsenic (III): evidence of hydroxyl radicals. *Environ. Sci. Technol*. **2005**, *39*, 1827-1834.

[59] Feng, L.; Junjie, L.; David, G.; Xue, D. Stoichiometric Synthesis of Pure MFe_2O_4 (M) Mg, Co, and Ni) Spinel Ferrites from Tailored Layered Double Hydroxide (Hydrotalcite-Like) Precursors. *Chem. Mater*. **2004**, *16*, 1597-1602.

[60] Robinson, T.; McMullan, G.; Marchant, R.; Nigam, P. Remediation of dyes in textile effluent: a critical review on current treatment technologies with a proposed alternative. *Bioresour. Technol.* **2001**, *77*, 247-255.

[61] Ramakrishna, S.; Fujihara, K.; Teo, W.; Yong, T.; Ma, Z.; Ramaseshan, R. Electrospun nanofibres: solving global issues. *Mater. Today* **2006**, *9*, 40-50.

[62] Zugle, R.; Nyokong, T. Physico-chemical properties of lutetium phthalocyanine complexes in solution and in solid polystyrene polymer fibres and their application in photoconversion of 4-nitrophenol. *J. Mol. Catal. A* **2012**, *358*, 49-57.

[63] Mu, Y.; Guo, D.; Hou, Y.; Wang, S. Facile electrospinning preparation and superior luminescence properties of BODIPY composite nanofibres. *Text. Res. J.* **2017**, *87*, 1795-1805.

[64] Li, W.; Xie, Z.; Jing, X. BODIPY photocatalysed oxidation of thioanisole under visible light. *Catal. Commun*. **2011**, 16, 94-97.

[65] Giroldo, L.M.; Felipe, M.P.; de Oliveira, M.A.; Munin, E.; Alves, L.P.; Costa, M.S. Photodynamic antimicrobial chemotherapy (PACT) with methylene blue increases membrane permeability in *Candida albicans*. *Lasers Med. Sci.* **2009**, *24*, 109-112.

[66] Osifeko, O.L.; Uddin, I.; Mashazi, P.N.; Nyokong, T. Physicochemical and antimicrobial photodynamic chemotherapy of unsymmetrical indium phthalocyanines alone or in the presence of magnetic nanoparticles. *New J. Chem.* **2016**, *40*, 2710-2721.

[67] Phoenix, D.A.; Dennison, S.R.; Harris, F. Photodynamic antimicrobial chemotherapy. In *Novel Antimicrobial Agents and Strategies*, Phoenix, D. A.; Dennison, S. R.; Harris, F. (Eds), Wiley-VCH: Weinheim, Germany, 2014, pp. 295-330.

[68] Gois, M.M.; Kurachi, C.; Santana, E.; Mima, de Oliveira, E.G.; Spolidório, D.M.P.; Pelino, J.E.P.; Bagnato, V.S. Susceptibility of *Staphylococcus aureus* to porphyrin-mediated photodynamic antimicrobial chemotherapy: an in vitro study. *Lasers Med. Sci.* **2010**, *25*, 391-395.

[69] Raab, O. Ueber die Wirkung Fluorizierender Stoffe auf Infusorien. *Z. Biol*. **1900**, 39, 524-546.

[70] Sharman, W.M.; Allen, C.M.; Van Lier, J.E. Photodynamic therapeutics: basic principles and clinical applications. *Drug Discov. Today* **1999**, *4*, 507-517.

[71] Nishijima, S.; Namura, S.; Mitsuya, K.; Asada, Y. The incidence of isolation of methicillin-resistant *Staphylococcus aureus* (MRSA) strains from skin infections during the past three years (1989–1991). *J. Dermatol.* **1993**, *20*,193-197.

[72] Chen, W.; Lu, W.; Yao, Y.; Xu, M. Highly efficient decomposition of organic dyes by aqueous-fiber phase transfer and in situ catalytic oxidation using fiber-supported cobalt phthalocyanine. *Environ. Sci. Technol.* **2007**, *41*, 6240-6245.

[73] Chatterjee, D.; Dasgupta, S. Visible light induced photocatalytic degradation of organic pollutants. *J. Photochem. Photobiol. C* **2005**, *6*, 186-205.

[74] Tanaka, K.; Padermpole, K.; Hisanaga, T. Photocatalytic degradation of commercial azo dyes. *Water Res.* **2000**, *34*, 327-333.

[75] Rajeshwar, K.; Osugi, M.; Chanmanee, W.; Chenthamarakshan, C.; Zanoni, M.V.B.; Kajitvichyanukul, P.; Krishnan-Ayer, R. Heterogeneous photocatalytic treatment of organic dyes in the air and aqueous media. *J. Photochem. Photobiol. C* **2008**, *9*, 171-192.

[76] Rauf, M.; Ashraf, S.S. Fundamental principles and application of heterogeneous photocatalytic degradation of dyes in solution. *Chem. Eng. J.* **2009**, *151*, 10-18.

[77] Ding, X.; Han, B. Metallophthalocyanine-Based Conjugated Microporous Polymers as Highly Efficient Photosensitizers for Singlet Oxygen Generation. *Angew. Chem. Int. Ed.* **2015**, *54*, 6536-6539.

[78] Wöhrle, D.; Suvorova, O.; Gerdes, R.; Bartels, O.; Lapok, L.; Baziakina, N.; Makarov, S.; Slodek, A. Efficient oxidations and photooxidations with molecular oxygen using metal phthalocyanines as catalysts and photocatalysts. *J. Porphyrins Phthalocyanines* **2004**, *8*, 1020-1041.

[79] Sutherland, R.L. Nonlinear absorption. In *Handbook of Nonlinear Optics*, 2nd ed.; Marcel Dekker: New York, 2003, pp. 579-626.

[80] Zhou, G.; Wang, X.; Wang, D.; Wang, C.; Shao, Z.; Fang, Q.; Jiang, M. Two-photon absorption and nonlinear optical properties of a new organic dye PSPI. *Opt. Commun.* **2001**, *190*, 345-349.

[81] Wolff, J.J.; Wortmann, R. Organic Materials for Second-order Non-linear Optics. In *Advances in Physical Organic Chemistry*, *Vol. 32*, Williams, N.H.; Williams, I.H. (Eds), Elsevier: Amsterdam, The Netherlands, 1999; pp. 121-217.

[82] Eaton, D.F. Nonlinear optical materials. *Science* **1991**, *253*, 281-287.

[83] He, G.S.; Liu, S.H. *Physics of Nonlinear Optics;* World Scientific: Singapore, 1999.

[84] Perry, J. Organic and Metal-containing Reverse Saturable Absorbers for Optical Limiters. In *Nonlinear Optics of Organic Molecules and Polymers* , Nalwa, H.S.; Seizo Miyata S. (Eds), CRC Press: Boca Raton, Florida, 1997, pp. 813-840.

[85] Sanusi, K.; Amuhaya, E.K; Nyokong, T. Enhanced optical limiting behavior of an indium phthalocyanine-single-walled carbon nanotube composite: an investigation of the effects of solvents. *J. Phys. Chem. C* **2014**, *118*, 7057-7069.

[86] de la Torre, G.; Torres, T.; Agulló-López, F. The phthalocyanine approach to second harmonic generation. *Adv. Mater*. **1997**, *9*, 265-269.

[87] Potamianos, D.; Giannakopoulou, P.; Kaloudi-Chantzea, A.; Pistolis, G.; Couris, S. Third-order nonlinear optical properties of some novel BODIPYs. 16th International Conference on Transparent Optical Networks (ICTON); IEEE: Piscataway, New Jersey, 2014; pp. 1-3.

[88] Wang, J.; Hernandez, Y.; Lotya, M.; Coleman, J.; Blau, W. Broadband nonlinear optical response of graphene dispersions. *Adv. Mater*. **2009**, *21*, 2430-2435.

[89] Band, Y. Optical properties and applications of reverse saturable absorbers. In *Methods of Laser Spectroscopy*; Prior, Y.; Ben-Reuven, A.; Rosenbluh, M. (Eds); Plenum Press: New York, 1986; pp. 117-121.

[90] Harris, J.; Gai, L.; Kubheka, G.; Mack, J.; Nyokong, T.; Shen, Z. Optical Limiting Properties of 3,5-Dithienylenevinylene BODIPY Dyes at 532 nm. *Chem. Eur. J.* **2017**, *23*, 14507-14514.

[91] Kubheka, G.; Achadu, O.; Mack, J.; Nyokong, T. Optical limiting properties of 3, 5-diphenyldibenzo-azaBODIPY at 532 nm. *New J. Chem.* **2017**, *41*, 12319-12325.

[92] Ngoy, B. P.; Hlatshwayo, Z.; Nwaji, N.; Fomo, G.; Mack, J.; Nyokong, T. Photophysical and optical limiting properties at 532 nm of BODIPY dyes with p-benzyloxystyryl groups at the 3, 5-positions. *Journal Porphyrins Phthalocyanines* **2018**, *22*, 413-422.

[93] De La Torre, G.; Vazquez, P.; Agullo-Lopez, F.; Torres, T. Role of structural factors in the nonlinear optical properties of phthalocyanines and related compounds. *Chem. Rev.* **2004**, *104*, 3723-3750.

[94] Sheik-Bahae, M.; Said, A.A.; Van Stryland, E.W. High-sensitivity, single-beam n^2 measurements. *Opt. Lett.* **1989**, *14*, 955-957.

[95] Sheik-Bahae, M.; Said, A.A.; Wei, T.; Hagan, D.J.; Van Stryland, E.W. Sensitive measurement of optical nonlinearities using a single beam. *IEEE J. Quant. Electron*. **1990**, *26*, 760-769.

[96] Neethling, P. H, Determining non-linear optical properties using the Z-scan technique. MSc Thesis, Stellenbosch University, South Africa, 2005.

[97] Dini, D.; Hanack, M. Physical properties of phthalocyanine-based materials. In *the Porphyrin Handbook*; Kadish, K.M.; Smith, K.M.; Guilard, R. (Eds); Academic Press: Cambridge, Massachusetts, 2003; pp. 22-31.

[98] Hollins, R. Materials for optical limiters. *Curr. Opin. Solid State Mater. Sci.* **1999**, *4*, 189-196.

[99] Fery-Forgues, S.; Lavabre, D. Are fluorescence quantum yields so tricky to measure? A demonstration using familiar stationery products. *J. Chem. Ed.* **1999**, *76*, 1260.

[100] Würth, C.; Grabolle, M.; Pauli, J.; Spieles, M.; Resch-Genger, U. Relative and absolute determination of fluorescence quantum yields of transparent samples. *Nature Protocols* **2013**, *8*, 1535.

[101] Brouwer, A.M. Standards for photoluminescence quantum yield measurements in solution (IUPAC Technical Report). *Pure Appl. Chem.* **2011**, *83*, 2213-2228.

[102] Kubin, R. F.; Fletcher, A. N. Fluorescence quantum yields of some rhodamine dyes. *J Lumin* **1982**, *27*, 455-462.

[103] Ogunsipe, A.; Nyokong, T. Effects of central metal on the photophysical and photochemical properties of non-transition metal sulfophthalocyanine. *J. Porphyrins Phthalocyanines* **2005**, *9*, 121-129.

[104] Birch, D.J.; Imhof, R.E. Time-domain fluorescence spectroscopy using time-correlated single-photon counting. In *Topics in Fluorescence Spectroscopy*, Lakowicz, R.E. (Ed); Springer: Berlin, 2002, pp 1-95.

[105] O'Connor, D. *Time-correlated single photon counting;* Academic Press: Cambridge, Massachusetts, 2012.

[106] Chen, R.; Wu, R.; Zhang, G.; Gao, Y.; Xiao, L.; Jia, S. Electron transfer-based single molecule fluorescence as a probe for nano-environment dynamics. *Sensors* **2014**, *14*, 2449-2467.

[107] Becker, W.; Bergmann, A.; Hink, M.; König, K.; Benndorf, K.; Biskup, C. Fluorescence lifetime imaging by time-correlated single photon counting. *Microsc. Res. Tech.* **2004**, *63*, 58-66.

[108] Usui, Y. Determination of quantum yield of singlet oxygen formation by photosensitization. *Chem. Lett.* **1973**, *2*, 743-744.

[109] Kuznetsova, N.; Gretsova, N.; Kalmykova, E.; Makarova, E.; Dashkevich, S.; Negrimovskii, V.; Kaliya, O.; Luk'Yanets, E. Relationship between the photochemical properties and structure of pophyrins and related compounds. *Russ. J. General Chem.* **2000**, *70*, 133-140.

[110] Waris, G.; Ahsan, H. Reactive oxygen species: role in the development of cancer and various chronic conditions. *J. Carcinog*. **2006**, *5*, 14-31.

[111] Gandra, N.; Frank, A. T.; Le Gendre, O.; Sawwan, N.; Aebisher, D.; Liebman, J. F.; Houk, K.; Greer, A.; Gao, R. Possible singlet oxygen generation from the photolysis of indigo dyes in methanol, DMSO, water, and ionic liquid, 1-butyl-3-methylimidazolium tetrafluoroborate. *Tetrahedron* **2006**, *62*, 10771-10776.

[112] Redmond, R.; Gamlin, J. A compilation of singlet oxygen yields from biologically relevant molecules. *Photochem. Photobiol.* **1999**, *70*, 391-475.

[113] Neckers, D. Rose Bengal. *J. Photochem. Photobiol. A.* **1989**, *47*, 1-29.

[114] Yang, Y.; Zhang, L.; Gao, C.; Xu, L.; Bai, S.; Liu, X. Pyrene-based BODIPY: synthesis, photophysics and lasing properties under UV-pumping radiation. RSC Advances 2014, 4, 38119-38123.

[115] Hoogendoorn, S.; Blom, A. E.; Willems, L. I.; van der Marel, Gijsbert A; Overkleeft, H. S. Synthesis of pH-activatable red fluorescent BODIPY dyes with distinct functionalities. *Org. Lett.* **2011**, *13*, 5656-5659.

[116] Harris, J. BODIPY Dyes for Singlet Oxygen and Optical Limiting Applications, MSc thesis, Rhodes University, Grahamstown, South Africa, 2018.

[117] Wang, Z.; Zhao, J. Bodipy–Anthracene Dyads as Triplet Photosensitizers: Effect of Chromophore Orientation on Triplet-State Formation Efficiency and Application in Triplet–Triplet Annihilation Upconversion. *Org. Lett.* **2017**, *19*, 4492-4495.

[118] Ueno, T.; Urano, Y.; Kojima, H.; Nagano, T. Mechanism-based molecular design of highly selective fluorescence probes for nitrative stress. *J. Am. Chem. Soc.* **2006**, *128*, 10640-10641.

[119] Quan, L.; Lin, W.; Sun, T.; Xie, Z.; Huang, Y.; Jing, X. Green Photocatalysis with Oxygen Sensitive BODIPYs under Visible Light. *Catal. Lett.* **2014**, *144*, 308-313.

[120] Qin, W.; Baruah, M.; De Borggraeve, W. M.; Boens, N. Photophysical properties of an on/off fluorescent pH indicator excitable with visible light based on a borondipyrromethene-linked phenol. *J. Photochem. Photobiol. A.* **2006**, *183*, 190-197.

[121] Kubheka, G. Synthesis and physicochemical evaluation of a seriesof boron dipyrromethene dye derivatives for potential utility in antimicrobial photodynamic therapy and nonlinear optics, MSc thesis, Rhodes University, Grahamstown, South Africa, 2016.

[122] May, A.K. Photosensitizer, pH sensing and optical limiting properties of BODIPY dyes, MSc thesis, Rhodes University, Grahamstown, South Africa, 2016.

[123] (a) Lebechi, A.K.; Nyokong, T.; Mack, J. BODIPY Dye Embedded Electrospun Polystyrene Nanofibers for the Photocatalytic Degradation of Orange G in Industrial Wastewaters. *Macroheterocycles* **2017**, *10*, 460-466. (b) Lebechi, A. K.; Gai, L.; Shen, Z.; Nyokong, T.; Mack, J. Electrospun 3,5-dithienylvinyleneBODIPY embedded polystyrene nanofibers for the photocatalytic degradation of azo dyes in industrial wastewaters. *J. Porphyrins Phthalocyanines* **2018**, 1-8.

[124] Akpan, U.G.; Hameed, B.H. Parameters Affecting the Photocatalytic Degradation of Dyes using TiO_2-based Photocatalysts: A Review. *J. Hazard. Mater.* **2009**, *170*, 520-529.

[125] Obana, N.; Swaminathan, M. Combination effect of ZnO and activated carbon for solar assisted photocatalytic degradation of Direct Blue 53. *Solar Energy Mater. Solar Cells* **2007**, *91*, 727-734.

[126] Qu, Y.; Yang, H.; Yang, N.; Fan, Y.; Zhu, H.; Zou, G. The effect of reaction temperature on the particle size, structure and magnetic properties of coprecipitated $CoFe_2O_4$ nanoparticles. *Mater. Lett.* **2006**, *60*, 3548-3552.

[127] Ehrenberg, B.; Malik, Z.; Nitzan, Y. Fluorescence spectral changes of hematoporphyrin derivative upon binding to lipid vesicles, *Staphylococcus aureus*, and *Escherichia coli* cells. *Photochem. Photobiol.* **1985**, *41*, 429-435.

[128] Nikaido, H. Outer membrane barrier as a mechanism of antimicrobial resistance. *Antimicrob. Agents Chemother.* **1989**, *33*, 1831-1836.

[129] Khoza, P.; Nyokong, T. Photocatalyticbehavior of phthalocyanine-silver nanoparticle conjugates supported on polystyrene fibers. *J. Mol. Catal. A* **2014**, *395*, 34-41.

[130] Bachmann, B.J. Linkage map of Escherichia coli K-12, edition 8. *Microbiol. Rev.* **1990**, *54*,130-197.

[131] Frenette, M.; Hatamimoslehabadi, M.; Bellinger-Buckley, S.; Laoui, S.; La, J.; Bag, S.; Mallidi, S.; Hasan, T.; Bouma, B.; Yelleswarapu, C. Shining light on the dark side of imaging: excited state absorption enhancement of a bis-styryl BODIPY photoacoustic contrast agent. *J. Am. Chem. Soc.* **2014**, *136*, 15853-15856.

[132] Ngoy, B.P.; May, A.K.; Mack, J.; Nyokong, T. Effect of bromination on the optical limiting properties at 532 nm of BODIPY dyes with p-benzyloxystyryl groups at the 3,5-positions. *J. Mol. Struct.* **2019**, *1175*, 745-753.

[133] Kubheka, G.; Mack, J.; Kobayashi, N.; Kimura, M.; Nyokong, T. Optical limiting properties of 2,6-dibromo-3,5-distyrylBODIPY dyes at 532 nm. *J. Porphyrins Phthalocyanines* **2017**, *21*, 523-531.

[134] Kubheka, G.; Sanusi, K.; Mack, J.; Nyokong, T. Optical limiting properties of 3,5-dipyrenylvinyleneBODIPY dyes at 532 nm. *Spectrochim. Acta A* **2018**, *191*, 357-364.

[135] Harris, J.; May, AK.; Ngoy, BP.; Mack, J.; Nyokong, T. Photophysical properties and electronic structures of 1,3,5-tristyrlBODIPY dyes. Accepted for publication in the *J. Porphyrins and Phthalocyanines* in 2019. {doi: 10.1142/S1088424619500019}

[136] Gaussian 09, Revision D.01, Frisch, M.J.; Trucks, G.W.; Schlegel, H.B.; Scuseria, G.E.; Robb, M.A.; Cheeseman, J.R.; Scalmani, G.; Barone, V.; Petersson, G.A.; Nakatsuji, H.; Li, X.; Caricato, M.; Marenich, A.; Bloino, J.; Janesko, B.G.; Gomperts, R.; Mennucci, B.; Hratchian, H.P.; Ortiz, J.V.; Izmaylov, A.F.; Sonnenberg, J.L.; Williams-Young, D.; Ding, F.; Lipparini, F.; Egidi, F.; Goings, J.; Peng, B.; Petrone, A.; Henderson, T.; Ranasinghe, D.; Zakrzewski, V.G.; Gao, J.; Rega, N.; Zheng, G.; Liang, W.; Hada, M.; Ehara, M.; Toyota, K.; Fukuda, R.; Hasegawa, J.; Ishida, M.; Nakajima, T.; Honda, Y.; Kitao, O.; Nakai, H.; Vreven, T.; Throssell, K.; Montgomery, J.A. Jr.; Peralta, J.E.; Ogliaro, F.; Bearpark, M.; Heyd, J.J.; Brothers, E.; Kudin, K.N.; Staroverov, V.N.; Keith, T.; Kobayashi, R.; Normand, J.; Raghavachari, K.; Rendell, A.; Burant, J.C.; Iyengar, S.S.; Tomasi, J.; Cossi, M.; Millam, J.M.; Klene, M.; Adamo, C.; Cammi, R.; Ochterski, J.W.; Martin, R.L.; Morokuma, K.; Farkas, O.; Foresman, J.B.; Fox, D.J. Gaussian, Inc., Wallingford CT, 2016.

[137] Yanai, T.; Tew, D.P.; Handy, N.C. A new hybrid exchange-correlation functional using the Coulomb-attenuating method (CAM-B3LYP). *Chem. Phys. Lett.* **2004**, *393*, 51-57.

[138] Chemcraft - graphical software for visualization of quantum chemistry computations. https://www.chemcraftprog.com